



UNIVERSITÀ DEGLI STUDI DI TRIESTE

**XXX CICLO DEL DOTTORATO DI RICERCA IN
*SCIENZE DELLA TERRA E MECCANICA DEI FLUIDI***

**Toward a coastal processing resolving ocean model -
nesting LES-COAST and MITgcm**

Settore scientifico-disciplinare: **ICAR/01**

**DOTTORANDO:
Massimiliano Palma**

**COORDINATORE:
Prof. Pierpaolo Omari**

**SUPERVISORE DI TESI:
Prof. Vincenzo Armenio**

**CO-SUPERVISORE DI TESI:
Dr. Gianmaria Sannino**

Anno Accademico 2016-2017

Abstract

Coastal and shelf seas represent a small fraction of the area of the global ocean but have a disproportionately large impact on many aspects of the marine environment and human activities (Holt et al., 2017).

Improving the representation of coastal and shelf seas in global models is one of the grand challenges in ocean modelling and Earth system science (Holt et al., 2017). Global ocean models often have poor representation of coastal and shelf seas due to both their coarse resolution and their lack of coastal ocean process representation (Renner et al., 2009; Holt et al., 2010; Holt et al., 2017). Accurate parameterization of vertical mixing processes has been a long-standing issue in ocean circulation modelling. A variety of schemes have been developed to face this challenge. Wind-driven turbulent boundary layer mixing, convection forced from the surface or at an overturning front, internal wave breaking and Kelvin-Helmholtz instabilities at the pycnocline are several of the typically unresolved mechanisms which contribute significantly to the vertical redistribution of both momentum and scalars (Durski et al., 2004).

As the demand for more accurate higher-resolution real ocean simulations increases, it is important to continue to assess the performance of currently available parameterizations to determine what can be done to improve their quality (Durski et al., 2004).

Ocean general circulation models (OGCMs) have improved to the point that they can capture many of the features of mesoscale coastal processes but rarely with the accuracy necessary for vertical mixing estimates to be directly compared with small-scale turbulent measurements in the field (Durski et al., 2004).

The MIT General Circulation Model (MITgcm) (Marshall et al. 1997a) has been applied to simulations of geophysical flows over a broad range of scales, from large-scale global circulation (Adcroft et al. 2004, Marshall et al. 1997b) to small-scale processes such as convection and internal waves. At global scales, due to the large domain and coarse grid, the hydrostatic solver is employed. Also, owing to lack of field observations, the model parameters such as sub-grid scale (SGS) closures are typically set without performing any sensitivity analysis and calibration based on existing field data (Dorostkar et al., 2010).

To conclude, there is a need for carefully evaluating the accuracy of the OGCMs (and their SGS models) below the mesoscale regime (Marques et al., 2014). As such, a clear avenue for gaining more insight into the accuracy of OGCMs solutions for mixing and stirring problems is using Large Eddy Simulation (LES) as reference.

LES solutions are feasible and refer to numerical solutions of the non-hydrostatic equations in which the large eddies, carrying most of the turbulent kinetic energy stresses, are resolved through computation, while the effect of the smaller eddies on the flow is represented by SGS models that must reproduce the energy dissipation associated to the small scales of motion (Marques et al., 2014).

Definitely, investigating the large-scale impacts on smaller-scale processes in the coastal ocean can often be successfully treated by (one-way or two-way) nested regional studies.

In the present thesis, first of all, a sensitivity analysis and calibration are carried out in the application of the MITgcm (a non-hydrostatic, z-coordinate, finite volume model that solves the incompressible Navier-Stokes equations with the Boussinesq approximation on an Arakawa-C grid) to simulate the basin-scale response of a domain to wind forcing. Understanding model sensitivity is a vital initial step. The performance of different vertical and horizontal mixing parameterizations is analysed to assess in what aspects they differ (the vertical mixing scheme developed by Gaspar et al., 1990 (GGL90) and the Leith viscosities for the horizontal mixing, respectively).

In this way a series of numerical simulations have been conducted and our goal has been to compare the results derived from two modelling approaches: an OGCM (MITgcm) and a LES, which has been used as our ground truth.

It has been discovered that the choice of a right configuration for GGL90 vertical mixing scheme plays a major role in the temporal evolution of horizontal velocity field. However, no total convergence towards the ground truth reference (LES) has been attained and the best results have been achieved using Leith viscosity for the horizontal mixing parameterization; While MITgcm simulations differ from LES in the amount of vertical mixing, the simulated feature of horizontal velocity field appear to be quite similar.

Later, considering that nesting remains an important approach for investigating of regional systems and providing fine-scale information, an unprecedented approach is proposed. A nesting (before “off-line” and successively “run-time”) between a general circulation model and a LES model has been designed and developed.

The nested model, proposed in this work, consists of two models: a MITgcm and a LES-Coast model. The two models involved are coupled via an external driver that establishes a connection, passing information from MITgcm to LES-Coast and that performs also all the necessary interpolations.

This driver represents the main core of the developed procedure.

In this work the MITgcm (Adcroft et al., 2014) is used in its non-hydrostatic, implicit free-surface, partial step topography formulation. LES-COAST model (Roman et al., 2010, University of Trieste) makes use of large-eddy simulation approach to solve three-dimensional Navier-Stokes equations, the model is suited for simulation of fluid flow in harbour and coastal areas. Complex coastline and bathymetry are reproduced by a combination of curvilinear structured grid and immersed boundaries (Roman et al., 2009b).

In order to allow the communication between these three codes (2 models plus driver), both models have been deeply modified; i.e. the insertion of new variables and new “include” files it was necessary, as well as a new initialization of the MPI environment for each model.

It has been shown how the “nested-LES” feels the effects of the MITgcm, as in the experiment with a neutral stratification as for the stable stratified case. Comparing the results of simulations MITgcm stand-alone and LES-Coast after nesting, it is evident how the resolution of the velocity field has been clearly improved. Moreover, the nested model has shown a remarkable sensitivity to the update frequency of the lateral boundary conditions.

Contents

<i>Introduction</i>	<i>1</i>
Chapter 1 – Numerical Ocean Models	7
<i>1.1 – Ocean models</i>	<i>7</i>
<i>1.2 – Options for discretization</i>	<i>9</i>
1.2.1 – Horizontal and vertical coordinates	10
Chapter 2 – Ocean General Circulation Model	12
<i>2.1 – MIT General Circulation Model</i>	<i>12</i>
2.1.1 – Continuous equations in “r” coordinates	12
2.1.2 – Non-hydrostatic capability	14
2.1.3 – Time-stepping	15
2.1.4 – Spatial discretization	16
<i>2.2 – MITgcm in coastal applications</i>	<i>17</i>
Chapter 3 – Large Eddy Simulation (LES)	20
<i>3.1 – LES in coastal oceanography</i>	<i>20</i>
<i>3.2 – LES-COAST Model</i>	<i>23</i>
3.2.1– The governing equations	24
3.2.2 – Numerical method	27
3.2.3 – Sub-grid scale (SGS) model	29
3.2.4 – Boundary conditions over solid boundaries	31

Chapter 4 – Wind Driven Circulation	33
<i>4.1 – Models Configuration</i>	33
<i>4.2 – LES-Coast simulation</i>	34
4.2.1– Instantaneous field	34
4.2.2– Turbulent Kinetic Energy	38
4.2.3– Eddy Viscosities	39
<i>4.3 – MITgcm simulations</i>	42
4.3.1– Constant horizontal eddy viscosity-sensitivity analysis	44
4.3.2– Leith viscosity- sensitivity analysis	61
Chapter 5 – Nesting Procedure	71
<i>5.1 – One-way Nesting</i>	74
<i>5.2 – Off-line Nesting</i>	74
<i>5.3 – Run-time Nesting</i>	80
Chapter 6 – Stratified Case	86
<i>6.1 – LES-Coast simulation</i>	87
<i>6.2 – MITgcm simulation</i>	90
<i>6.3 – Run-time Nesting</i>	93
Conclusions	96
Bibliography	103

Introduction

Approximately 70% of the earth's surface is covered by the ocean (Kantha et al., 2000), and in the ocean it is possible to find around 97% of all the water on the earth (Brown et al., 1989).

Seven prognostic equations to forecast the weather were presented by Wilhelm Bjerknes in his paper in 1904 (Bjerknes et al., 1904). Bjerknes thought that, given suitable initial and boundary conditions, the weather could be predicted far into the future by these equations. These seven prognostic equations are found useful for forecasting the weather systems and the currents in the ocean too. They now form the basis for both atmospheric and oceanic numerical models. In the early 1960s, Kirk Bryan and Michael Cox developed the first numerical ocean model (Bryan, 1969).

Since the early days of oceanography, the attention has been moved from the mean circulation to the variability of the mean circulation, regional studies and process studies. Nowadays numerical models provide a complete description of the entire ocean, but there are still large unknown mysteries as turbulent mixing in the ocean and the connection between large scales and smaller scales. However, the discretization of the equations introduces errors to the solution of numerical models, that are only an image of the real ocean. The ocean is highly turbulent and it is characterized by three-dimensionality, irregularity, vorticity, unsteadiness (Kantha et al. 2000) and the processes that are not directly calculated must be parameterized using sub-grid models.

In spite of the challenges, numerical ocean models, giving us the opportunity to study processes that cover a large spectrum of time scales and length scales, are an excellent tool for studying the interaction between different scales and different physical phenomena as tides, mixing and the large-scale circulation (Jayne et al. 2004).

Ocean general circulation models (OGCMs) are the primary tools for predicting ocean currents and changes in the ocean's stratification (Marques et al., 2014). Many OGCMs integrate the hydrostatic primitive equations (PE) set using a variety of horizontal and vertical coordinates, mixing parameterizations and advection schemes (Griffies et al., 2000, 2004, Marques et al., 2014). These models can be configured at the global and regional scale or can have a nested structure to represent multi-scale interactions (Debreu et al., 2012). Modern OGCMs contain realistic forcing, domain geometry and assimilate ocean data available from a wide range of instruments, including satellite altimeter, sea surface temperature, current meters, drifters and other in situ data for temperature and salinity (Marques et al., 2014). Ocean observing and assimilation techniques have matured to a level where one can claim that the dynamics, phase and strength of the ocean's mesoscale features are adequately represented in OGCMs (Marques et al., 2014). Nevertheless, OGCMs may encounter significant obstacles for reproducing accurate results for scales smaller and faster than the mesoscale (scales smaller than $O(10)$ km and shorter than a few days) due primarily to three reasons (Marques et al., 2014).

First, data at such scales may not be available from observing systems or contain technical challenges within the context of present assimilation methods (Marques et al., 2014). For instance, sea-surface height data is usually converted to velocity under the assumption of geostrophy, while submesoscale flows are distinctly ageostrophic (Mahadevan and Tandon, 2006; Thomas et al., 2008; Marques et al., 2014).

Second, OGCMs may not resolve submesoscale features fully and must rely on subgrid-scale (SGS) parameterizations (Fox-Kemper et al., 2008; Fox-Kemper and Ferrari, 2008). Recent numerical studies showed that the SGS parameterization can have important consequences in the temporal and spatial evolution of submesoscale instabilities even when the grid spacing resolves the submesoscale (Ramachandran et al., 2013; Marques et al., 2014).

OGCMs were originally designed to model large scale processes, where the flow is anisotropic with lateral processes being far more energetic than vertical processes and the unresolved processes are represented through an eddy viscosity or diffusivity (Marques et al., 2014).

Third, even if the OGCMs contain the spatial resolution to extend into the submesoscales and below, the PE start losing validity, being subject to the hydrostatic approximation (Kantha and Clayson, 2000; Marques et al., 2014). The hydrostatic approximation affects both dissipative and dispersive properties of fluid motion (Marques et al., 2014).

To conclude, there is a need for carefully evaluating the accuracy of the OGCMs (and their SGS models) below the mesoscale regime (Marques et al., 2014). As such, a clear avenue for gaining more insight into the accuracy of OGCMs solutions for mixing and stirring problems is using LES (large eddy simulation) as reference. The scales of interest include submesoscales, as well as fully 3D stratified mixing, that is of interest in coastal phenomena (Warner et al., 2005a;)

Coastal and shelf seas represent a small fraction of the area of the global ocean (9.7 % of the global ocean is < 500 m deep and 7.6 % < 200 m) but have a disproportionately large impact on many aspects of the marine environment and human activities (Holt et al., 2017). Improving the representation of coastal and shelf seas in global models is one of the grand challenges in ocean modelling and Earth system science (Holt et al., 2017). Global ocean models often have poor representation of coastal and shelf seas due to both their coarse resolution and their lack of coastal ocean process representation. (Renner et al., 2009; Holt et al., 2010; Holt et al., 2017). The lack of physical understanding of turbulence is one of the main challenges of numerical ocean modelling today. The study of coastal and shelf seas in a global context involves both upscaling and downscaling considerations, alongside the internal

dynamics. Both dynamics and bio-geochemistry provide motivations to studying the influence of coastal ocean processes on a global scale (Holt et al., 2017).

Investigating the large-scale impacts on smaller-scale processes in the coastal ocean can often be successfully treated by (one-way or two-way) nested regional studies, focusing on an area of interest ranging from local (e.g. Zhang et al., 2009) to regional (e.g. Wakelin et al., 2009) to basin (e.g. Holt et al., 2014; Curchitser et al., 2005) scale (Holt et al., 2017).

While regional or local models often provide the optimal solution for many coastal ocean questions there is a significant overhead in their deployment (Holt et al. 2017). A global model with improved representation of the coastal ocean opens up the opportunity to provide rapid and cost-effective information in a particular region for either scientific or operational use, without needing to configure a new domain (Holt et al. 2017). The distinct physical characteristics of the coastal ocean, in comparison to other oceanic regions, are largely determined by their shallow depth and proximity to land; this has several implications for the dynamics (Holt et al. 2017).

Nesting is the most common approach to multiscale modelling. In its simplest form, boundary conditions for a fine-resolution model are taken from a previous run of a larger area ocean model. It has the significant advantage that the global model does not have to be rerun for each regional simulation (Holt et al., 2017). Considering that nesting remains an important approach for investigating of regional systems and providing fine-scale information, in this thesis an unprecedented approach is proposed. A nesting between a general circulation model and a Large Eddy Simulation (LES) model has been designed and developed.

LES solutions are feasible and refer to numerical solutions of the non-hydrostatic equations in which the large eddies, carrying most of the turbulent kinetic energy stresses, are resolved through computation, while the effect of the smaller eddies on the flow is represented by SGS models that must reproduce the energy dissipation associated to the small

scales of motion (Marques et al., 2014). The LES approach lies in between the extremes of direct numerical simulation (DNS), where all turbulence is resolved, and Reynolds-averaged Navier–Stokes (RANS), in which only the mean flow is computed while the entire effect of turbulence is represented by turbulence models (Marques et al., 2014). Since LES greatly reduces the SGS parameterization problem, many studies on ocean turbulence have relied on this approach to establish a ground truth for particular problems (Chang et al., 2005; Xu et al., 2006; Marques et al., 2014).

The nested model, proposed in this work, consists of two models: a MIT general circulation model (MITgcm) and a LES-Coast model. The two models involved are coupled via an external driver that establishes a connection, passing information from one model to another and that performs also all the necessary interpolations. This driver represents the main core of the developed procedure.

The MITgcm is a numerical model designed for study of the atmosphere, ocean, and climate. Its non-hydrostatic formulation enables it to simulate fluid phenomena over a wide range of scales. In this work the MITgcm (Adcroft et al., 2014) is used in its non-hydrostatic, implicit free-surface, partial step topography formulation.

LES-COAST model (Roman et al., 2010, University of Trieste) makes use of large-eddy simulation approach to solve three-dimensional Navier-Stokes equations, the model is suited for simulation of fluid flow in harbour and coastal areas. Complex coastline and bathymetry are reproduced by a combination of curvilinear structured grid and immersed boundaries (Roman et al., 2009b). The model was successfully used to reproduce wind-driven circulations in the industrial harbour of Trieste (Italy) (Petronio et al., 2013).

The thesis is structured as follows: chapter 1 provides an overview of numerical ocean models; The MIT General Circulation Model is illustrated in the chapter 2. Chapter 3 describes the mathematical model and the main features of LES-COAST model; In chapter 4 simulations of the wind driven circulation in a simplified domain and the results of a sensitivity analysis of MITgcm are presented. The nesting procedure and the obtained results are illustrated in chapter 5. In Chapter 6 are presented the results of the stratified case. Finally, concluding remarks and an idea for a future work are given.

Chapter 1 – Numerical Ocean Models

In the ocean measurements are sparse both in time and space, so numerical ocean models are a considerable tool for studying the ocean, giving us the possibility to study either large or local regions with full descriptions of all the components, i.e. salinity, temperature, velocity. The versatility of the numerical models allows us to study how different parameters affect the circulation. Moreover, models can be used to gain more knowledge of physical processes in the ocean, to predict future ocean scenarios and to explore the relationships and interactions between the different scales.

1.1 Ocean models

Numerical ocean models are principally based on the following same set of equations:

The Navier stokes equations,

$$\frac{\partial \vec{u}}{\partial t} + \vec{u} \cdot \nabla \vec{u} + 2\Omega \times \vec{u} = -\frac{1}{\rho} \nabla p - g\vec{k} + \nu \nabla^2 \vec{u} \quad (1.1)$$

the equation of continuity,

$$\nabla \cdot \vec{u} = 0 \quad (1.2)$$

conservation of scalar properties,

$$\frac{\partial \phi}{\partial t} + \vec{u} \cdot \nabla \phi = \kappa_s \nabla^2 \phi + \Phi \quad (1.3)$$

and an equation of state,

$$\rho = \rho(T, S, p) \quad (1.4)$$

Here \vec{u} represents the velocity components, t the time, Ω the earth's rotation, ρ the density, p the pressure, ν the kinematic viscosity, ϕ the scalar properties such as temperature and salinity, κ_s the diffusivity, Φ a source or sink term of the scalars, T the temperature, and S the salinity.

Turbulence, due to non-linear instabilities, takes place in the flow for high Reynolds numbers (Burchard, 2002). Turbulence takes place on a wide range of scales, it is generated by shear, waves, and also due to viscous effects near boundaries (Burchard, 2002) and it is characterized by non-linearity, randomness, and irregularity (Kantha et al., 2000). To describe turbulence, statistical methods can be used but at present it is impossible to predict the exact development of the instantaneous turbulent flow (Burchard, 2002).

Most of the kinetic energy resides in the large-scale motion and energy is carried by turbulence from the large scale to the viscous scales. Non-linear instabilities generate eddies; the largest eddies extract energy from the mean flow. This energy is gradually transferred to smaller and smaller eddies (Kundu, 2004). Finally the smallest scales are transferred to heat due to viscous friction (Burchard, 2002). This transect of energy from large to smaller scales is called the energy cascade. An energy spectrum consisting of the energy containing scales, the viscous scales and the inertial subrange, exist for high Reynolds numbers. In the inertial subrange, the eddies are independent on both the large scale forcing and the viscosity. In 1941, Kolmogorov (Kolmogorov, 1991) presented his famous two-thirds law,

$$E(K_w) \propto \epsilon^{2/3} K_w^{-5/3} \quad (1.5)$$

Here $E(K_w)$ represents the energy spectrum, ϵ the dissipation rate, and K_w the wave number. This law describes the energy cascade within the inertial subrange; It assumes isotropic turbulence, stationarity, homogeneity, and an infinite Reynolds number. For small scales, the turbulence is approximately isotropic (Kundu, 2004) and the eddies at this scale are not affected by the mean direction of the flow. The dissipation rate, ϵ , depends on the large scales (Burchard, 2002).

It is possible to define, based on how they deal with different scales and turbulent processes, different classes of numerical models.

1)**Direct Numerical Simulations, DNS**, that solve the governing equations of fluid motions and scalar transport directly without any additional model for turbulence closure. All scales from the Kolmogorov scale, η_k (Kundu, 2004)

$$\eta_k = \left(\frac{\nu^3}{\epsilon} \right)^{1/4} \quad (1.6)$$

are resolved by the use of efficient spectral techniques (Kantha et al., 2000). Here ν represents the kinematic viscosity. In order to obtain correct results, the domain in DNS-simulations must be at least large enough to resolve the largest turbulent eddy in the flow (Baumert et al., 2005) and the grid size should be smaller or equal to the Kolmogorov scale.

However, such simulations are highly computationally costly and at present it is only possible to achieve high Reynolds numbers on laboratory scales (Kantha et al. 2000).

2)**Large Eddy Simulations, LES**, that resolve the most energy containing eddies, while smaller scales are represented by the use of a sub-scale turbulence closure model (Burchard, 2002). The model-resolution should be chosen so that the subgrid scales are within the Kolmogorov inertial subrange (Kantha et al. 2000). In LES models the viscosities and diffusivities in the Navier-Stokes equations are replaced by eddy viscosities and diffusivities estimated from the sub-grid turbulence model.

3)**Reynolds Averaged Navier-Stokes Simulations, RANS-models**, that split the velocities, u , v , w , and the pressure, p , into a mean component and its fluctuations, i.e. $u_i = \bar{U}_i + u'_i$. The Navier Stokes equations are averaged both in time and in space and the intention is to capture the average velocities, etc. in each timestep. RANS models do not include any random turbulent motion (Burchard, 2002), and the turbulent motions are all estimated through sub-scale models and represented by eddy viscosities and diffusivities.

1.2 Options for discretization

The mathematical model must be discretized to transform the partial differential equation (PDE) into a numerical model. Euler, in the 18th century, introduced the finite differences method (FDM) and it is the oldest numerical method for solving PDEs (Ferziger et al., 2002). In finite differences, the derivatives, approximated by the use of Taylor series or polynomial fits (Ferziger et al., 2002), are evaluated based on neighbouring points and they are a local approximation (Kantha et al. 2000).

The integral form of the governing equations is used in finite volume methods (FVM) (Ferziger et al., 2002). The domain is divided into control volumes or a finite number of subdomains and the equations are solved for each control volume (Ferziger et al., 2002). Finite volume methods are automatically conservative because the flux that flows into a control volume equals the flux out of the subdomain.

The finite element method (FEM) was developed in the 1960s (Kantha et al. 2000). This method is especially appropriate working with complex geometries and when the flow is associated with large spatial variations (Kantha et al. 2000).

1.2.1 HORIZONTAL AND VERTICAL COORDINATES

There exist five different ways to arrange the dependent variables on a grid and these arrangements are called the Arakawa grids, named from A to E (Fig.1.1) (Kantha et al. 2000). Except for type A, where all the variables are located in the same point, all the grid types are staggered. In ocean models the two most common grids are the B- and the C-grid (Haidvogel et al., 1998; Kantha et al. 2000).

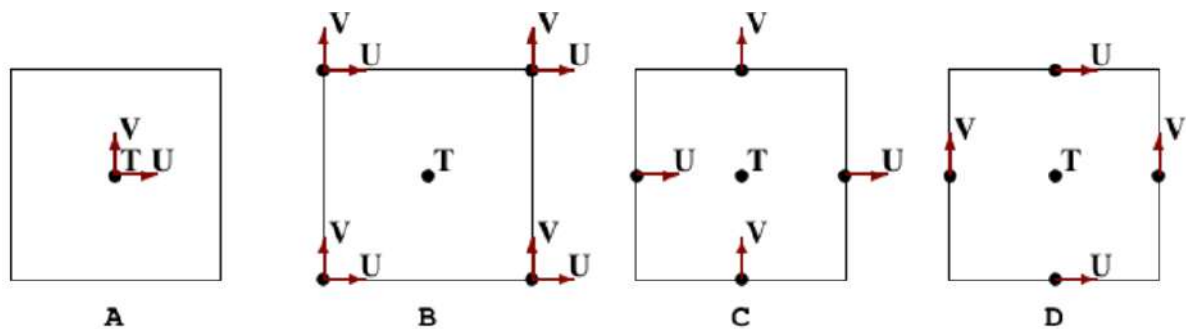


Figure 1.1: Different grids by Arakawa (V. Balaji, Zhi Liang, 2007)

Vertical coordinates are a key consideration especially when modelling the coastal ocean (Holt et al., 2017); the bathymetry necessarily varies substantially at the transition from open ocean to shelf sea and from coastal seas to the land (Holt et al., 2017). Mixing processes require the accurate resolution of the benthic boundary layer, moreover, bottom boundary mixing and freshwater input lead to exceptionally sharp pycnoclines (Holt et al., 2017).

To discretize the equations in the vertical direction there are several options: i.e. geopotential coordinates, terrain-following coordinates and isopycnal coordinates.

Two vertical coordinate systems are shown in Figure 1.2

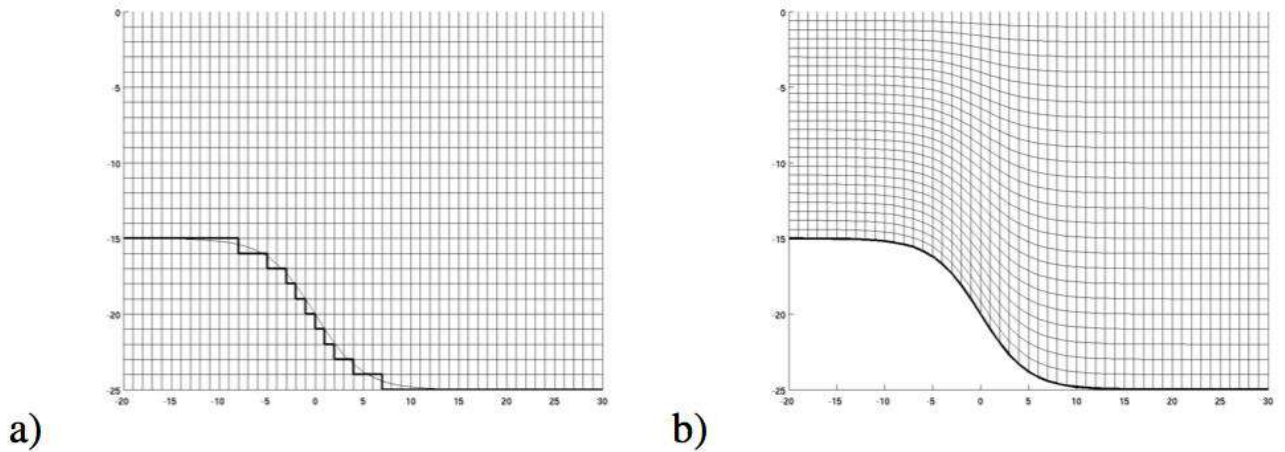


Figure 1.2: a) Geopotential coordinates (z -coordinates) and b) terrain following coordinates (σ -coordinates).

Cartesian grid is used with geopotential coordinates, or z -coordinate models. In this case, it is possible to implement the governing equations directly without the use of transformations. When the bottom matrix is discretized into z -coordinates, truncation errors are introduced (Haidvogel et al., 1998). The result is a stair-case topography on the slopes. It can generate false vertical transports and spurious mixing near the steps (Kantha et al. 2000).

Making use of terrain-following coordinates, the Reynolds averaged equations are transformed using the following standard σ -transformation:

$$x^* = x, \quad y^* = y, \quad \sigma = \frac{z - \eta}{H + \eta}, \quad t^* = t \quad (1.7)$$

Here σ varies between 0 and -1. The σ -coordinates have the value 0 at the surface and -1 at the bottom. In the ocean, the number of vertical layers is the same over the entire domain. It is possible to find large variations in the thickness of a given σ -layer in the deep and the shallow regions in cases with steep slopes.

Using z -coordinate models, the internal pressure gradient is calculated accurately along the exact horizontal lines (Kantha et al. 2000). Terrain-following models have problems with spurious mixing due to errors in the estimate of the internal pressure gradient (Berntsen, 2002). This error generates false velocities (first order error) (Mellor et al., 1998).

In spite of a large scientific focus for the last 40 years, the problem regarding internal pressure in σ -coordinate models is still not solved. Especially for cases with steep topography and stratification, the false velocities due to errors in the internal pressure gradient might be large (Berntsen, 2002).

Chapter 2 – Ocean General Circulation Model

2.1 MIT General Circulation Model

In this paragraph the MIT General Circulation Model is described.

The MIT General Circulation Model (MITgcm) is a numerical model designed for study of the atmosphere, ocean, and climate. It was developed at the Massachusetts Institute of Technology, it solves the equations of motion governing the ocean or Earth's atmosphere using the finite volume method and it was one of the first non-hydrostatic models of the ocean. Its non-hydrostatic formulation enables it to simulate fluid phenomena over a wide range of scales (Adcroft et al., 2014).

MITgcm has a number of novel aspects:

- it can be used to study both atmospheric and oceanic phenomena; one hydrodynamical kernel is used to drive forward both atmospheric and oceanic models
- it has a non-hydrostatic capability and so can be used to study both small-scale and large scale processes
- finite volume techniques are employed yielding an intuitive discretization and support for the treatment of irregular geometries using orthogonal curvilinear grids and shaved cells
- tangent linear and adjoint counterparts are automatically maintained along with the forward model, permitting sensitivity and optimization studies.
- the model is developed to perform efficiently on a wide variety of computational platforms.

2.1.1 CONTINUOUS EQUATIONS IN ‘R’ COORDINATES

To render atmosphere and ocean models from one dynamical core the ‘isomorphisms’ between equation sets, that govern the evolution of the respective fluids, has been exploited.

One system of hydro-dynamical equations is written down and encoded. The model variables have different interpretations depending on whether the atmosphere or ocean is being studied. Thus, for example, the vertical coordinate ‘r’ is interpreted as pressure, p, if the atmosphere is modeled and height, z, if the ocean is modeled (Adcroft et al., 2014).

The state of the fluid at any time is characterized by the distribution of velocity \vec{v} , active tracers θ and S , a ‘geopotential’ Φ and density $\rho = \rho(\theta, S, p)$ which may depend on θ , S , and p . The equations that govern the evolution of these fields, obtained by applying the laws of classical mechanics and thermodynamics to a Boussinesq, Navier-Stokes fluid are, written in terms of a generic vertical coordinate, r , so that the appropriate kinematic boundary conditions can be applied isomorphically:

$$\frac{D\vec{V}h}{Dt} + (2\vec{\Omega} \times \vec{V})h + \nabla h\Phi = \mathcal{F}\vec{V}h \quad \text{horizontal mtm} \quad (2.1)$$

$$\frac{D\dot{r}}{Dt} + \hat{k} \cdot (2\vec{\Omega} \times \vec{V}) + \frac{\partial\Phi}{\partial r} + b = \mathcal{F}\dot{r} \quad \text{vertical mtm} \quad (2.2)$$

$$\nabla h \cdot \vec{V}h + \frac{\partial\dot{r}}{\partial r} = 0 \quad \text{continuity} \quad (2.3)$$

$$b = b(\theta, S, r) \quad \text{equation of state} \quad (2.4)$$

$$\frac{D\theta}{Dt} = Q\theta \quad \text{potential temperature} \quad (2.5)$$

$$\frac{DS}{Dt} = QS \quad \text{humidity/salinity} \quad (2.6)$$

$Q\theta$ are forcing and dissipation of θ

QS are forcing and dissipation of S

In the ocean:

$$r = z \text{ is the height} \quad (2.7)$$

$$\dot{r} = \frac{Dz}{Dt} = w \text{ is the vertical velocity} \quad (2.8)$$

$$\Phi = p/\rho_c \text{ is the pressure} \quad (2.9)$$

$$b(\theta, S, r) = \frac{g}{\rho_c}(\rho(\theta, S, r) - \rho_c) \text{ is the buoyancy} \quad (2.10)$$

where ρ_c is a fixed reference density of water and g is the acceleration due to gravity.

In the above

At the bottom of the ocean: $R_{fixed}(x, y) = -H(x, y)$.

The surface of the ocean is given by: $R_{moving} = \eta$

The position of the resting free surface of the ocean is given by $R_o = Z_o = 0$

Boundary conditions are:

$$w = 0 \text{ at } r = R_{fixed} \text{ (ocean bottom)} \quad (2.11)$$

$$w = \frac{D\eta}{Dt} \text{ at } r = R_{moving} = \eta \text{ (ocean surface)} \quad (2.12)$$

where η is the elevation of the free surface.

2.1.2 NON-HYDROSTATIC CAPABILITY

The pressure, P , in the ocean can be split into three different components:

$$P(x, z, t) = P_\eta(x, t) + P_{int}(x, z, t) + P_{nh}(x, z, t) \quad (2.13)$$

where $P_\eta = g\rho_o\eta(x, t)$ represents the pressure due to the surface elevation,

$P_{int} = \int_z^0 \rho(x, z', t) dz'$ the internal pressure and P_{nh} the non-hydrostatic pressure generated due to internal movements in the fluid.

The hydrostatic approximation is considered dogmatic to many scientists in large scale studies (Marshall et al., 1997). Through this simplification an exact balance is assumed between the vertical pressure gradient and the gravitational force (Kantha et al., 2000),

$$0 = \frac{1}{\rho_0} \frac{\partial P}{\partial z} - \frac{\rho}{\rho_0} g \quad (2.14)$$

The hydrostatic assumption is valid when the vertical length scale is much shorter than the horizontal length scale ($H/L \ll 1$) and the Froude number ($Fr = U/NH$) is small ($\ll 1$). In (Marshall et al, 1997) it was suggested the non-hydrostatic parameter:

$$n_{nh} = \frac{Y^2}{Ri} \quad (2.15)$$

where $Y = h/L$ and $Ri = \frac{N^2 h^2}{U^2}$ represents the Richardson number. The horizontal and vertical length scales are represented by h and L respectively. The Brunt-Vaisala frequency is given by N^2 . The flow can be considered hydrostatic when:

$$n_{nh} \ll 1 \quad (2.16)$$

For cases when the hydrostatic assumption is no longer valid, the pressure must be found from the full vertical momentum equation.

Due to the computational costs, the non-hydrostatic pressure correction should only be included in cases where the non-hydrostatic pressure effects are important and the resolution is high enough to resolve such processes.

2.1.3 TIME-STEPPING

The equations of motion integrated by the model involve four prognostic equations for flow, u and v , temperature, θ , and salt/moisture, S , and three diagnostic equations for vertical flow, w , density/buoyancy, ρ/b , and pressure/geo-potential, ϕ_{hyd} . In addition, the surface pressure or height may be described by either a prognostic or diagnostic equation and if non-hydrostatics terms are included then a diagnostic equation for non-hydrostatic pressure is also solved. The combination of prognostic and diagnostic equations requires a model algorithm that can march forward prognostic variables while satisfying constraints imposed by diagnostic equations (Adcroft et al., 2014).

The basic formulations are:

1. the semi-implicit pressure method for hydrostatic equations with a rigid-lid, variables co-located in time and with Adams-Bashforth time-stepping,
2. as 1. but with an implicit linear free-surface,
3. as 1. or 2. but with variables staggered in time,
4. as 1. or 2. but with non-hydrostatic terms included,
5. as 2. or 3. but with non-linear free-surface.

In all the above configurations it is possible to substitute the Adams-Bashforth scheme with an alternative time-stepping scheme for terms evaluated explicitly in time.

Adams-Bashforth scheme is a quasi-second order method for all explicit terms in both the momentum and tracer equations. This is still the default mode of operation but it is now possible to use alternate schemes for tracers (Adcroft et al., 2014).

An explicit scheme can be described as:

$$\tau^* = \tau^n + \Delta t G_\tau^{(n+\frac{1}{2})}$$

where τ could be any prognostic variable (u , v , θ or S) and τ^* is an explicit estimate of τ^{n+1} and would be exact if not for implicit-in-time terms. The parenthesis about $n+1/2$ indicates that the term is explicit and extrapolated forward in time and for this we use the quasi-second order Adams-Bashforth method:

$$G_\tau^{(n+\frac{1}{2})} = \left(\frac{3}{2} + \varepsilon_{AB}\right) G_\tau^n - \left(\frac{1}{2} + \varepsilon_{AB}\right) G_\tau^{n-1}$$

This is a linear extrapolation, forward in time, to $t = (n + 1/2 + \varepsilon_{AB})\Delta t$. An extrapolation to the mid-point in time, $t = (n + 1/2)\Delta t$, corresponding to $\varepsilon_{AB} = 0$, would be second order

accurate but is weakly unstable for oscillatory terms. A small but finite value for ϵ_{AB} stabilizes the method (Adcroft et al., 2014).

2.1.4 SPATIAL DISCRETIZATION

Spatial discretization is carried out using the finite volume method. This amounts to a grid-point method (namely second-order centered finite difference) in the fluid interior but allows boundaries to intersect a regular grid allowing a more accurate representation of the position of the boundary (Adcroft et al., 2014). The components of flow are staggered in space in the form of an Arakawa C grid. Fig. 2.1 shows the components of flow (u,v,w) staggered in space such that the zonal component falls on the interface between continuity cells in the zonal direction. Similarly, for the meridional and vertical directions. The continuity cell is synonymous with tracer cells (they are one and the same).

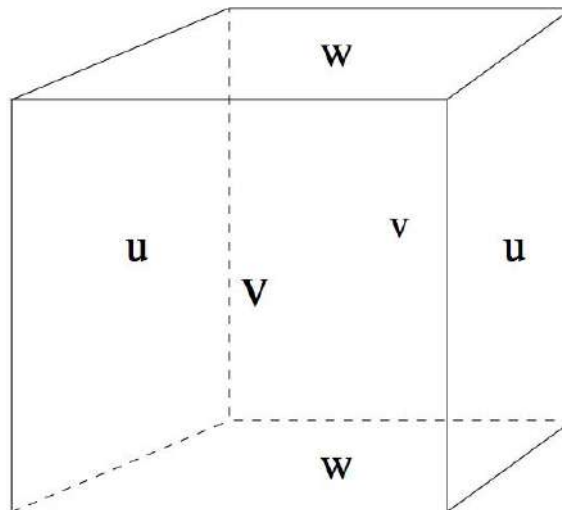


Figure 2.1: Three dimensional staggering of velocity components (Adcroft et al., 2014).

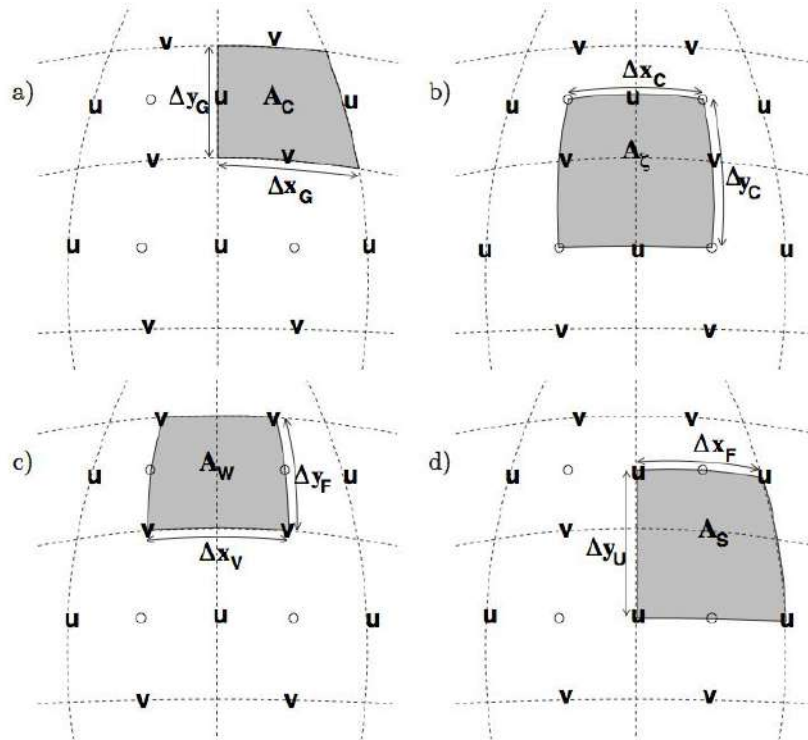


Figure 2.2: Staggering of horizontal grid descriptors (length and areas) (Adcroft et al., 2014).

2.2 MITgcm in coastal applications

Numerical ocean models are now widely used in basic science studies, in studies of the climate, in engineering and in the management of marine resources (Berntsen et al., 2009). Most simulations are presently done with hydrostatic models. The hydrostatic assumption simplifies the numerical computations considerably and has facilitated numerous interesting studies of oceanic flow (Berntsen et al., 2009).

Increasing spatial and temporal resolution appears to be an obvious route for getting more accurate simulations in coastal applications. However, there are penalties for increasing resolution, for example the cost of running a higher resolution model may increase by several orders of magnitude, because if the resolution in 1-D is doubled the resolution in 2-D is 2^2 , plus usually there will be a related reduction in time step which may lead to an order of magnitude increase in the model run time for the same period of real time (Bricheno et al., 2013).

As the horizontal resolution of the ocean models is gradually refined with increasing computer power, the validity of the hydrostatic assumption may, depending both on the problems addressed and the grid sizes used, become questionable. Non-hydrostatic ocean models are therefore used in many recent studies (Berntsen et al., 2009).

In this paragraph, I will focus on some MITgcm coastal applications; A wide range of grid sizes, horizontally and vertically, and subgrid scale closure schemes are applied in these studies.

In “*Horizontal dispersion in shelf seas: High resolution modelling as an aid to sparse sampling (Stashchuk et al.,2014)*” the ability of a hydrodynamic model to reproduce the results of a dye release experiment conducted in a wide shelf sea environment is investigated. The model domain is approximated by a 595 X 491 model grid in the code with a horizontal resolution of 50 m in both zonal and meridional directions. In addition to the central part of the domain, 386 steps are added to the model grid at the northern, southern, western and eastern boundaries, transforming it into a 1383 X 1279 grid. The vertical grid step Δz is equal to 5 m in the upper surface 40 m layer and below it Δz is increased to 10 m.

In “*High-resolution modelling of a large-scale river plume (Vlasenko et al.,2013)*” the evolution of a large-scale river plume is studied. The model parameters were set close to those observed in the area of the Columbia River mouth. The model domain represents an area of 27.5 km in the north–south direction and 23.7 km in the west–east direction. It contains $950 \times 1,100$ grid points with horizontal step $\Delta x = \Delta y = 25$ m (some sensitivity runs were conducted with $\Delta x = \Delta y = 12.5$ m). An additional 50 grid points are added to the north, south and west directions with grid step increasing up to 4,000 m In the vertical direction, the grid step varied from a resolution of 1 m near the surface to 10 m in bottom layers

In “*Three-dimensional simulation of NLIW generation, propagation and breaking in Cayuga Lake (Boegman et al.,2011)*” the 3D non-hydrostatic MITgcm is applied to simulate the dynamics of Nonlinear internal waves (NLIWs) in long narrow Cayuga Lake (NY). This allows for high-resolution simulation (20 m x 20 m x 0.5 m) in a closed domain at high Reynolds number ($Re \sim 105$).

In “*On the importance of non-hydrostatic processes in determining tidally induced mixing in sill regions (Xing et al.,2007)*” the importance of using a non-hydrostatic model to compute tidally induced mixing and flow in the region of a sill is examined using idealized topography representing the sill at the entrance to Loch Etive. This site is chosen since detailed measurements were recently made there. Calculations are performed with and without the inclusion of non-hydrostatic dynamics using a vertical slice model for a range of sill widths corresponding to typical sill regions. By employing fine grids of 10m in the horizontal and 1m in the vertical, it is possible to use minimum values of diffusivity, namely $K_v = K_h = 10^{-7} \text{ m}^2 \text{ s}^{-1}$ and viscosity $A_v = 10^{-3}$, $A_h = 10^{-1} \text{ m}^2 \text{ s}^{-1}$. By this means the small-scale

processes that contribute to the mixing can in part be resolved and regions where intense mixing can occur, identified in terms of critical Richardson number can be determined.

In “*Subaqueous melting of Store Glacier, west Greenland from three-dimensional, high-resolution numerical modeling and ocean observations (Xu et al.,2013)*” three-dimensional, high-resolution simulations of ice melting at the calving face of Store Glacier, a tidewater glacier in West Greenland, is presented. The authors compare the simulated ice melt with an estimate derived from oceanographic data. The simulations show turbulent upwelling and spreading of the freshwater-laden plume along the ice face and the vigorous melting of ice at rates of meters per day. The model domain is a simplified representation of the Store Glacier fjord. It is used 1 m horizontal and vertical grid spacing near the ice front and gradually increase horizontal grid spacing to 5 m in the x direction at the open ocean boundary.

Chapter 3 - Large Eddy Simulation (LES)

3.1 LES in coastal oceanography

Coastal areas are usually shallow and with complex geometry, arising from rapid varying bathymetry, coastline and anthropic structures (Roman et al., 2010; Petronio et al., 2013). Variations of density, temperature and salinity in the water column give rise to buoyancy-driven mixing, which is intensified in the presence of river run-off (Roman et al., 2010; Petronio et al., 2013). The resulting flow field is three dimensional and turbulent.

Turbulence is an unresolved problem of classical physics. Because of the non-linearity of the fluid motion equations there are no analytical solutions. Turbulence is composed of eddies in a broad range of size. These vortices are formed and break down continuously in a cascade from the largest to the smallest ones. To solve numerically the Navier-Stokes equations a very fine grid is necessary in order to catch also the smallest eddies, but the direct solution of Navier-Stokes equation (DNS) is not feasible for most of the practical flows.

A new numerical approach is the Large Eddy Simulation (LES) and it can be located between DNS and RANS. In LES most of the scales of motion are directly solved, in particular all the large energy carrying scales, the ones that extract energy from the mean flow. These scales are influenced by the boundaries and they are strongly anisotropic. The smaller and dissipative scales must be modelled.

Large eddy simulation has a long tradition in geophysics, starting with the pioneering work of Smagorinsky (1963), Lilly (1967) and Deardorff (1970, 1973). All the motivations that justify numerical modelling in engineering applications are magnified in geophysical flows, where often it is simply not possible to scale the problem down to laboratory scales (Scotti,2010). Not surprisingly, given the interest of these pioneers, the boundary layer generated by winds near the surface of the Earth, the Planetary Boundary Layer (PBL), has long enjoyed a privileged relationship with LES (Scotti,2010).

Following, I will focus on oceanographic applications, an area of relatively recent LES ‘colonisation’. I would like to emphasise that this paragraph is not meant to be an exhaustive review of the application of LES to the ocean. In selecting the topics, I have tried to show that LES is a versatile tool, with a range of applications from coastal oceanography to long-term climate prediction.

The problem of deep oceanic convection, for example, induced by localized surface cooling has received considerable attention in the last years. Results from field observations (e.g., in the

Greenland Sea or the Gulf of Lions), laboratory experiments and numerical simulations have led to some theoretical predictions concerning the structure of the convective region like plume scale, chimney scale, and rim current (Raasch et al.,1997).

In “*An ocean Large-eddy simulation model with application to deep convection in the Greenland Sea (Denbo and Skyllingstad 1996)*”, a non-hydrostatic, Boussinesq, three-dimensional model, the ocean large-eddy simulation model (OLEM), has been developed to study deep oceanic convection. The model uses a subgrid-scale parameterization of turbulence developed for large-eddy simulation models and the advection of scalars is accomplished using a monotonic scheme. A set of experiment was performed using OLEM to provide a direct comparison with laboratory results and aircraft measurements of the atmospheric convective boundary layer.

In “*Modeling Deep Ocean Convection:Large Eddy Simulation in Comparison with Laboratory Experiments (Raasch and Etling 1997)*” large-eddy simulation model has been applied to study deep convective processes in a stratified ocean driven by the energetic cooling at the ocean surface. Closely related to a laboratory experiment, the numerical experiment deals with the inverted problem of the growth of a convective mixed layer driven by a localized source of bottom heating in a rotating, stably stratified fluid. In general, good agreement is found between numerical and laboratory results.

In “*Large- eddy simulation of the equatorial ocean boundary layer: Diurnal cycling, eddy viscosity, and horizontal rotation (Wang et al,1996)*” oceanic boundary layers (OBL) at the equator are studied using a large-eddy simulation model. The model has no equatorial under current and the vertical component of Earth's rotation is zero. It is forced with a constant westward zonal wind stress and with a constant surface heat flux and, in some cases, a diurnal cycle of solar heating.

In “*Large-Eddy Simulation of the Diurnal Cycle of Deep Equatorial Turbulence (Wang et al,1997)*”, the deep diurnal cycle of turbulence at the equator is studied. Based on a scale-separation hypothesis, the LES model includes the following large-scale flow terms: the equatorial undercurrent (EUC), zonal pressure gradient, upwelling, horizontal divergence, zonal temperature gradient, and mesoscale eddy forcing terms for the zonal momentum and the heat equations. The importance of these terms in obtaining a quasi-equilibrium boundary layer solution is discussed.

In “*Upper-Ocean Turbulence during a Westerly Wind Burst: A Comparison of Large-Eddy Simulation Results and Microstructure Measurements (Skyllingstad et al 1999)*” the response of the upper ocean to westerly wind forcing in the western equatorial Pacific was modeled by means of large-eddy simulation for the purpose of comparison with concurrent microstructure observations. The model was initialized using currents and hydrography measured during the Coupled Ocean–Atmosphere Response Experiment (COARE) and forced using measurements of surface fluxes over a 24-h

period. Comparison of turbulence statistics from the model with those estimated from concurrent measurements reveals good agreement within the mixed layer.

In “*Assessment of the upper-ocean mixed layer parameterizations using a large eddy simulation model (Furuichi et al 2015)*” a large eddy simulation of the upper ocean mixed layer processes in the winter north-western Pacific is carried out and compared with concurrent microstructure measurements. The authors find that dissipation rates of turbulent kinetic energy and temperature variance from LES agree well with field observations in the areas.

In “*Large Eddy Simulation of the Ocean Mixed Layer: The effects of Wave Breaking and Langmuir Circulation (Noh et al 2003)*” a large eddy simulation of the ocean mixed layer was performed in which both wave breaking and Langmuir circulation are realized. Wave breaking was represented by random forcing consistent with the observed near-surface turbulence and Langmuir circulation was realized by the Craig–Leibovich vortex force. The effects of wave breaking were found to be mainly limited to the near-surface zone of the upper few meters. Langmuir circulations below it are not significantly modified, although they become somewhat weakened and less coherent. The comparison of the results from the LES and the ocean mixed layer model also reveals the significances of wave breaking and Langmuir circulation in the vertical mixing process of the ocean mixed layer.

In “*Large eddy simulation of turbulence in ocean surface boundary layer at Zhangzi Island offshore (Shuang et al 2013)*” a large eddy simulation model is used to investigate the turbulence processes in the ocean surface boundary layer at Zhangzi Island offshore. Field measurements at Zhangzi Island during July 2009 are used to drive the LES model. The LES results capture a clear diurnal cycle in the oceanic turbulence boundary layer. The process of the heat penetration and heat distribution characteristics are analyzed through the heat flux results from the LES and their differences between two diurnal cycles are discussed as well.

In “*Large-Eddy Simulation of Flow over Two-Dimensional Obstacles: High Drag States and Mixing (Skylingstad et al 2003)*” A three-dimensional large-eddy simulation model was used to examine how stratified flow interacts with bottom obstacles in the coastal ocean. LES models have only recently been applied to geophysical problems involving topography and have focused almost exclusively on atmospheric conditions. Bottom terrain representing a 2D ridge was modeled using a finite-volume approach with ridge height (4.5 m) and width (30 m) and water depth (45 m) appropriate for coastal regions. A simulation with bottom drag, but with a much larger obstacle height (16 m) and width (400 m), produced a stronger lee-wave response, indicating that large obstacle flow is not influenced as much by bottom roughness.

3.2 LES-COAST Model

LES-COAST model (Roman et al., 2010, University of Trieste) solves the filtered form of three dimensional, non-hydrostatic Navier-Stokes equations under the Boussinesq approximation and the transport equation for salinity and temperature. Temperature and salinity are active scalars affecting the flow field.

The equations are solved with a finite difference approach accurate at the second order both in space and time. Spatial derivatives are treated with central scheme, except the convective terms, which are discretized using the QUICK, third-order accurate scheme (the QUICK option can be switched off if necessary and central differences are thus employed). The equations can be advanced in time in an explicit or semi-implicit way. The scheme used for advancing explicitly in time is the Adam-Bashfort. When the semi-implicit option is used, a Crank-Nicolson scheme is applied only to diagonal diffusive terms to overcome the diffusive stability limit on the time step.

LES-COAST works with non-staggered grid, it means that the primitive variables, like velocity, pressure, density are located at the cell centroid, while at the cell faces the fluxes are defined. The time integration of the equations is described in details in Zang et al. (1994). LES-COAST model makes use of large-eddy simulation approach to parametrize turbulence, the variables are filtered by application of a low-pass filter function represented by the size of the cells. The subgrid-scale fluxes (SGS), which come out from the filtering operation, are parametrized by a two-eddy viscosity anisotropic Smagorinsky model, to better adapt to coastal flow in which the horizontal length scale is much larger than the vertical one. Complex geometry that characterizes coastal flows is treated by Immersed Boundary Method (IBM).

3.2.1 THE GOVERNING EQUATIONS

The environmental flows are governed by the Navier-Stokes equations. In the most of the application the equations are considered under the Boussinesq approximation, according to which density variations can be neglected in continuity and in momentum equations, except in the gravity term.

The variables of Navier-Stokes equations, in LES methodology, are filtered through an application of a low-pass filter. In three dimensions the application of the filter to the variable u reads as:

$$\bar{u}(x) = \int G(x, x')u(x')dx' \quad (3.1)$$

where x is the Cartesian coordinate vector, G is the filter function, Δ is the filter width. A top-hat filter function is used:

$$G(x) = \begin{cases} \frac{1}{\Delta} & \text{if } |x| < \Delta/2 \\ 0 & \text{otherwise} \end{cases} \quad (3.2)$$

where the filter width Δ is the grid cell size; turbulence structures, with length scales smaller than Δ , have to be modelled (example is shown in figure 3.1). The filtering operation decomposes the variable u into the sum of two components: $u = \bar{u} + u_{SGS}$, where \bar{u} is the resolved component (it represents large-eddy motion) and u_{SGS} is the residual one (or subgrid- scale).

Large scale eddies continuously break up into smaller eddies until they are too small and they dissipate into heat.

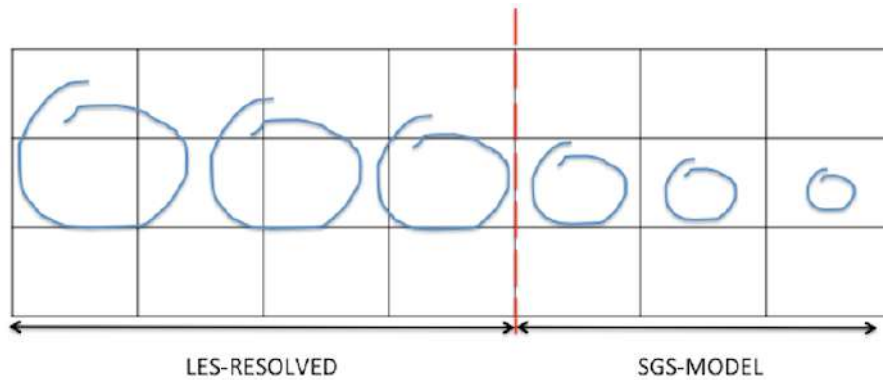


Figure 3.1: Turbulent structures with length scale bigger than the grid size are directly resolved, the smaller ones are parametrized by SGS-model

The filtered Boussinesq form of the Cartesian Navier-Stokes equations reads as follows:

Continuity equation:

$$\frac{\partial \bar{u}_j}{\partial x_j} = 0 \quad (3.3)$$

Momentum equation:

$$\frac{\partial \bar{u}_i}{\partial t} + \frac{\partial \bar{u}_i \bar{u}_j}{\partial x_j} = -\frac{1}{\rho_0} \frac{\partial \bar{p}_i}{\partial x_i} + \nu \frac{\partial^2 \bar{u}_i}{\partial x_j \partial x_j} - 2\epsilon_{ijk} \Omega_j \bar{u}_k - \frac{\bar{\rho}}{\rho_0} g_i \delta_{i,2} - \frac{\partial \tau_{ij}}{\partial x_j} \quad (3.4)$$

Temperature equation:

$$\frac{\partial \bar{T}}{\partial t} + \frac{\partial \bar{u}_j \bar{T}}{\partial x_j} = \kappa_T \frac{\partial^2 \bar{T}}{\partial x_j \partial x_j} - \frac{\partial \lambda_j^T}{\partial x_j} \quad (3.5)$$

Salinity equation:

$$\frac{\partial \bar{S}}{\partial t} + \frac{\partial \bar{u}_j \bar{S}}{\partial x_j} = \kappa_S \frac{\partial^2 \bar{S}}{\partial x_j \partial x_j} - \frac{\partial \lambda_j^S}{\partial x_j} \quad (3.6)$$

where ‘ $\bar{\cdot}$ ’ represents the filtering operation, u_i represents the i^{th} -component of the Cartesian velocity vector (u, v, w), x_i represents the i^{th} -component of the Cartesian coordinates (x, y, z) (x and z denote horizontal direction, and y vertical one), t is time, ρ_0 is the reference density, \bar{p} is the filtered pressure, ν is the kinematic viscosity, ϵ_{ijk} is the Levi-Civita tensor, Ω_i is the i^{th} -component of the Earth rotation vector, $\Delta\rho$ is the density anomaly, g_i is the i^{th} -component of the gravity vector, and τ_{ij} is the SGS stress which comes from the non-linearity of the advection term. T is temperature (K), S is salinity (PSU), κ^T and κ^S are respectively temperature and salinity diffusivity, λ_j^T the SGS temperature fluxes, while λ_j^S the salinity ones. Temperature and salinity are related to density through the state equation:

$$\frac{\Delta\rho}{\rho_0} = \frac{\rho - \rho_0}{\rho_0} = \beta^T(T - T_0) + \beta^S(S - S_0) \quad (3.7)$$

where ρ_0 is the reference density at the temperature T_0 and salinity S_0 ; β^T and β^S are respectively the coefficient of temperature expansion and saline contraction.

Curvilinear Coordinates

The above equations are written in a Cartesian frame of reference. Coastal domains are often characterised by a complex geometry thus, a curvilinear grid adapts better to such areas, following closely the coastline. Figure 3.2 shows an example of coordinates transformation between the physical and the computational space.

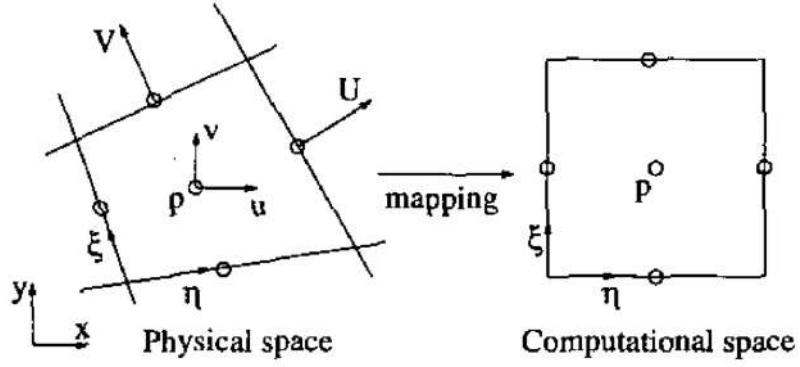


Figure 3.2: Control volume of a non-staggered grid and the mapping in two dimensions (Zang et al. 1994).

The governing equation transformed in curvilinear form are:

$$\frac{\partial U_m}{\partial \xi_m} = 0 \quad (3.8)$$

$$\frac{\partial J^{-1}u_i}{\partial t} + \frac{\partial F_{im}}{\partial \xi_m} = J^{-1}B_i \quad (3.9)$$

in which B_i is including the gravitational term and F_{im} is defined as:

$$F_{im} = U_m u_i + J^{-1} \frac{\partial \xi_m}{\partial x_i} p - \nu G^{mn} \frac{\partial u_i}{\partial \xi_n} \quad (3.10)$$

where ξ_m ($m=1,2,3$) are the coordinates in transformed computational space ($\xi(x,y,z), \eta(x,y,z), \zeta(x,y,z)$), and

$J^{-1} = \det \left(\frac{\partial x_i}{\partial \xi_j} \right)$ inverse of the Jacobian, it represents the volume of the cell.

$U_m = J^{-1} \frac{\partial \xi_m}{\partial x_j} u_j$ is the volume flux normal to the surface of constant ξ_m

$G^{mn} = J^{-1} \frac{\partial \xi_m}{\partial x_j} \frac{\partial \xi_n}{\partial x_j}$ mesh skewness tensor

The transformed pressure term represents the flux of the pressure gradient through the faces of the cell in the physical domain, while the third term on the right-hand side of equation (3.10) is the transformed diffusive term, which represents the fluxes of the viscous stresses through the cell faces of the cell.

3.2.2 NUMERICAL METHOD

A non-staggered grid it is used; Cartesian velocities, pressure and body forces are defined in the centre of the cell; velocity fluxes are defined in the mid-point of their corresponding face cells.

Following Kim and Moin (1985) and Zang et al. (1994), in the LES-COAST the equations are integrated in time using a semi-implicit fractional step method, accurate to second-order, with the Adams-Bashforth method for the explicit terms and the Crank-Nicholson method for the implicit terms (diagonal diffusive terms) to remove the viscous stability limit for the time step.

Spatial derivatives are approximated using centered second-order finite differences, except for the advective terms, which are discretized using a 3rd-order accurate upwind scheme (QUICK), which calculates the face value from the nodal values using a quadratic upwind interpolation, to make the simulation more stable.

The pressure equation is solved using a line-SOR algorithm, with line solution in the vertical direction and point iteration in the horizontal directions, in conjunction with a Multigrid technique to speed up the convergence.

The discretized equations are:

Continuity equation:

$$\frac{\partial U_m}{\partial \xi_m} = 0 \quad (3.11)$$

Momentum equation:

$$J^{-1} \frac{u_i^{n+1} - u_i^n}{\Delta t} = \frac{3}{2} (C(u_i^n) + D_E(u_i^n) + B_i^n) - \frac{1}{2} (C(u_i^{n-1}) + D_E(u_i^{n-1}) + B_i^{n-1}) \\ + R_i(p^{n+1}) + \frac{1}{2} (D_I(u_i^{n+1} + u_i^n)) \quad (3.12)$$

where $\partial/\partial \xi_m$ stands for the discrete finite difference operators in the computational space; superscripts represent the time step, C represents the convective term, R_i is the discrete operator for the pressure gradient term; D_E and D_I represent respectively the off-diagonal viscous terms (treated explicitly) and the diagonal viscous terms (treated implicitly); B_i represents the body forces like Coriolis and buoyancy.

They are:

$$C_i = -\frac{\partial}{\partial \xi_m} (U_m u_i) \quad (3.13)$$

$$R_i = -\frac{\partial}{\partial \xi_m} \left(J^{-1} \frac{\partial \xi_m}{\partial x_i} \right) \quad (3.14)$$

$$D_I = \frac{\partial}{\partial \xi_m} \left(\nu G^{mn} \frac{\partial}{\partial \xi_n} \right) \quad m = n \quad (3.15)$$

$$D_E = \frac{\partial}{\partial \xi_m} \left(\nu G^{mn} \frac{\partial}{\partial \xi_n} \right) \quad m \neq n \quad (3.16)$$

The momentum equation (eq. 3.12) is solved by applying the fractional step method.

It consists in splitting the solution procedure in two steps: *predictor* and *corrector* part. The former part solves the *intermediate velocity* u^* which satisfy the advective and diffusive transport and body force action:

$$\begin{aligned} \left(I - \frac{\Delta t}{2J^{-1}} \right) (u_i^* - u_i^n) = \frac{\Delta t}{J^{-1}} \left[\frac{3}{2} (C_i^n + D_E(u_i^n) + B_i^n) - \right. \\ \left. \frac{1}{2} (C_i^{n-1} + D_E(u_i^{n-1}) + B_i^{n-1}) + R_i(p^{n+1}) + \frac{1}{2} (D_I(u_i^{n+1} + u_i^n)) \right] \end{aligned} \quad (3.17)$$

in which I is the identity matrix. The *corrector* step finds u_i^{n+1} by means of u^* , which satisfies the continuity equation, both velocities are related to the pressure gradient by:

$$u_i^{n+1} - u_i^* = \frac{\Delta t}{J^{-1}} [R_i(\phi^{n+1})] \quad (3.18)$$

the variable ϕ is related to p as follows:

$$R_i(p) = \left(J^{-1} - \frac{\Delta t}{2} D_I \right) \left(\frac{R_i(\phi)}{J^{-1}} \right) \quad (3.19)$$

By interpolating the 3.18 to the cell's faces it is obtained:

$$U_m^{n+1} = U_m^n - \Delta t \left(G^{mn} \frac{\partial \phi^{n+1}}{\partial \xi_n} \right) \quad (3.20)$$

in which U_m^* is the intermediate volume flux and it is defined as: $U_m^{n+1} = J^{-1} (\partial \xi_m / \partial x_j) u_j^*$.

By substituting 3.20 into the continuity equation finally it is obtained the Poisson equation for ϕ^{n+1}

$$\frac{\partial}{\partial \xi_m} \left(G^{mn} \frac{\partial \phi^{n+1}}{\partial \xi_n} \right) = \frac{1}{\Delta t} \frac{\partial U_m^*}{\partial \xi_m} \quad (3.21)$$

which is solved by a multigrid method.

3.2.3 SUB-GRID SCALE (SGS) MODEL

In LES the large eddies are resolved directly whereas the small sub-grid scales are modelled using a SGS model to approximate the SGS Reynolds stress τ_{SGS} .

The most commonly used SGS model is the one proposed by Smagorinsky (1963). The classical Smagorinsky model assumes that the anisotropic part of the subgrid-scale stress tensor τ_{ij}^{SGS} is related to the resolved strain rate tensor $\overline{S_{ij}}$ through a SGS eddy viscosity ν_T as follows:

$$\tau_{ij} - \frac{1}{3}\tau_{kk}\delta_{ij} = -2\nu_T\overline{S_{ij}} = -\nu_T\left(\frac{\partial\bar{u}_i}{\partial x_j} + \frac{\partial\bar{u}_j}{\partial x_i}\right) \quad (3.22)$$

where ν_T is the SGS eddy viscosity parameter which can be defined as the product of a length scale $C\Delta$, proportional to the grid size and a velocity scale $C\Delta|\bar{S}|$, where C is an empirical constant and $|\bar{S}|$ is the contraction of the resolved strain rate tensor.

Finally, the eddy viscosity can be written as:

$$\nu_T = (C\Delta)^2|\overline{S_{ij}}| \quad (3.23)$$

This classic SGS Smagorinsky model approach is designed for isotropic or nearly isotropic grids. However, in the case of coastal areas finding a unique length scale representative of the three dimensions of the cells could lead to an overestimation of the eddy viscosity in all directions because of the strong anisotropy of the cells used to discretize the domain. In order to overcome this problem, the anisotropic Smagorinsky model (ASM) developed by Roman et al. (2010) has been adopted. The model uses a two-SGS-eddy-viscosity (vertical and horizontal) concept.

The quantities are defined as:

$$\nu_{\tau,V} = (C_V L_V)^2 |\overline{S_V}| \quad (3.24)$$

$$\nu_{\tau,H} = (C_H L_H)^2 |\overline{S_H}| \quad (3.25)$$

where $L_H = \sqrt{\Delta_x^2 + \Delta_y^2}$ and $L_V = \Delta_z$

C_V and C_H are two empirical constants calculated from the grid aspect-ratio as illustrated in figure 3.3; $|\overline{S_V}|$ and $|\overline{S_H}|$ are respectively the contraction of the vertical and horizontal, resolved, strain rate tensor; they are defined as follows:

$$|\overline{S_V}| = \sqrt{4\overline{S_{13}}^2 + 2\overline{S_{33}}^2 + 4\overline{S_{23}}^2} \quad (3.26)$$

$$|\overline{S_H}| = \sqrt{2\overline{S_{11}}^2 + 2\overline{S_{22}}^2 + 4\overline{S_{12}}^2} \quad (3.27)$$

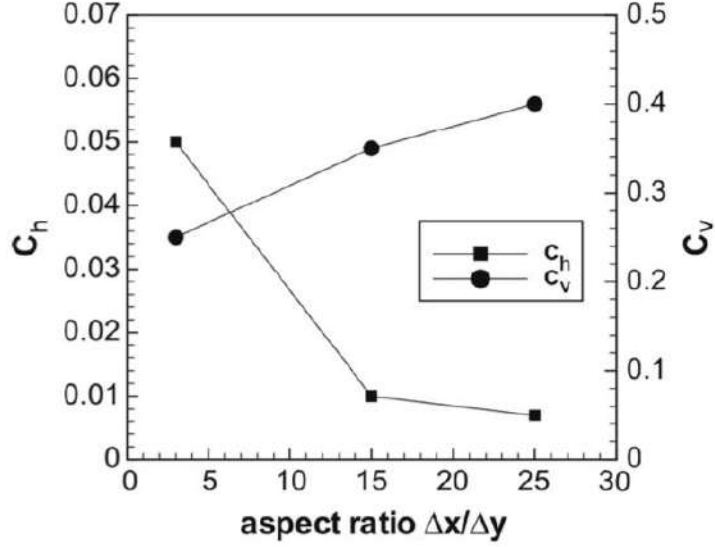


Figure 3.3: Variation of the empirical constants C_h and C_v with the grid anisotropy (Roman et al 2010).

Like momentum equations, the filtering operation of scalar transport equations introduces the residual subgrid-scale fluxes $q_i^{SGS} = \lambda_i^T$ in the temperature equation and $q_i^{SGS} = \lambda_i^S$ in the salinity equation:

$$q_i^{SGS} = \overline{u_i \rho} - \bar{u}_i \bar{\rho} \quad (3.28)$$

where ρ represents the scalar quantity (temperature or salinity). The SGS fluxes q_i^{SGS} need to be parametrized; An eddy diffusivity model is used, in which the SGS fluxes are treated in analogy to the SGS stresses:

$$q_i^{SGS} = \Gamma_t \frac{\partial \bar{\rho}}{\partial x_i} \quad (3.29)$$

where Γ_t is the SGS eddy-diffusivity and it is calculated by assuming that the SGS eddy viscosity and the SGS eddy diffusivities are proportional through the SGS Prandtl number Pr_{SGS} (in the case of temperature) and Schmidt number Sc_{SGS} (in the case of salinity). SGS Prandtl and Schmidt numbers are defined as follows:

$$Pr_{SGS} = \frac{u_{SGS}}{\Gamma_t^T}, Sc_{SGS} = \frac{u_{SGS}}{\Gamma_t^S} \quad (3.30)$$

These constants are set $Pr_{SGS} = Sc_{SGS} = 0.8$ as suggested in literature (Armenio and Sakar,2002)

3.2.4 BOUNDARY CONDITIONS OVER SOLID BOUNDARIES

The complexity of the coastal areas is treated using a combination of a curvilinear grid and the Immersed Boundary Method (IBM). The improved method for curvilinear coordinates is presented in Roman et al., 2009. IBM method is used to reproduce coastline and bathymetry by adding a body force in Navier-Stokes equations to mimic the presence of a solid boundary.

Application of the immersed boundary methodology requires the identification in the computational domain of solid nodes, located in the solid phase and fluid nodes, lying in the fluid phase; when a fluid node is surrounded by at least one solid node it is classified as immersed boundary node (IB). Figure 3.4 shows the three kinds of nodes in a two-dimensional domain. The technique used to identify solid and fluid nodes is briefly described in figure 3.5

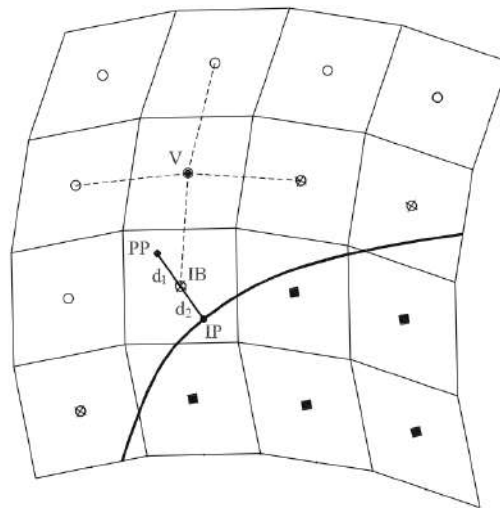


Figure 3.4: Identification, for a two-dimensional grid, of solid nodes (small solid squares), fluid nodes (small empty circles) and immersed boundary nodes, IB (small circles marked with a cross) (Roman et al 2009).

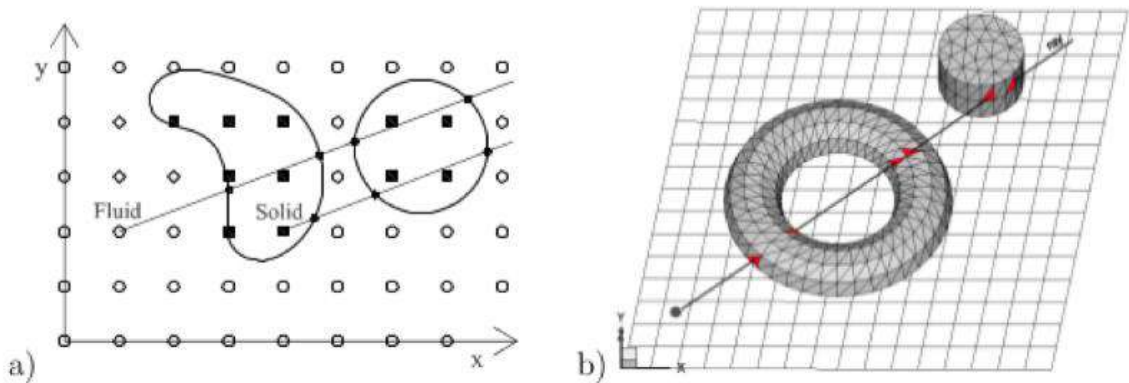


Figure 3.5: Ray-tracing technique is applied to identify fluid and solid nodes in the computational domain: scheme of the method in a two- dimensional domain fig. a) and in a three-dimensional one fig. b) (Roman et al 2009).

Coastal flows are characterized by very high Reynolds number, but the computational cost of LES resolving the near-wall viscous layer (wall-resolving LES) is proportional to $Re^{2.5}$ (Piomelli, 2008), limiting such a class of simulations to low values of Re (Petronio et al. 2013).

The problem is overcome by skipping the direct solution in the near-wall sub-layer and parametrizing the wall shear stress by using a wall-function. This is the strategy adopted in LES-COAST (Petronio et al. 2013). Specifically, two different approaches are adopted for body-fitted solid boundaries or immersed boundaries (as illustrated in Petronio et al. 2013). For body-fitted solid boundaries the logarithmic law of the wall is used at the first node off the wall:

$$u^+(1) = \frac{1}{k} \log(y^+(1)) + B \quad (3.31)$$

where $u^+(1)$ is the tangential velocity at the first grid point off the wall, made non-dimensional with the friction velocity u_τ , $k = 0.41$ is the von Karman constant, $y^+(1)$ is the distance of the first computational mesh point from the wall, scaled with the viscous length scale ν/u_τ and B is a coefficient which also includes roughness effects. This equation is solved iteratively to determine the friction velocity used to compute the wall shear stress, which is employed as a boundary condition.

This technique cannot be applied to solid walls reproduced using immersed boundaries, since the grid face generally does not coincide with the surface of the immersed body (Petronio et al. 2013). In order to overcome this issue, a novel approach, proposed by Roman et al. (2009), is used. It consists of a two-step method: first the velocity of the first off-the-wall node, with respect to the immersed boundary, is calculated, employing the velocity field from the interior flow (Petronio et al. 2013). Second, a RANS-like eddy viscosity is set at the interface between the fluid region and the solid one as $\nu_t = k u_\tau y$, where y is the distance between the first fluid node and the surface of the immersed boundary. Details of the method are discussed in Roman et al. (2009).

Chapter 4 – Wind Driven Circulation

Before proceeding to develop a nesting, the ability of two codes to simulate a flow in a simple closed domain has been tested.

For this purpose, idealized simulations have been used to examine and to compare the flow field, the turbulent kinetic energy and the eddy viscosities developed by the two different models. In this way a series of numerical simulations have been conducted and the goal has been to compare the results derived from the two modelling approaches: Ocean General Circulation Model (MITgcm) and a LES, which has been used as our ground truth.

The numerical experiments, carried out by the use of MITgcm, were configured as similarly as possible to the LES settings, even though it was not a trivial matter to set them up in an identical fashion. Although comparing these two different modelling approaches has been not a trivial task, given that the former is configured in terms of dimensional variables while non-dimensional variables are used in the latter, it has been a valuable way of testing the accuracy of MITgcm when the scales fall below the mesoscale regime.

4.1 Models Configuration

All simulations are performed for 48 hours ($\Delta t=3$ sec) with a constant westerly wind of 10 m/s, giving rise to a homogeneous steady wind case. Coriolis is neglected and the flow is neutrally buoyant and incompressible. The rectangular domain (measuring 1280m X 640m X 32m) is discretized in 256 x 128 grid cells in horizontal direction and 32 cells in vertical direction. With this discretization, the dimensions of the cells are about $\Delta x \approx \Delta y \approx 5$ m and $\Delta z \approx 1$ m.

The effect of the wind imposed over the free surface is taken into account by means of the formula proposed in Wu (1982). The induced stress at the sea surface, τ , is initially computed from the wind velocity 10 m above the mean sea level (U_{10}) through:

$$\tau_0 = \rho_a C_{10} U_{10}^2 \quad (4.1)$$

where ρ_a is the air density and C_{10} is the drag coefficient parameter which is calculated as a function of wind speed as:

$$C_{10} = (0.8 + 0.065 U_{10}) 10^{-3} \quad (4.2)$$

4.2 LES-Coast Simulation

In this section we discuss the results of the simulation performed by the LES-Coast model: first we describe the instantaneous flow field; successively we discuss about turbulent kinetic energy and the eddy viscosities.

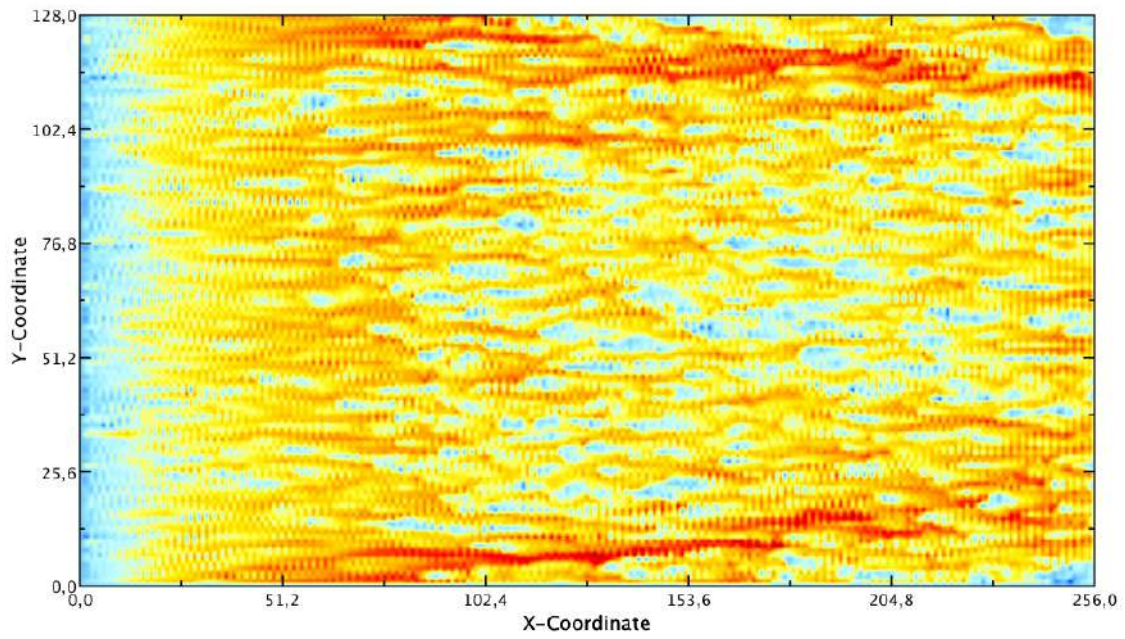
4.2.1 INSTANTANEOUS FIELD

As a representative example of the wind-driven circulation occurring in a such simplified domain, snapshots of velocity field have been extracted at the end of simulation (when the flow has reached the steady state).

Figures 4.1 (A)-(B) and 4.2 (A)-(B) provide the contour plot of U and V component of the horizontal velocity at different horizontal planes and transect (Fig.4.3). It is possible to perfectly observe the presence of turbulent structures, streaks of higher and slower horizontal velocities. The figures show that at the surface the current is aligned to wind direction (the component V is mostly equal to zero in the whole domain, meanwhile the component U is aligned with the wind direction), but close to the bottom the velocity field is reversed with respect to the wind direction. Specifically, by looking at the vertical profile of the streamwise velocity, shown in figure 4.3, it is possible to appreciate how the U component inverts its direction below 10 m depth.

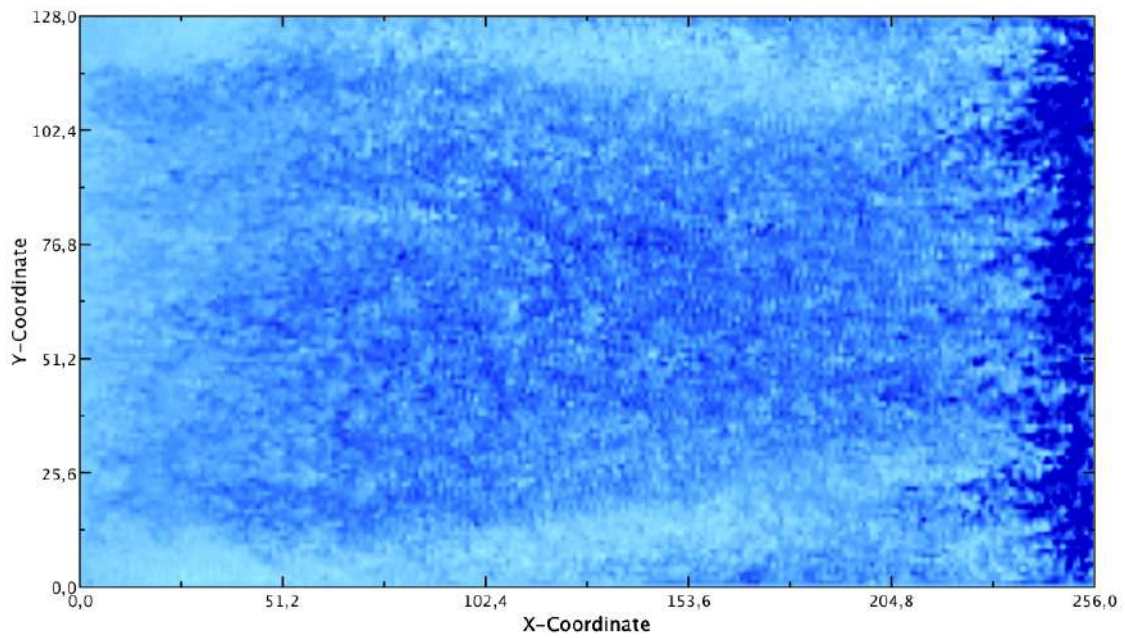
The inversion of current between the surface and bottom is the effect of the downwelling along the eastern side of the domain and the consequently upwelling along the western side of the domain. This feature is perfectly shown in figure 4.4, that provides the contour plot of the vertical velocity. It is possible to observe an intense vertical mixing along the domain, with an emphasized negative velocity (blue colour) on the eastern side opposed to a strong positive velocity (red colour) on the western side.

Velocity_u at -0,5m



A)

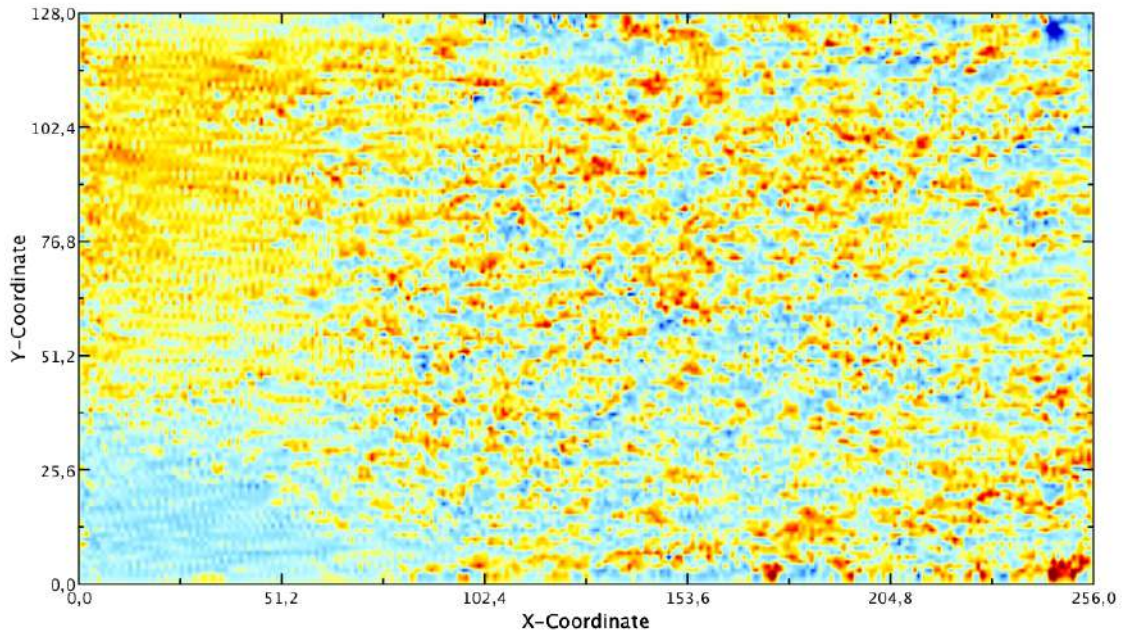
Velocity_u at -31,5m



B)

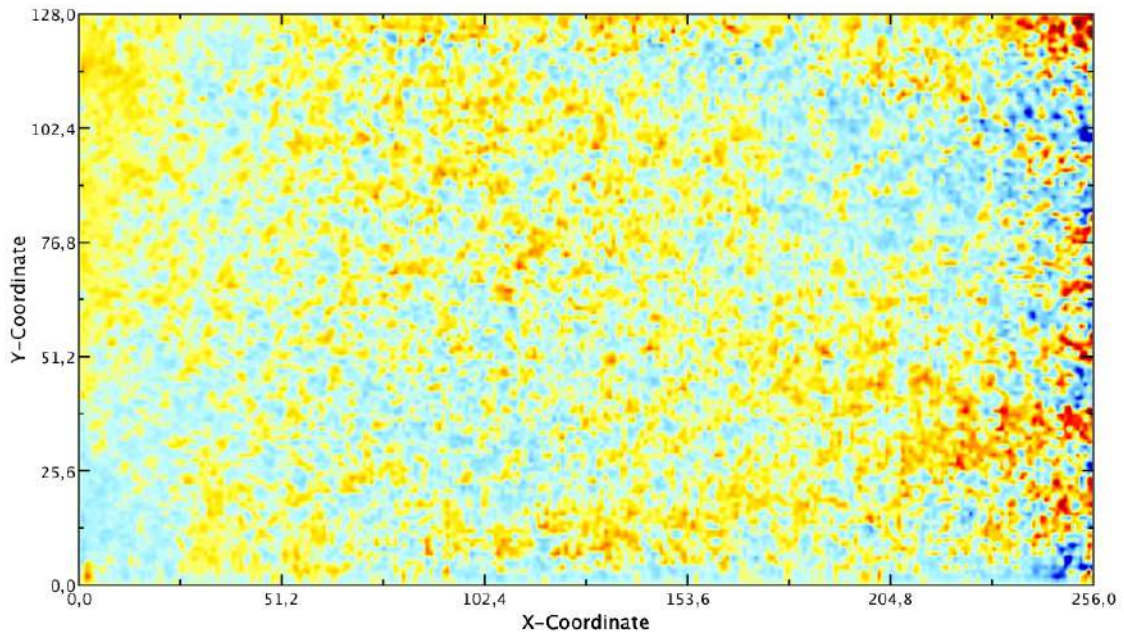
Fig.4.1: Contour plot of U component of the horizontal instantaneous velocity at two horizontal planes: (A) -0,5m; (B) -31,5m. Grid cells are shown on x and y axes; Resolution 5 m.

Velocity_v at -0,5m



A)

Velocity_v at -31,5m



B)

Fig.4.2: Contour plot of V component of the horizontal instantaneous velocity at two horizontal planes: (A) -0,5m; (B) -31,5m. Grid cells are shown on x and y axes; Resolution 5 m.

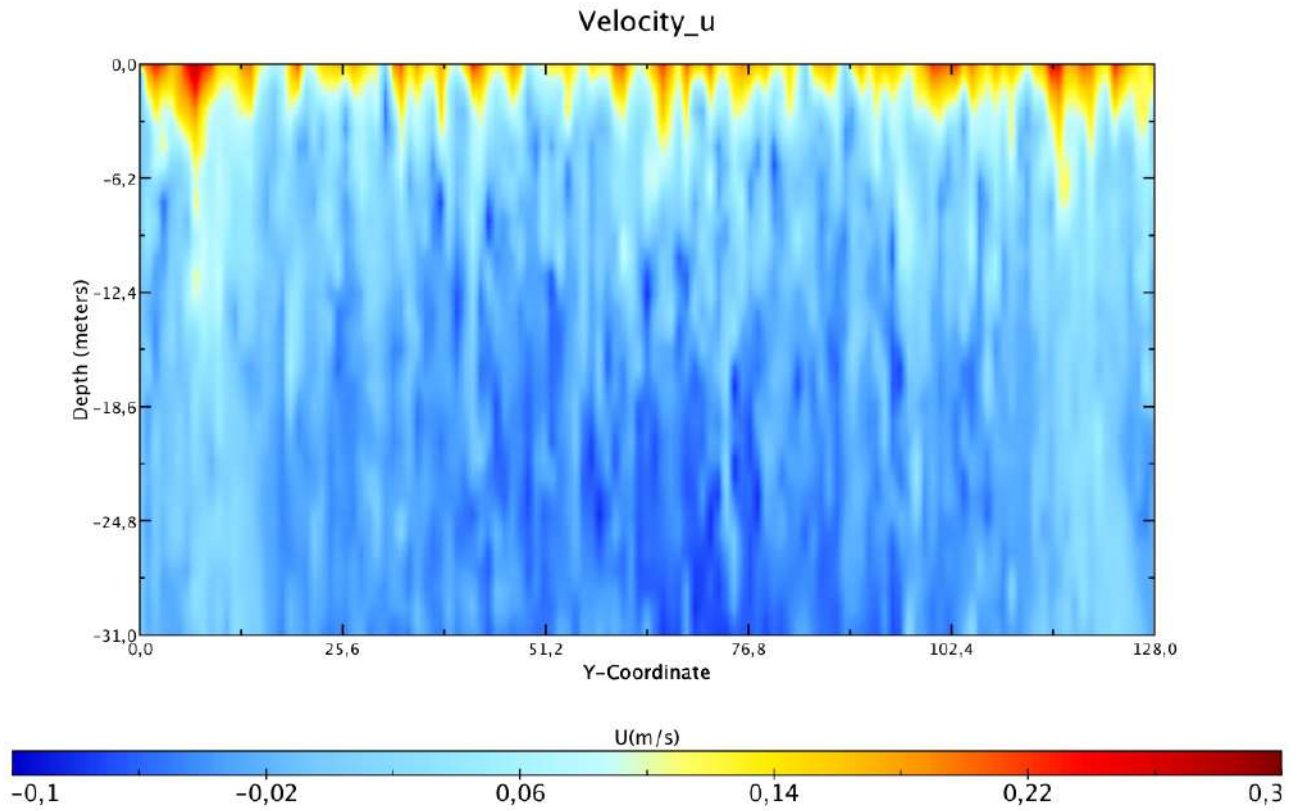


Fig.4.3: Contour plot of U component of the horizontal instantaneous velocity in a vertical plane. Grid cells are shown on y-coord; Resolution 5 m.

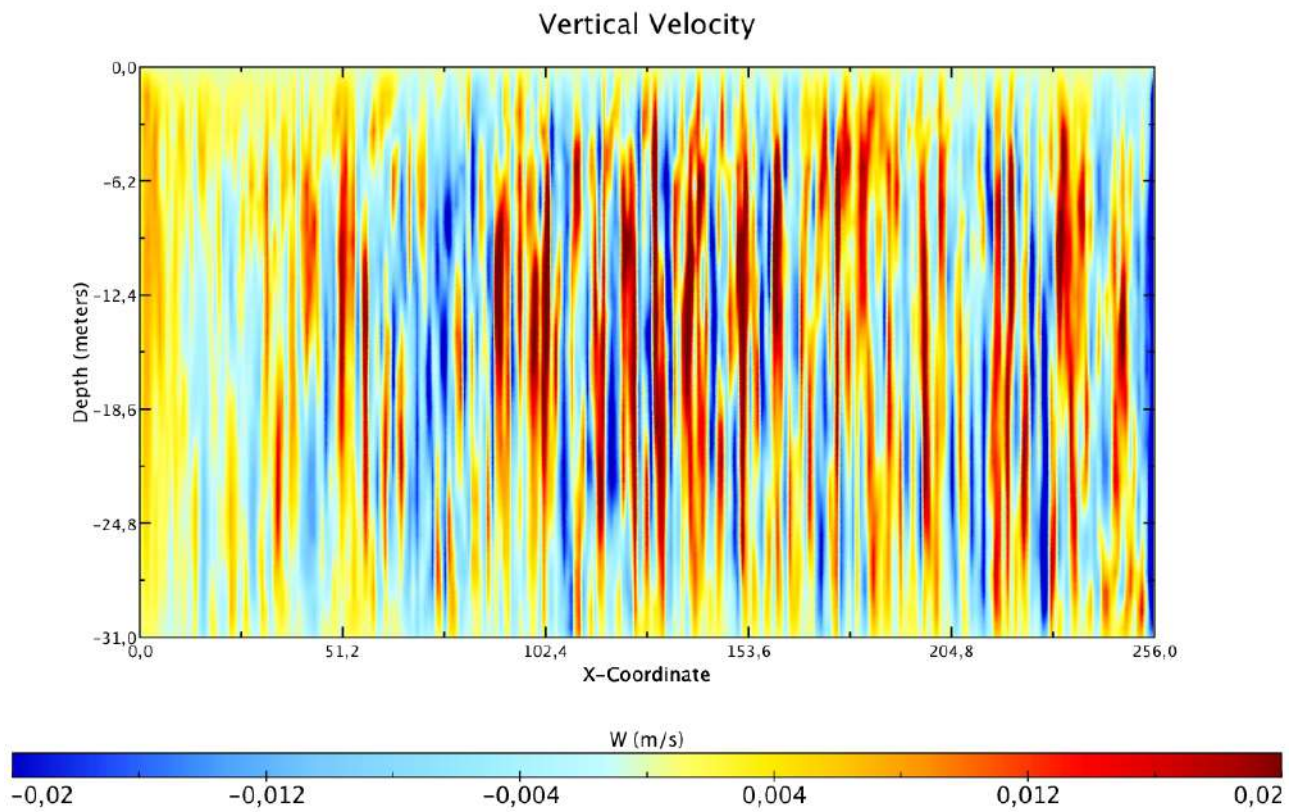


Fig.4.4: Contour plot of W component of the vertical instantaneous velocity in a vertical plane. Grid cells are shown on x-coord; Resolution 5 m.

4.2.2 TURBULENT KINETIC ENERGY

The turbulent kinetic energy (TKE) is examined to illustrate horizontal and vertical distribution of turbulent intensity:

$$TKE = \frac{1}{2} (\tilde{u}'\tilde{u}' + \tilde{v}'\tilde{v}' + \tilde{w}'\tilde{w}') \quad (4.3)$$

Figure 4.5 shows TKE at the surface. We can observe that TKE is higher where we noticed streaks with higher values.

Figure 4.6 illustrates the vertical distribution of turbulent kinetic energy. High values of TKE are observed close to the free surface and small values are detected at the bottom. The reduction of TKE from the surface to the bottom confirms that the main source of turbulence is provided by the wind stress.

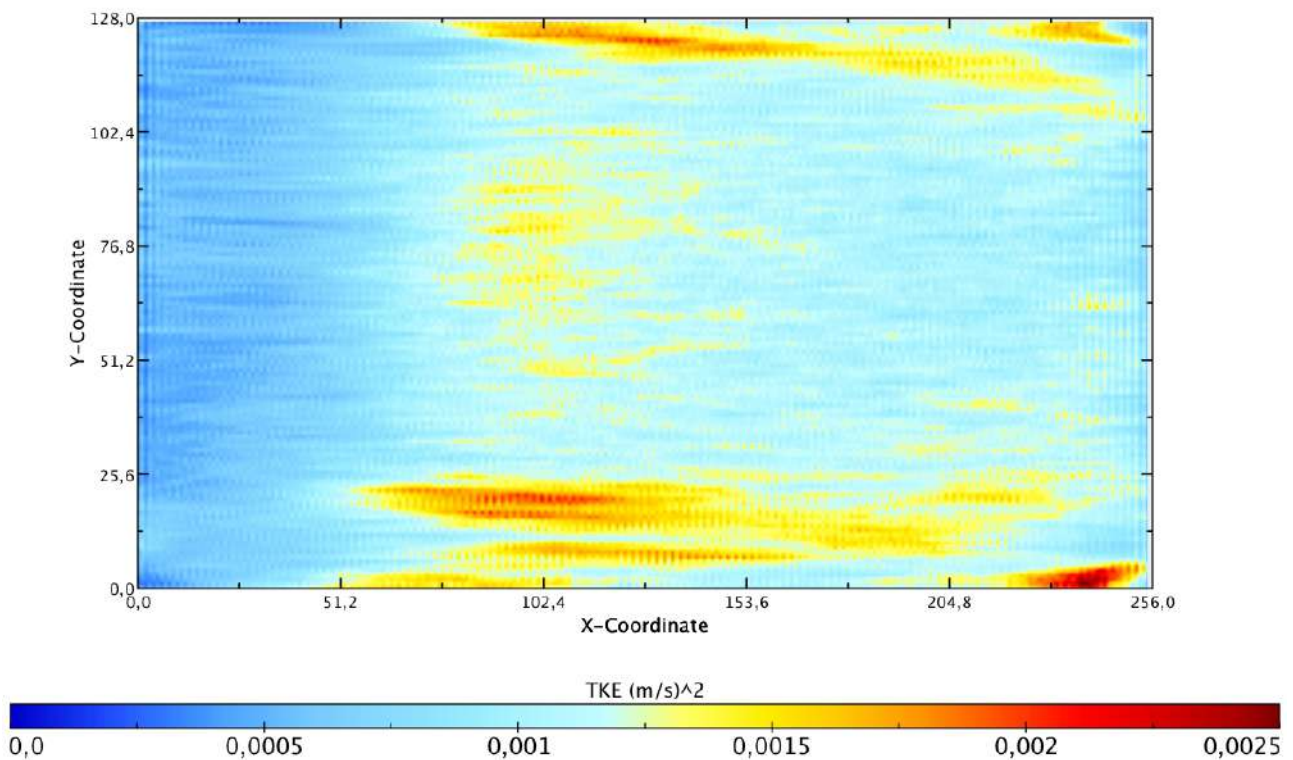


Fig.4.5: Turbulent kinetic energy at the surface; Grid cells are shown on x and y axes; Resolution 5 m.

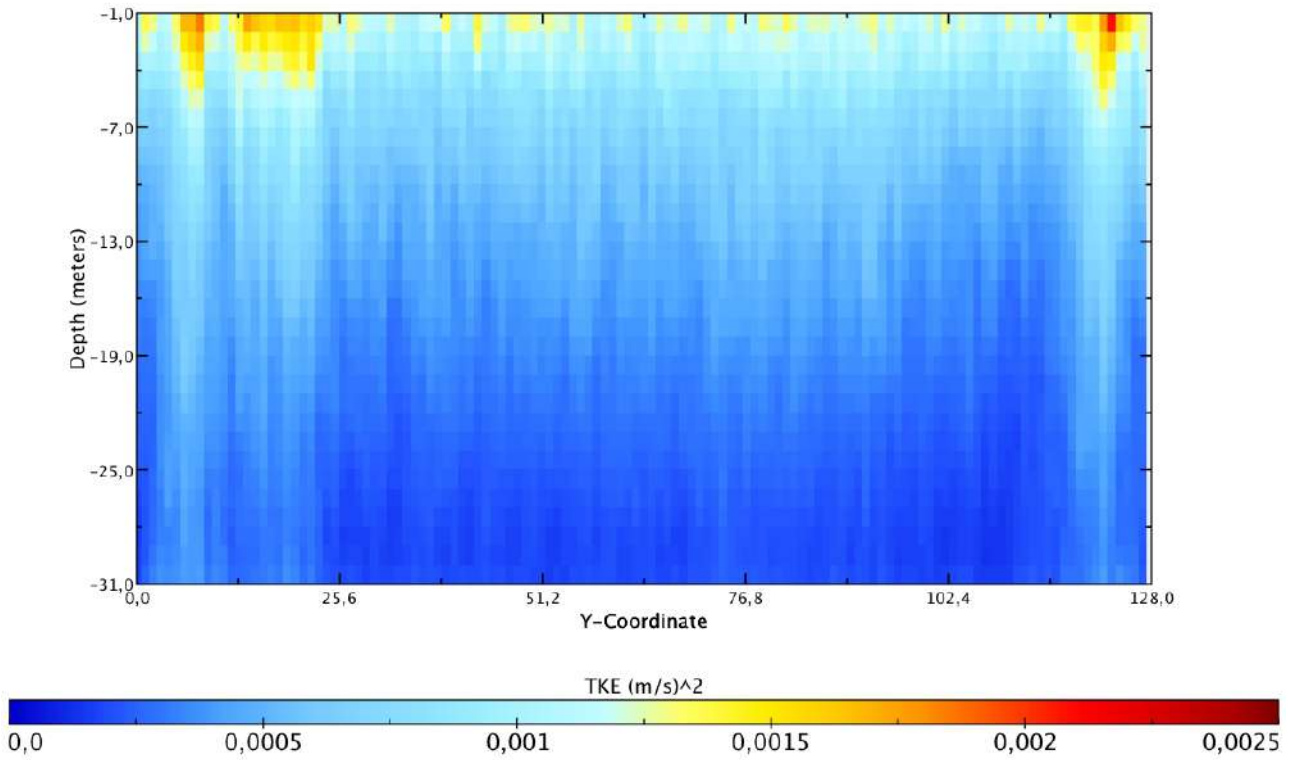


Fig.4.6: Vertical distribution of turbulent kinetic energy. Vertical plane, grid cells are shown on y-coord; Resolution 5 m.

4.2.3 EDDY VISCOSITIES

The concept of eddy viscosity is based on the gradient-diffusion hypothesis which assumes the anisotropic Reynolds stress tensor be aligned with the mean rate of the strain tensor. Although such an assumption is somehow crude (Kundu, 2004), it is generally accepted in the scientific and engineering communities.

The horizontal and vertical eddy viscosities are expressed respectively as:

$$v_H = \frac{\sqrt{\overline{u'v'^2}}}{\sqrt{\left(\frac{\partial \tilde{u}}{\partial y} + \frac{\partial \tilde{v}}{\partial x}\right)^2}} + v_{\tau,H} \quad (4.4)$$

$$v_V = \frac{\sqrt{\overline{u'w'^2} + \overline{v'w'^2}}}{\sqrt{\left(\frac{\partial \tilde{u}}{\partial z}\right)^2 + \left(\frac{\partial \tilde{v}}{\partial z}\right)^2}} + v_{\tau,V} \quad (4.5)$$

where $v_{\tau,H}$ and $v_{\tau,V}$ are respectively the SGS contribution of Eq. 3.24 and 3.25

Note that in this work the eddy viscosities have been calculated by using the Reynolds stresses and velocity gradients obtained in an operation of post-processing.

The horizontal eddy viscosity ($\nu_{\tau,H}$) (Fig.4.7), calculated with eq. 4.4, exhibits substantial inhomogeneity along the horizontal plane, with values from 0.1 to 0.3 m^2/s . This feature remains constant along the depth.

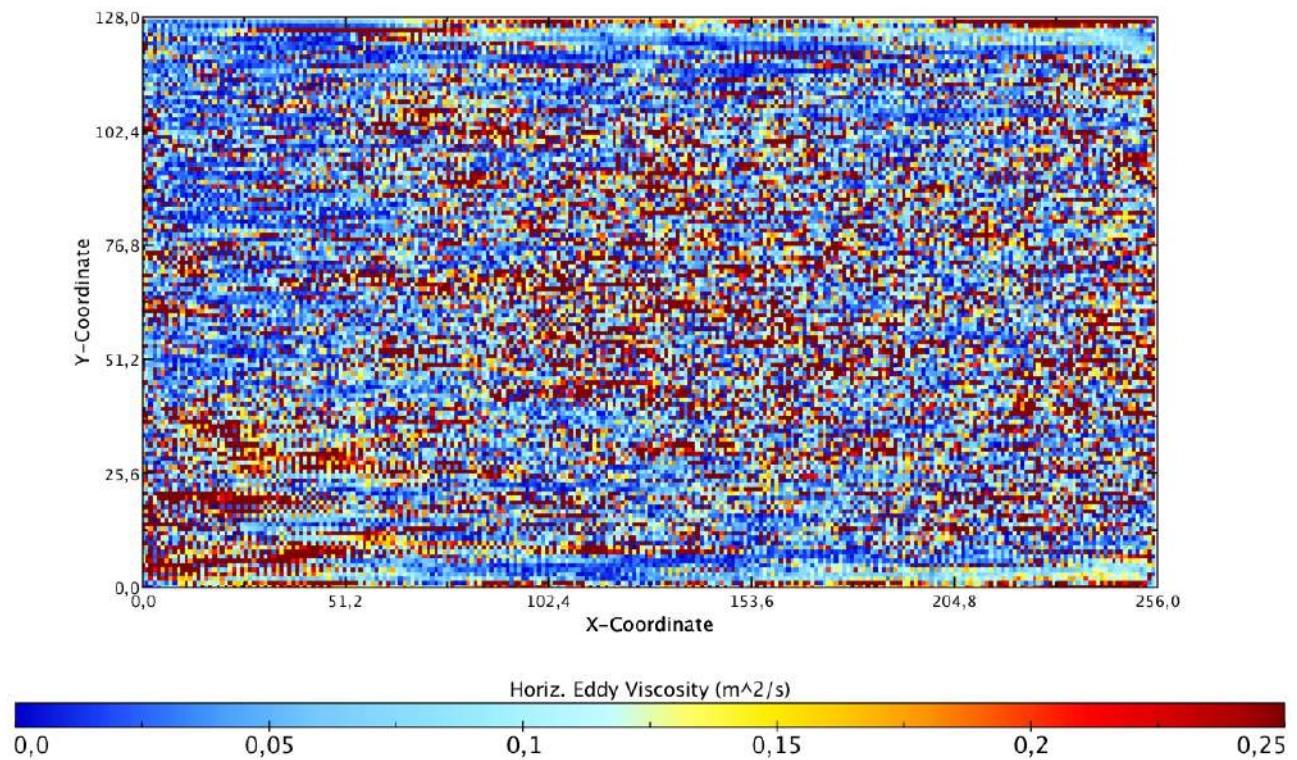


Fig.4.7: Horizontal distribution of horizontal eddy viscosity at the surface. Grid cells are shown on x and y axes; Resolution 5 m.

Figure 4.8 illustrates the vertical distribution of vertical eddy viscosity ($\nu_{\tau,v}$), calculated with eq. 4.5.

This distribution qualitatively agrees with that of Zikanov et al (2003) for a LES of an infinite Reynolds number surface Ekman layer. Specifically, in the surface layer the vertical eddy viscosity increases with depth reaching its maximum at around -20m. The vertical eddy viscosity is larger along the eastern side, due to the presence of the boundary layer associated to a strong downwelling region.

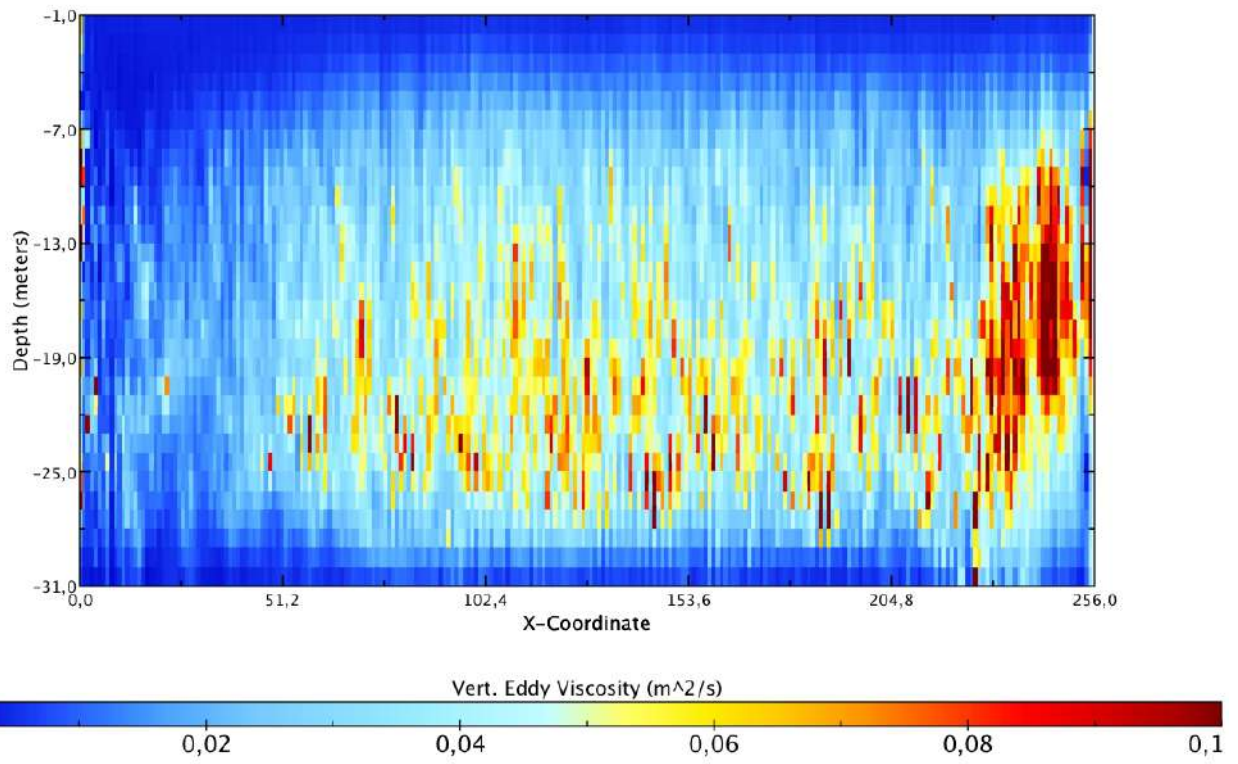


Fig.4.8: Vertical distribution of vertical eddy viscosity. Vertical plane, grid cells are shown on x-coord; Resolution 5 m.

4.3 MITgcm Simulations

In this section we discuss the results of the simulations performed by the use of MITgcm model.

First of all, a sensitivity analysis and calibration have been carried out in the application of the MITgcm to simulate the response of the closed channel to wind forcing. Understanding model sensitivity has been a vital initial step, thereby enabling the exploration of efficient high-resolution non-hydrostatic simulations, which will demand significant computational effort.

The performance of different vertical and horizontal mixing parameterizations has been analysed to assess in what aspects they differ.

As a first step, simulations with different constant values of eddy viscosity for the horizontal component and enhanced with the vertical mixing scheme developed by Gaspar et al. 1990 (hereafter GGL90) have been compared.

As a second step, simulations enhanced with “Leith Viscosity” for the horizontal parameterization and with the GGL90 scheme for the vertical component have been compared.

Finally, the same simulations, but with coarse resolution, have been run.

Nonlinear Viscosities for Large Eddy Simulation

In Large Eddy Simulations (LES), a turbulent closure needs to be provided that accounts for the effects of sub-grid scale motions on the large scale. With sufficiently powerful computers, we could resolve the entire flow down to the molecular viscosity scales ($L_v \approx 1\text{cm}$). Current computation allows perhaps four decades to be resolved, so the largest problem computationally feasible would be about 10m (Adcroft et al., 2014).

Parameterizations of Eddy Viscosity

MITgcm users can select from different parameterizations, among which: “Reynolds-Number Limited Eddy Viscosity”, “Smagorinsky Viscosity”, “Leith Viscosity”; the latest has been selected in this study.

Leith Viscosity

Leith (1996) finds an alternative to the Smagorinsky viscosity by focusing on resolving the direct enstrophy cascade in 2D turbulence rather than the direct energy cascade in 3D turbulence (Fox-Kemper 2008).

Leith (1968, 1996) notes that 2-d turbulence is quite different from 3-d. In two-dimensional turbulence, energy cascades to larger scales, so there is no concern about resolving the scales of energy dissipation. Instead, another quantity, enstrophy (which is the vertical component of vorticity squared) is conserved in 2-d turbulence and it cascades to smaller scales where it is dissipated.

Following a similar argument to that Smagorinsky about energy flux, the enstrophy flux is estimated to be equal to the positive-definite gridscale dissipation rate of enstrophy.

By dimensional analysis, the enstrophy-dissipation scale is $L_\eta(A_{hLeith}) \propto \pi A^{1/2} \eta^{-1/6}$

The Leith-estimated length scale of enstrophy-dissipation and the resulting eddy viscosity are:

$$L_\eta(A_{hLeith}) \propto \pi A_{hLeith}^{1/2} \eta^{-1/6} = \pi A_{hLeith}^{1/3} |\nabla\omega_3|^{-1/3} \quad (4.6)$$

$$A_{hLeith} = \left(\frac{viscC2Leith}{\pi} \right)^3 L^3 |\nabla\omega_3| \quad (4.7)$$

$$|\nabla\omega_3| \equiv \sqrt{\left[\frac{\partial}{\partial x} \left(\frac{\partial \bar{v}}{\partial x} - \frac{\partial \bar{u}}{\partial y} \right) \right]^2 + \left[\frac{\partial}{\partial y} \left(\frac{\partial \bar{v}}{\partial x} - \frac{\partial \bar{u}}{\partial y} \right) \right]^2} \quad (4.8)$$

Holland (1978) suggested that eddy viscosities ought to be focuses on the dynamics at the grid scale, as larger motions would be 'resolved'. To enhance the scale selectivity of the viscous operator, he suggested a biharmonic eddy viscosity instead of a harmonic (or Laplacian) viscosity. Griffies and Hallberg (2000) propose that if one scales the biharmonic viscosity by stability considerations, then the biharmonic viscous terms will be similarly active to harmonic viscous terms at the gridscale of the model, but much less active on larger scale motions. Similarly, a biharmonic diffusivity can be used for less diffusive flows.

In practice, biharmonic viscosity and diffusivity allow a less viscous, yet numerically stable, simulation than harmonic viscosity and diffusivity. MITgcm supports a plethora of biharmonic viscosities and diffusivities, which are controlled with parameters named similarly to the harmonic viscosities and diffusivities with the substitution $h \rightarrow 4$ (Adcroft et al., 2014).

TKE vertical mixing schemes

If the results from numerical models were insensitive to the constant values assigned to the mixing parameters, namely, the coefficients of vertical eddy viscosity ν and eddy diffusivity κ then there would be no need for concern. But this is not the case.

GGL90 scheme

This parameterization scheme is based on works on atmospheric turbulence modelling. It is designed to simulate vertical mixing at all depths, from the upper boundary layer down to the abyss. This scheme includes a single prognostic equation for the turbulent kinetic energy. The computation of the turbulent length scales is diagnostic, rather than prognostic. In weakly turbulent regions the simulated vertical diffusivity is inversely proportional to the Brunt-Vaisala frequency (Gaspar et al, 1990).

The turbulent vertical fluxes are parameterized using the classical concept of eddy diffusivity. The eddy diffusivities are related to the TKE according to

$$K_m = c_k l_k \bar{e}^{1/2} \quad (4.9)$$

$$K_s = K_h = K_m / P_{rt} \quad (4.10)$$

where C_k is a constant to be determined, l_k is a mixing length, e is the TKE and P_{rt} is the turbulent Prandtl number (Gaspar et al, 1990).

4.3.1 CONSTANT HORIZONTAL EDDY VISCOSITY- SENSITIVITY ANALYSIS

We first compare the results of numerical experiments that differ only in coefficients of horizontal viscosity. Later we show results of simulation that differ in values of the constants used in the vertical mixing scheme.

Various sensitivity simulations were carried out to determine how the model results are affected with different values of horizontal viscosity. A subset of these simulations is shown in Table 4.1

GGL90 scheme is applied for the vertical mixing; Constant in viscosity coefficient (C_k) is set equal to 0.1, dissipation constant (C_{eps}) equal to 0.7 and the minimum mixing length (L_{min}) is set equal to $1.e^{-2}$.

Table 4.1

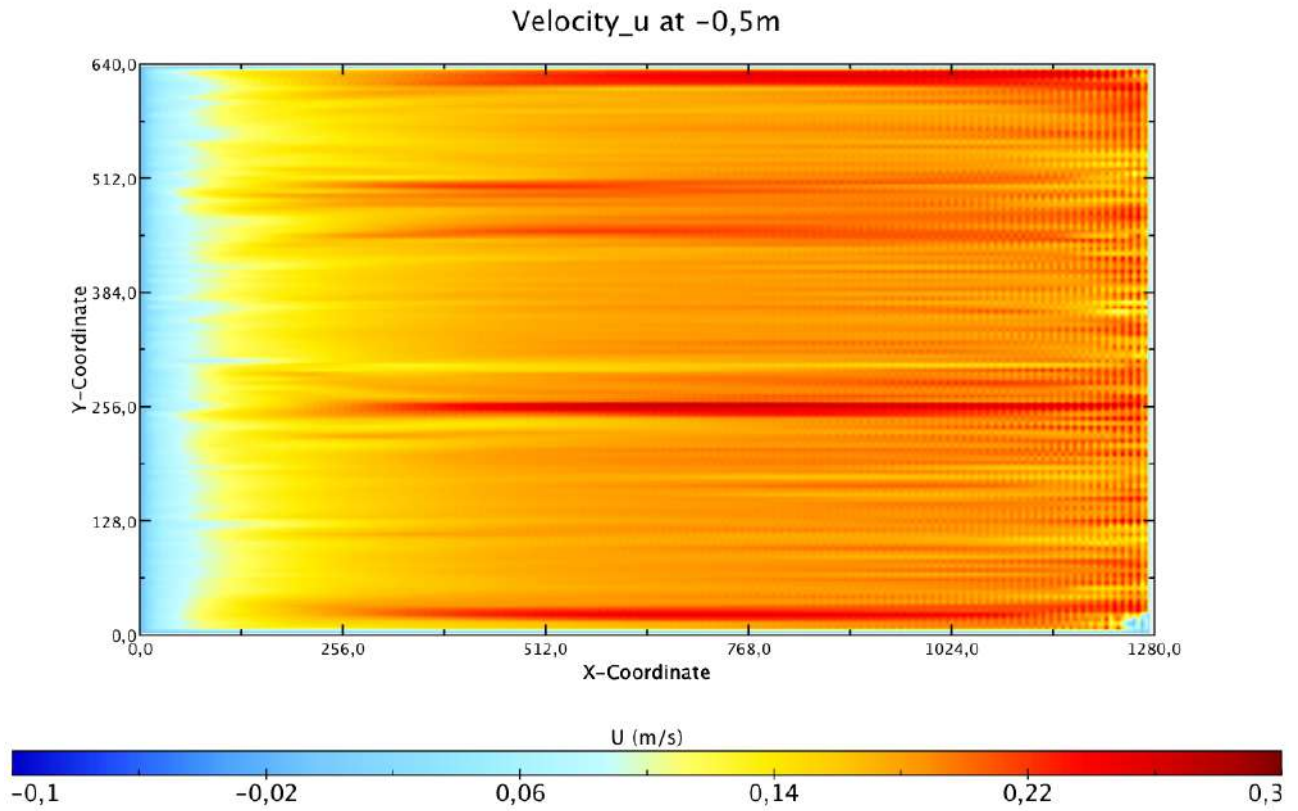
Sim.	Vertical Mixing	Setting	*ViscAh	*ViscAz
4	GGL90	Ck=0.1;Ceps=0.7;LengthMin=1.e ⁻²	1.e ⁻¹ m ² s ⁻¹	1.e ⁻⁷ m ² s ⁻¹
5	GGL90	Ck=0.1;Ceps=0.7;LengthMin=1.e ⁻²	1.e ⁻⁵ m ² s ⁻¹	1.e ⁻⁷ m ² s ⁻¹
6	GGL90	Ck=0.1;Ceps=0.7;LengthMin=1.e ⁻²	1.e ⁻⁴ m ² s ⁻¹	1.e ⁻⁷ m ² s ⁻¹
7	GGL90	Ck=0.1;Ceps=0.7;LengthMin=1.e ⁻²	1.e ⁻³ m ² s ⁻¹	1.e ⁻⁷ m ² s ⁻¹
8	GGL90	Ck=0.1;Ceps=0.7;LengthMin=1.e ⁻²	1.e ⁻² m ² s ⁻¹	1.e ⁻⁷ m ² s ⁻¹

*ViscAh and ViscAz are background horizontal and vertical eddy viscosities, respectively.

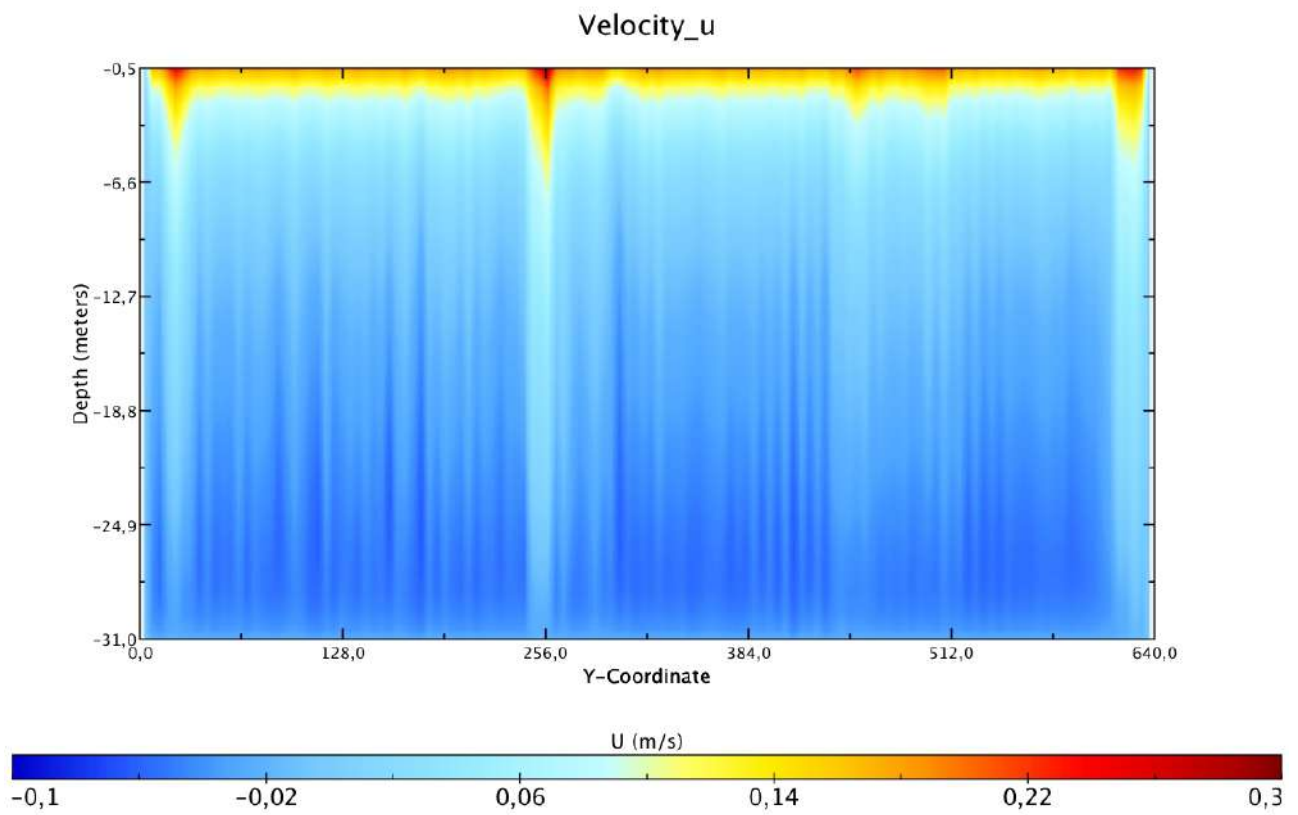
Figures from 4.9 to 4.13 (A)-(B) show the contour plot of U component of horizontal velocity at horizontal plane (-0,5m) and at vertical plane. The figures show that, as expected, at the surface the current is aligned to wind direction, but close to the bottom the velocity field is reversed with respect to the wind direction. This inversion of current between the surface and bottom is well shown in every simulation.

The MIT model reveals a considerable sensitivity in response to the different values of horizontal viscosity. Indeed, it is possible to recognise a tendency to a homogenization of the velocity field resulting from the increasing of the horizontal viscosity. Anyway, it is, however, possible to observe higher values at the surface with respect to the results obtained by LES simulation. This can be explicable analysing the values of the constants used in the vertical mixing scheme. This scheme, indeed, has been developed for open-ocean and the calibration, obtained and proposed, is suitable for that scenario.

Therefore, it has been necessary to tune up the vertical scheme following the results of LES-Coast simulation.

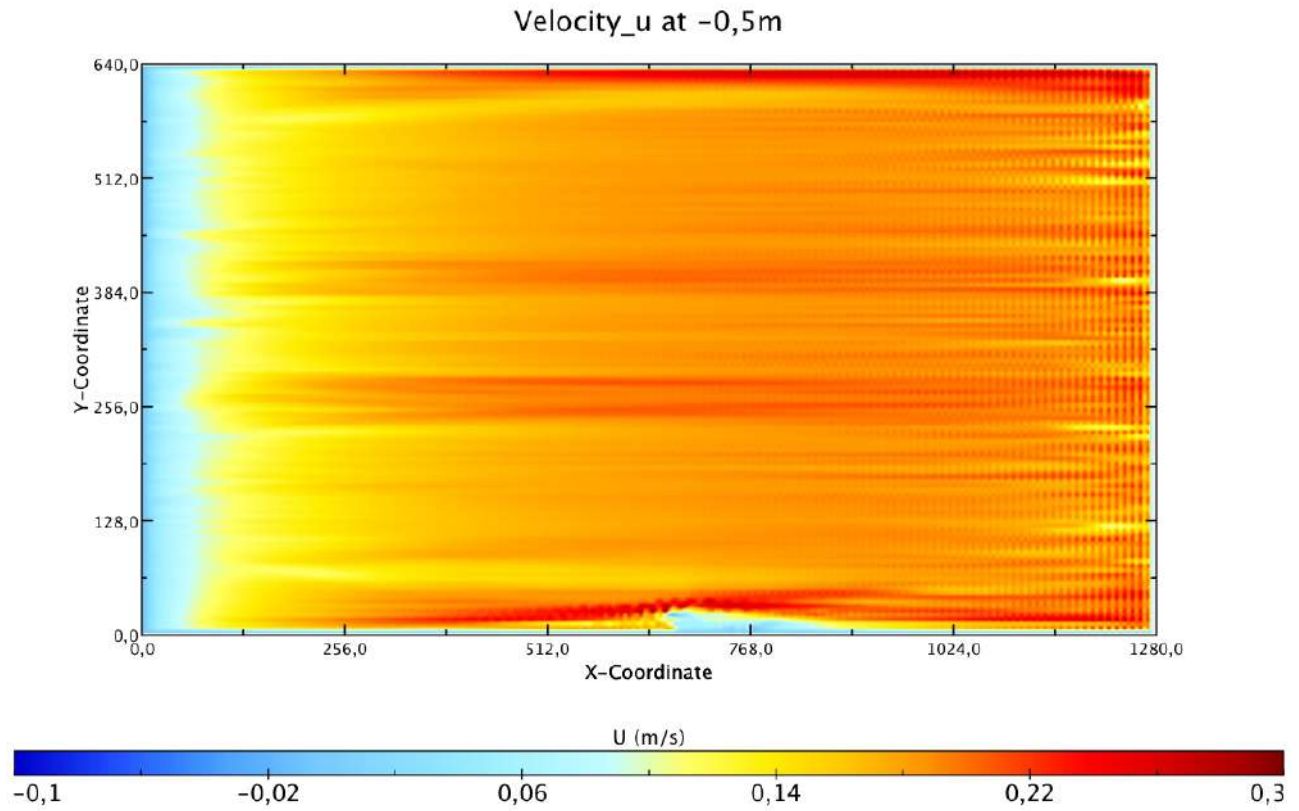


A)

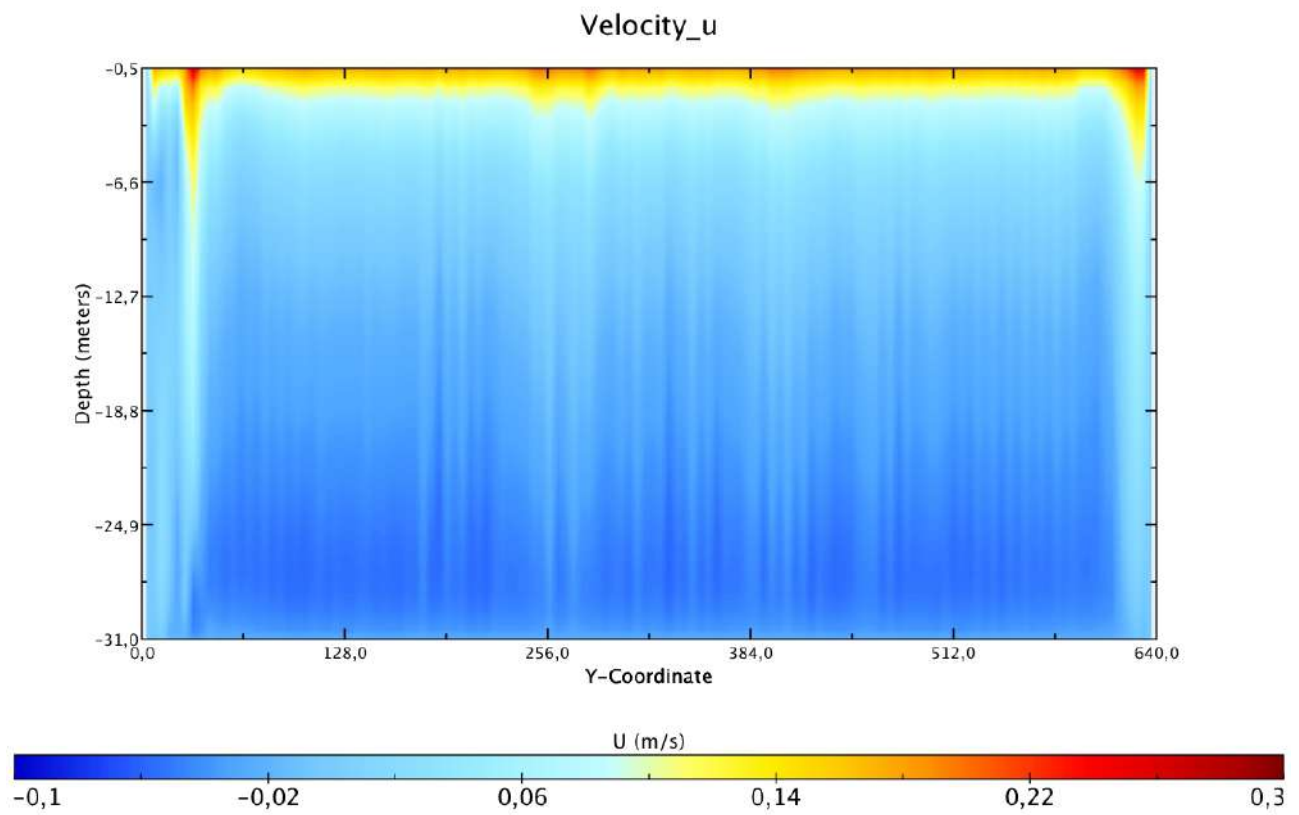


B)

Fig.4.9: Simulation 5 (Horizontal viscosity- $A_h=1.E-5$); Contour plot of U component of the horizontal instantaneous velocity (A) horizontal plane (B) vertical plane. The dimension of the domain (meters) are shown on x and y axes.

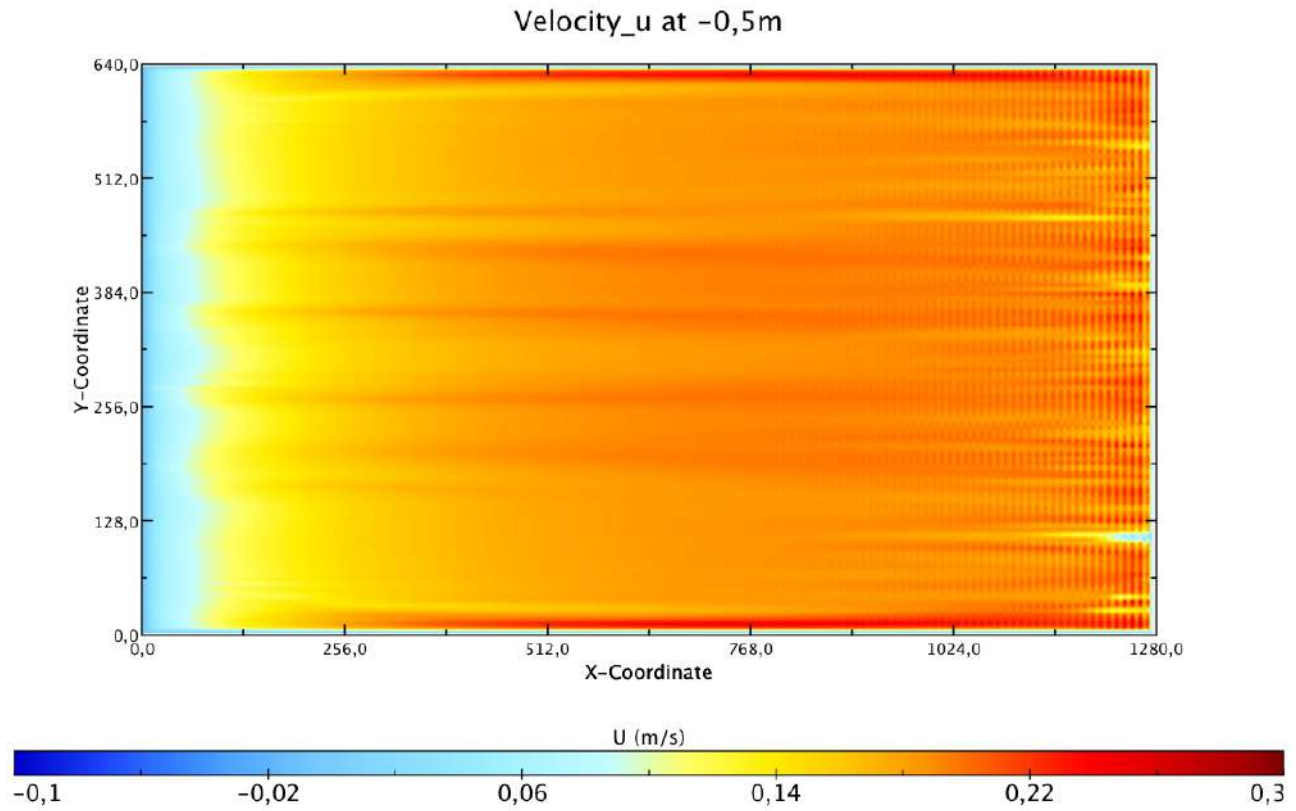


A)

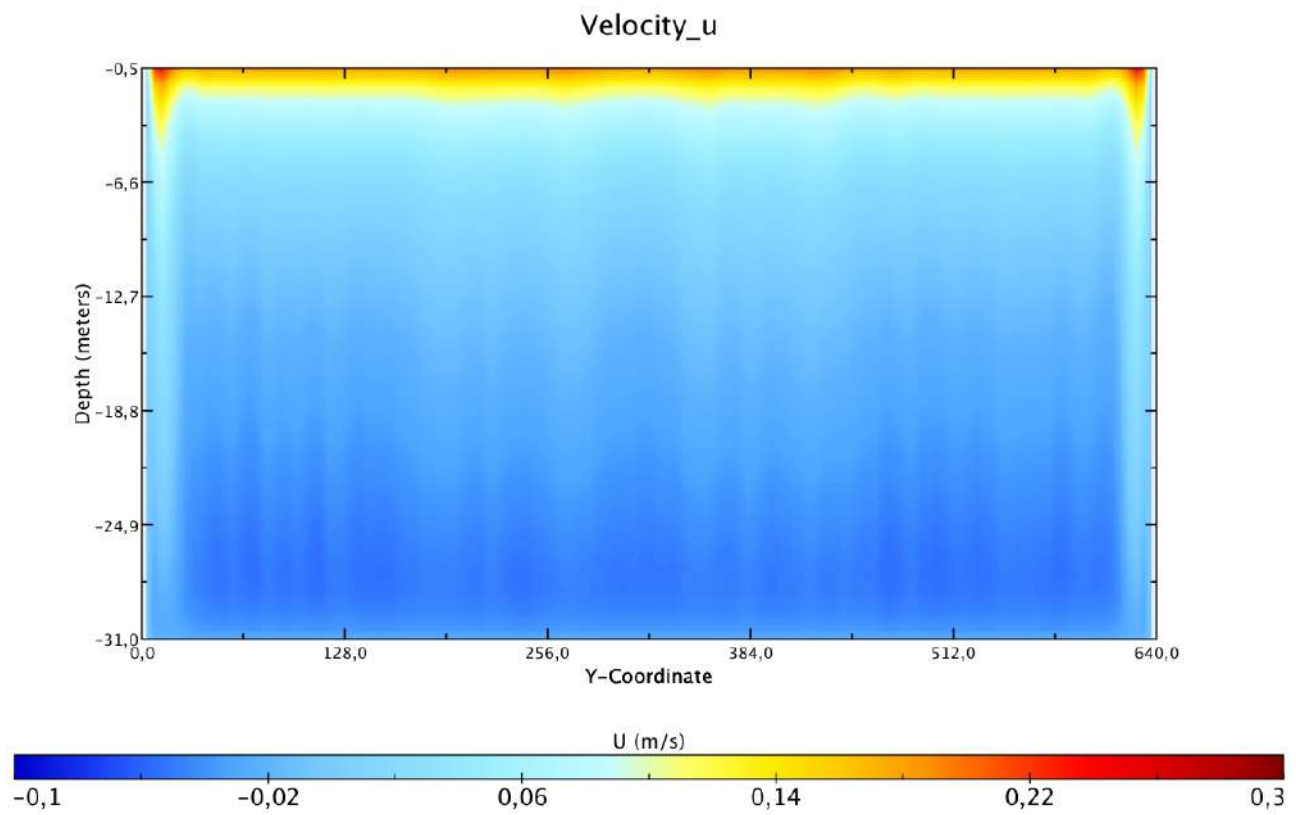


B)

Fig.4.10: Simulation 6 (Horizontal viscosity- $Ah=1.E-4$); Contour plot of U component of the horizontal instantaneous velocity (A) horizontal plane (B) vertical plane. The dimension of the domain (meters) are shown on x and y axes.

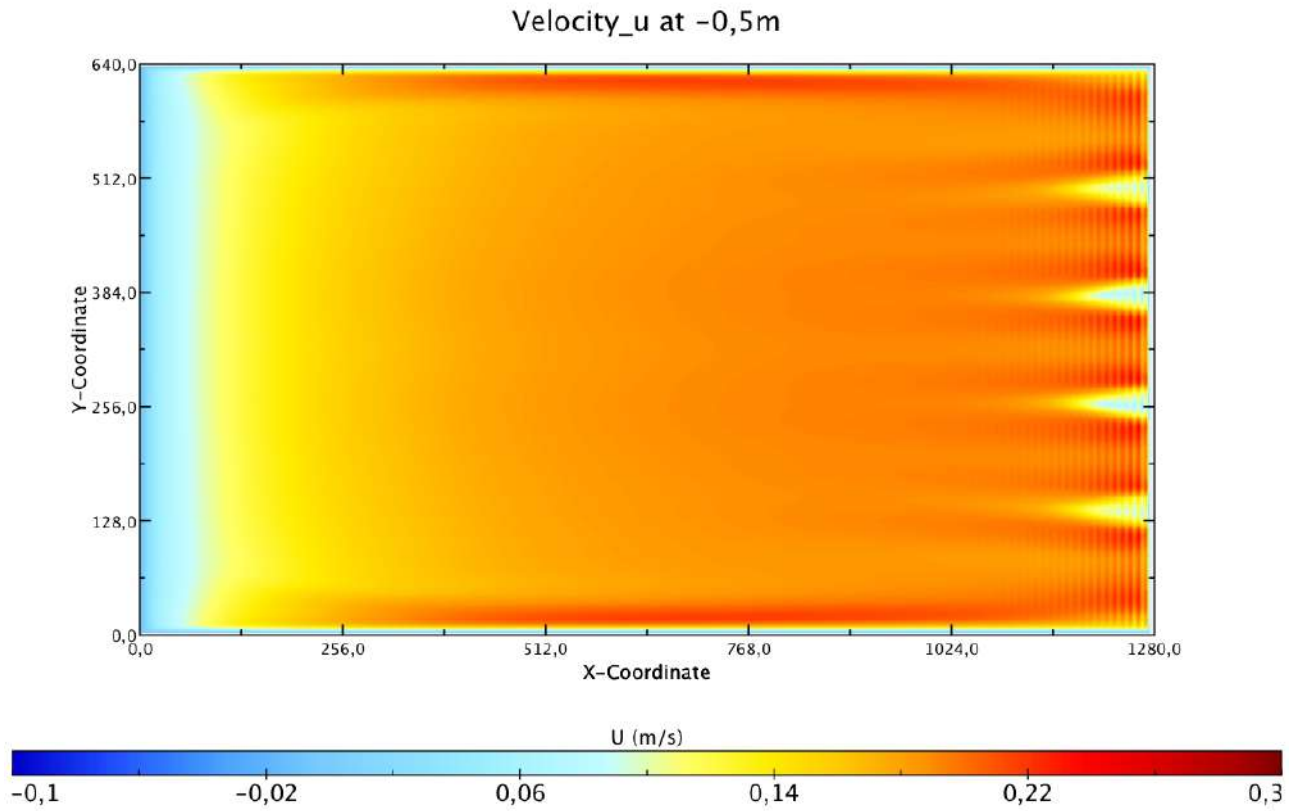


A)

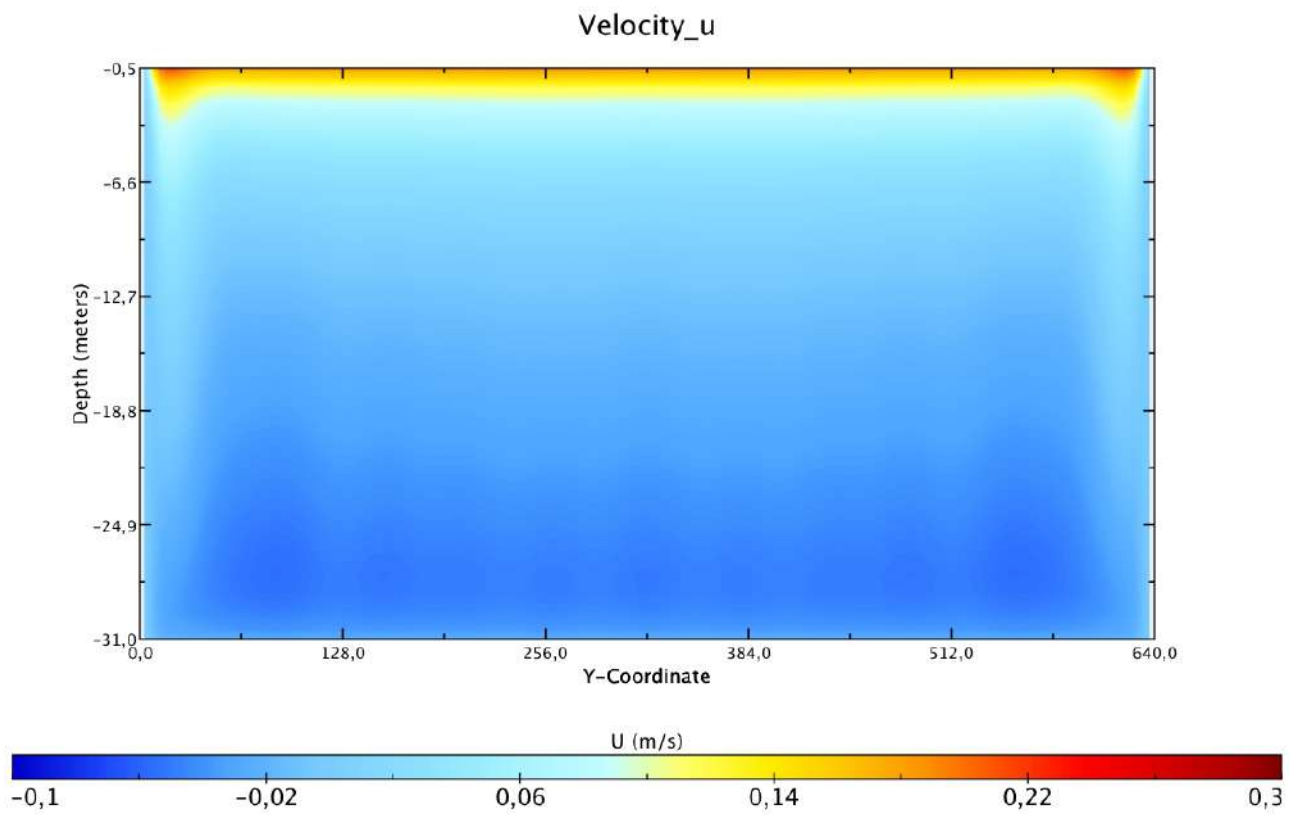


B)

Fig.4.11: Simulation 7 (Horizontal viscosity- $A_h=1.E-3$); Contour plot of U component of the horizontal instantaneous velocity (A) horizontal plane (B) vertical plane. The dimension of the domain (meters) are shown on x and y axes.

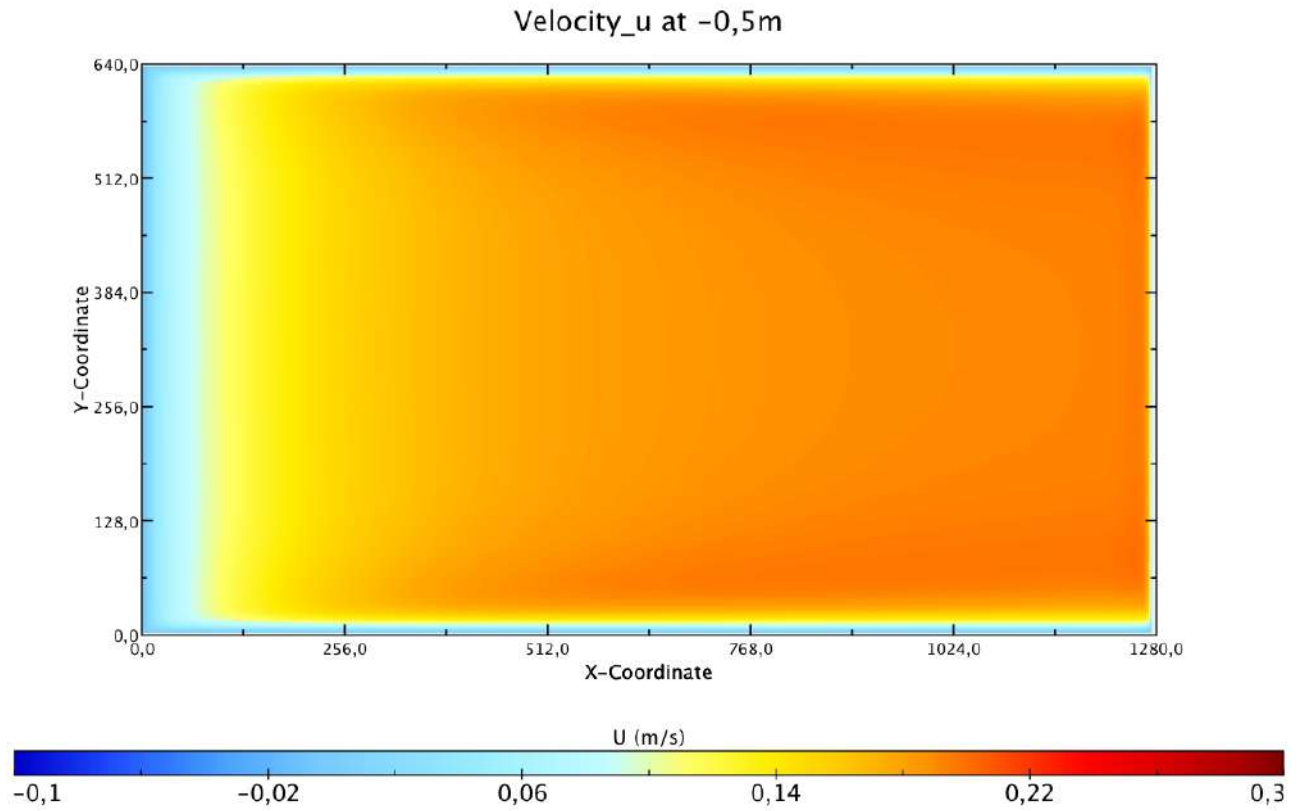


A)

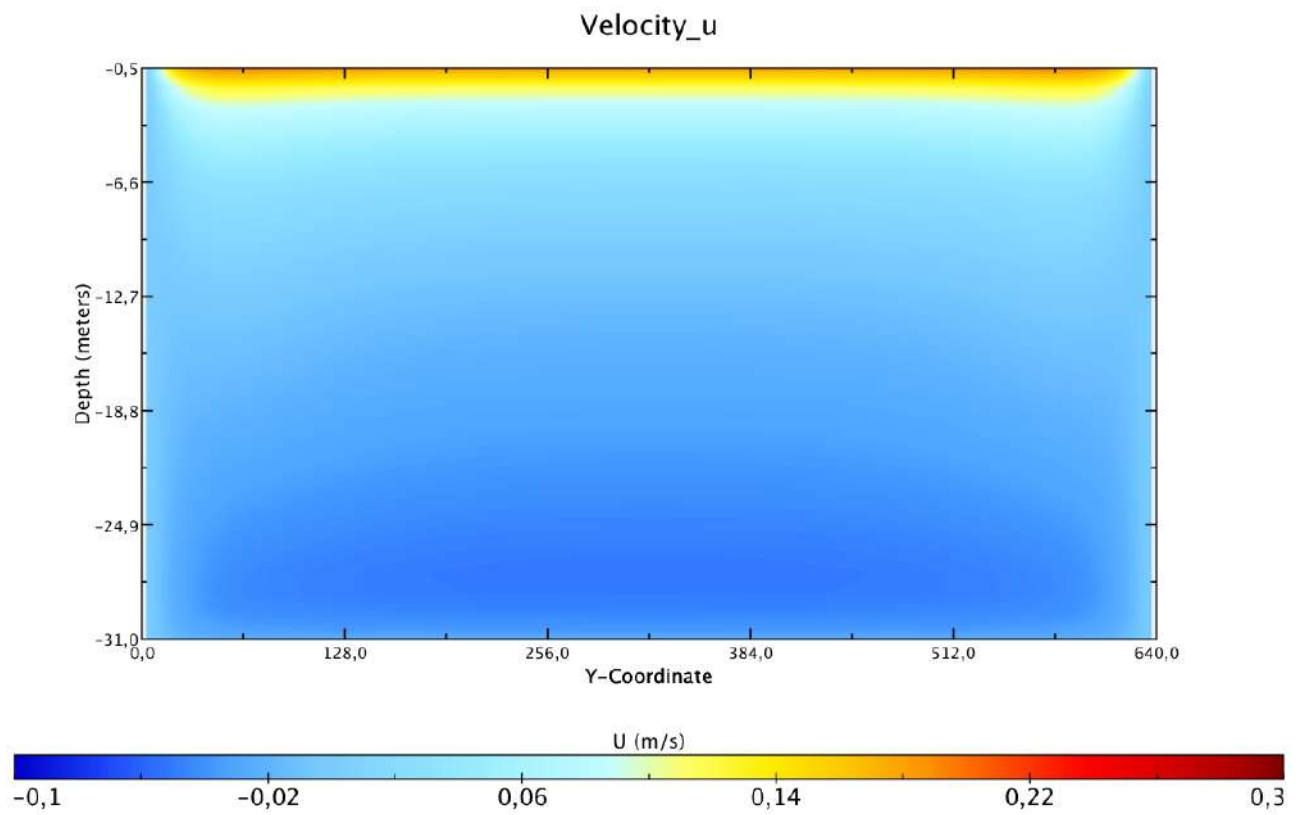


B)

Fig.4.12: Simulation 8 (Horizontal viscosity- $Ah=1.E-2$); Contour plot of U component of the horizontal instantaneous velocity (A) horizontal plane (B) vertical plane. The dimension of the domain (meters) are shown on x and y axes.



A)



B)

Fig.4.13: Simulation 4 (Horizontal viscosity- $Ah=1.E-1$); Contour plot of U component of the horizontal instantaneous velocity (A) horizontal plane (B) vertical plane. The dimension of the domain (meters) are shown on x and y axes.

The analysis of the subset of simulations, discussed above, has been carried out. The entire domain has been divided into three characteristic depths (-0,5m, -5,5m and -29,5m). For each layer the velocity profiles have been compared and the correlation coefficients (R) have been calculated (Figures 4.14 to 4.16). From the results of this study we have selected the simulation number 7 (MIT_7) in order to proceed with the tuning of the vertical mixing scheme and later with the nesting.

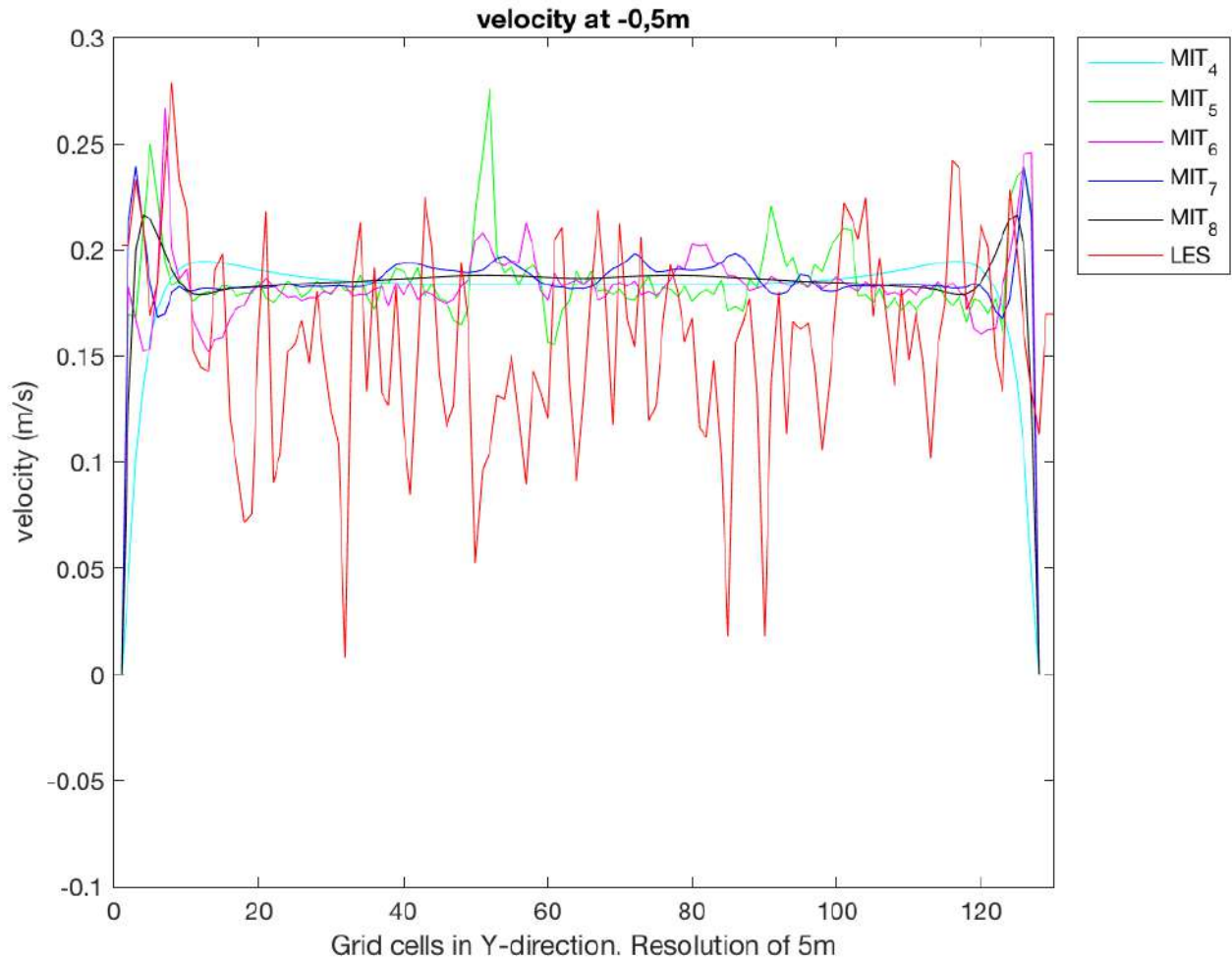


Fig.4.14: Velocity profiles at -0,5m. The plot is shown for X-Coordinate of 640m. On the x-axis is shown the number of grid cells in y-direction, with a resolution of 5m (Y-Coordinate: 0-640m).

Correlation Coefficient:

- LES – MIT_4 R=-0,075
- LES – MIT_5 R=-0,046
- LES – MIT_6 R=-0,023
- LES – MIT_7 R=0,028
- LES – MIT_8 R=-0,004

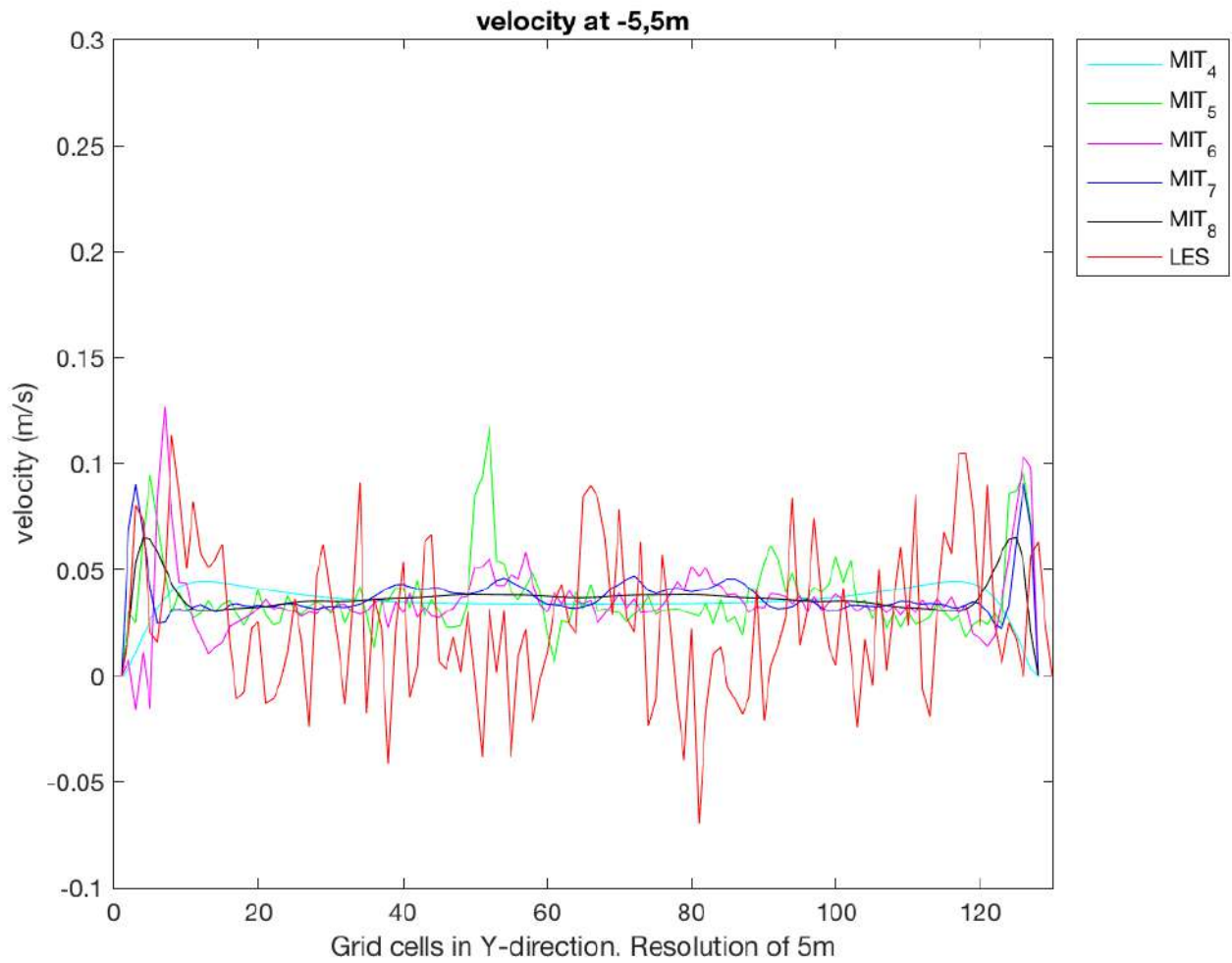


Fig.4.15: Velocity profiles at -5,5m. The plot is shown for X-Coordinate of 640m. On the x-axis is shown the number of grid cells in y-direction, with a resolution of 5m (Y-Coordinate: 0-640m).

Correlation Coefficient:

LES – MIT_4 R=0,030
 LES – MIT_5 R=-0,096
 LES – MIT_6 R=-0,110
 LES – MIT_7 R=-0,032
 LES – MIT_8 R=-0,052

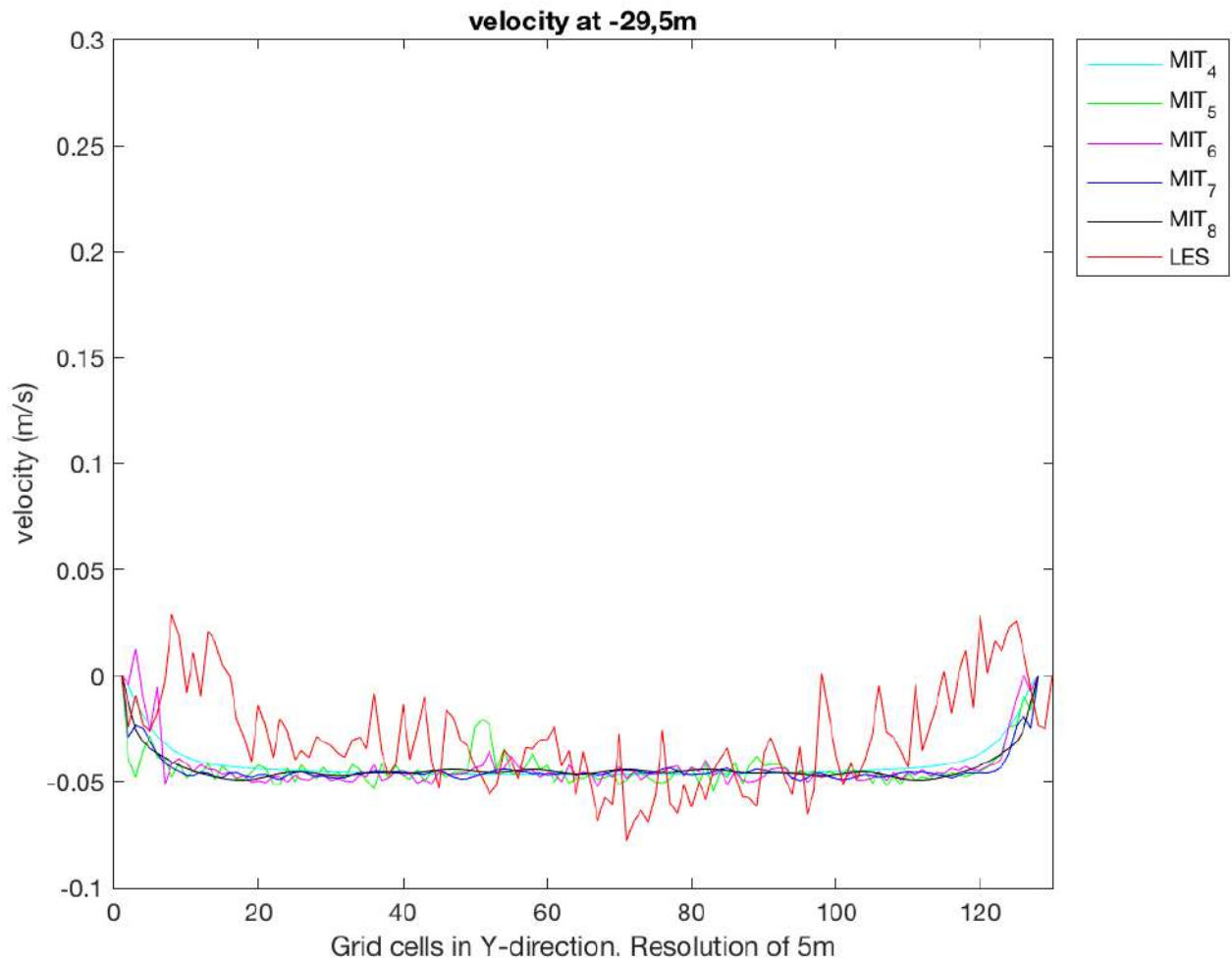


Fig.4.16: Velocity profiles at -29,5m. The plot is shown for X-Coordinate of 640m. On the x-axis is shown the number of grid cells in y-direction, with a resolution of 5m (Y-Coordinate: 0-640m).

Correlation Coefficient:

- LES – MIT_4 R=0,30
- LES – MIT_5 R=0,220
- LES – MIT_6 R=0,220
- LES – MIT_7 R=0,265
- LES – MIT_8 R=0,253

Starting from the configuration selected and following the results obtained by the LES-Coast simulation, the vertical mixing scheme has been tuned up.

In this section we discuss the results of the simulation performed by the MITgcm model tuned with the final constants selected. Parameters are shown in the following table 4.2

Table 4.2

Sim	Vertical Mixing	Setting	*ViscAh	*ViscAz
29	GGL90	Ck=0.15;Ceps=1.0;LengthMin=3.e ⁻²	1.e ⁻³ m ² s ⁻¹	1.e ⁻⁷ m ² s ⁻¹

*ViscAh and ViscAz are background horizontal and vertical eddy viscosities, respectively.

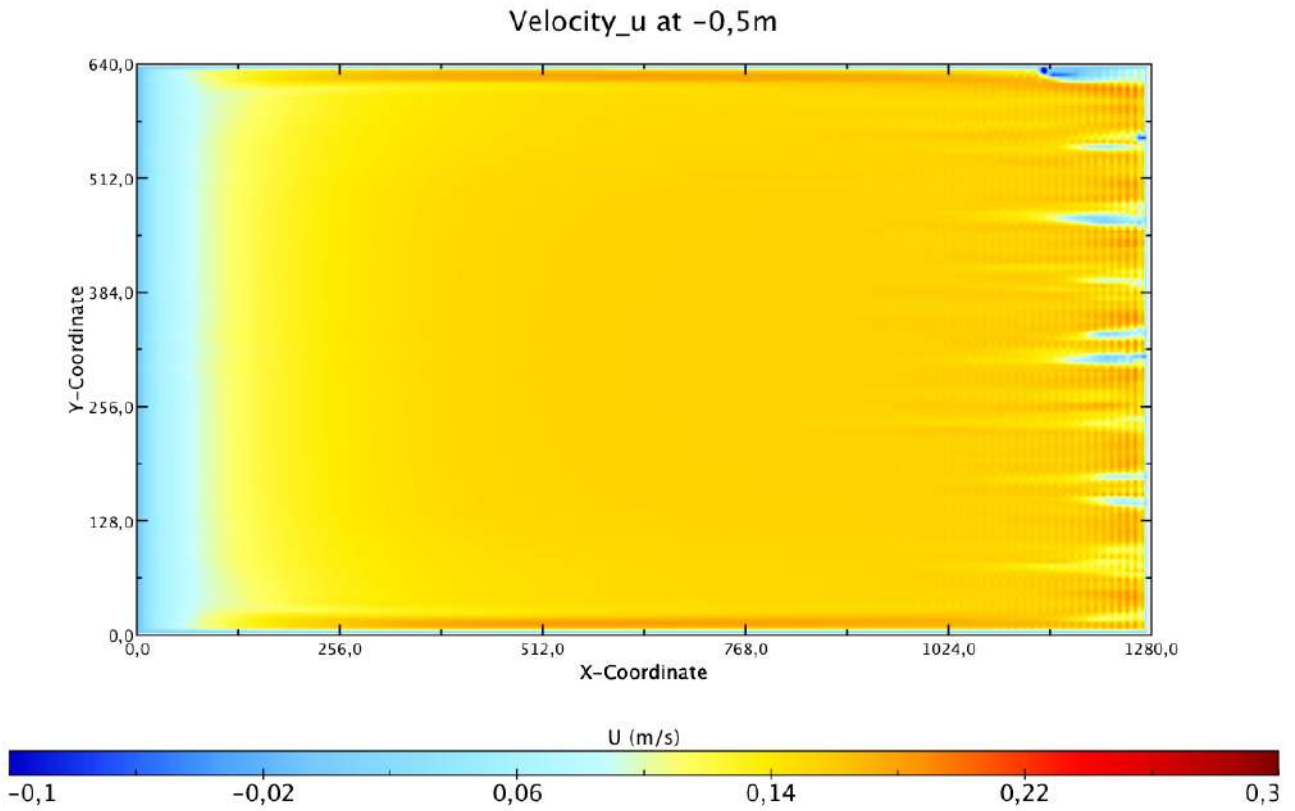
First, we describe the instantaneous flow field; successively we discuss about turbulent kinetic energy and the eddy viscosities.

Instantaneous field

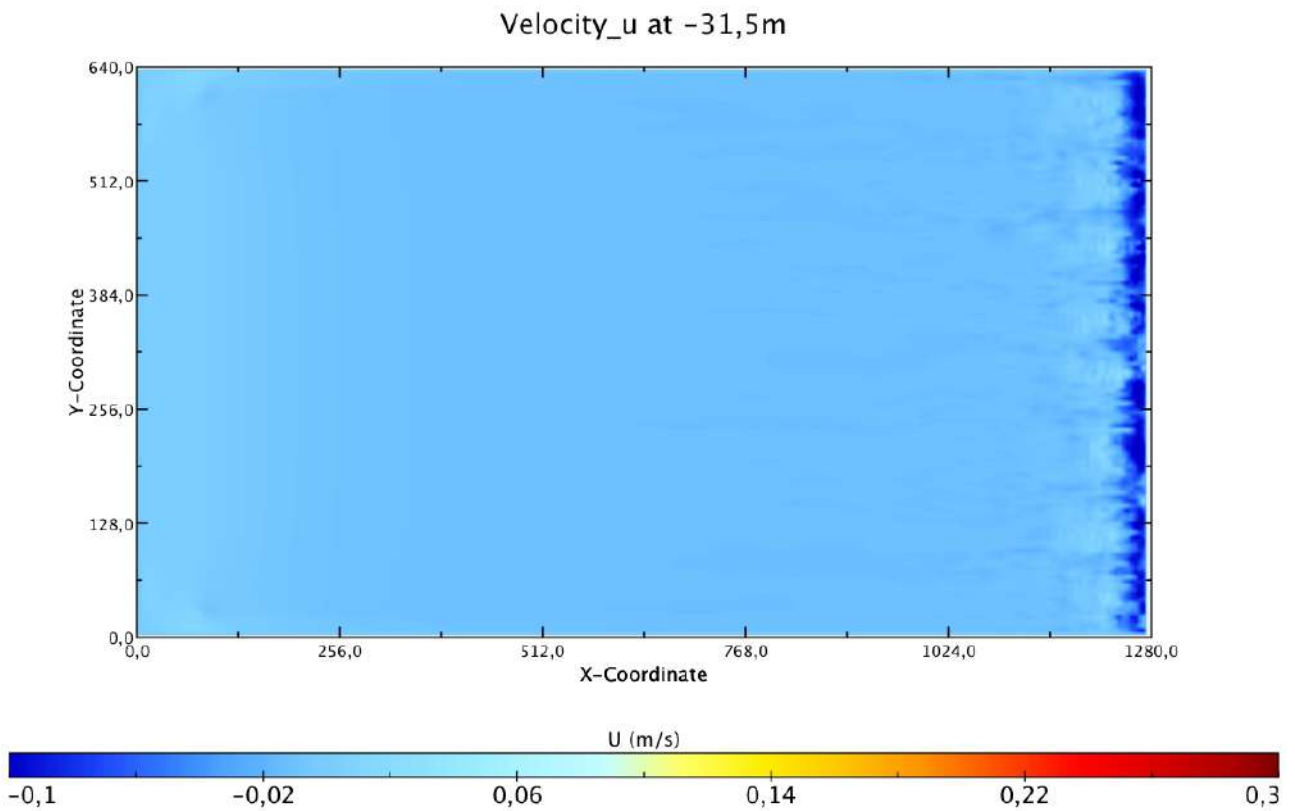
Figures 4.17 (A and B) and 4.18 (A and B) show the contour plot of U and V component of the horizontal velocity at two different depths. As expected, the “classical” feature, that is the inversion of current between the surface and bottom, is still shown.

It is possible to recognise lower values at the surface with respect to the results obtained by the previous MIT simulation. This time the simulation returns a velocity field with intensity more similar to that developed by a LES simulation. This is because the GGL90 vertical scheme has been tuned and it has been calibrated for a shallow water scenario.

Figure 4.20 provides the contour plot of the vertical velocity. It is possible to observe an intense vertical mixing close to the eastern side of the domain and an emphasized positive velocity on the western side.

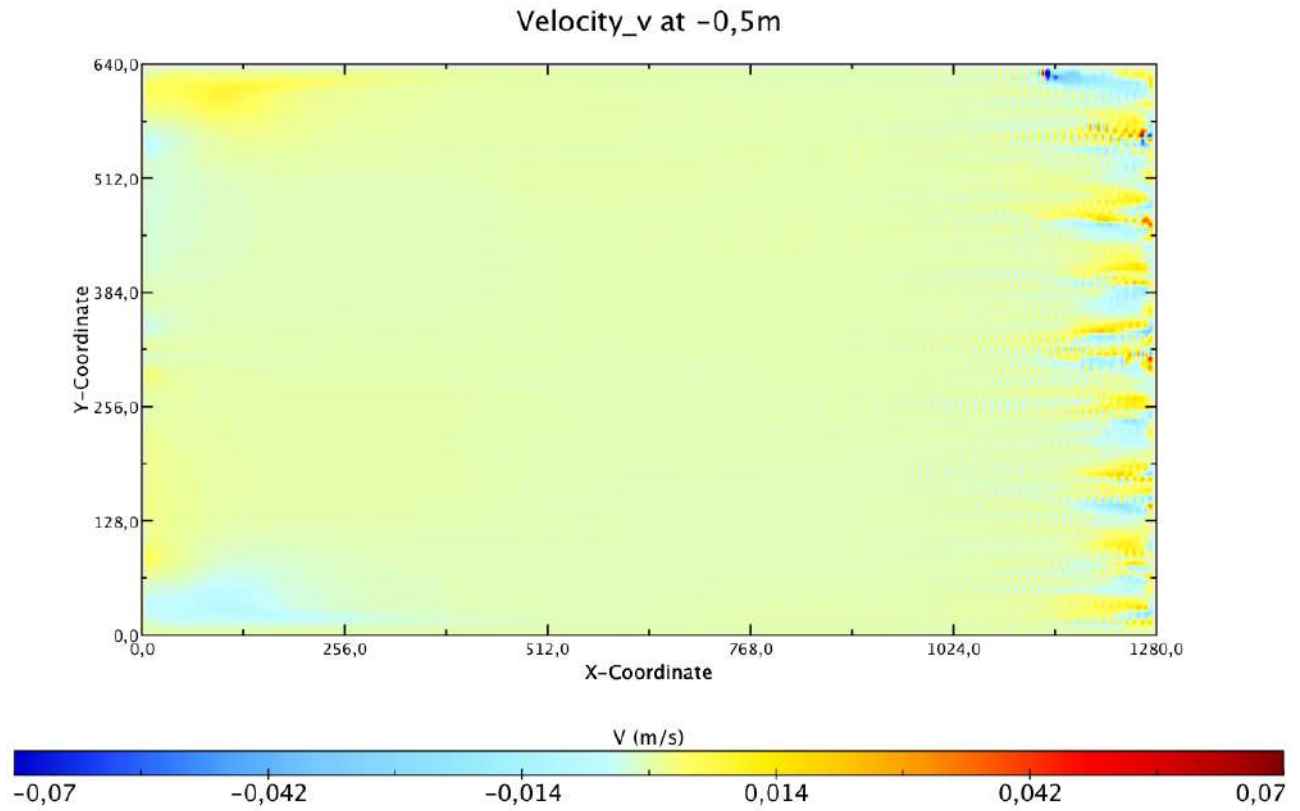


A)

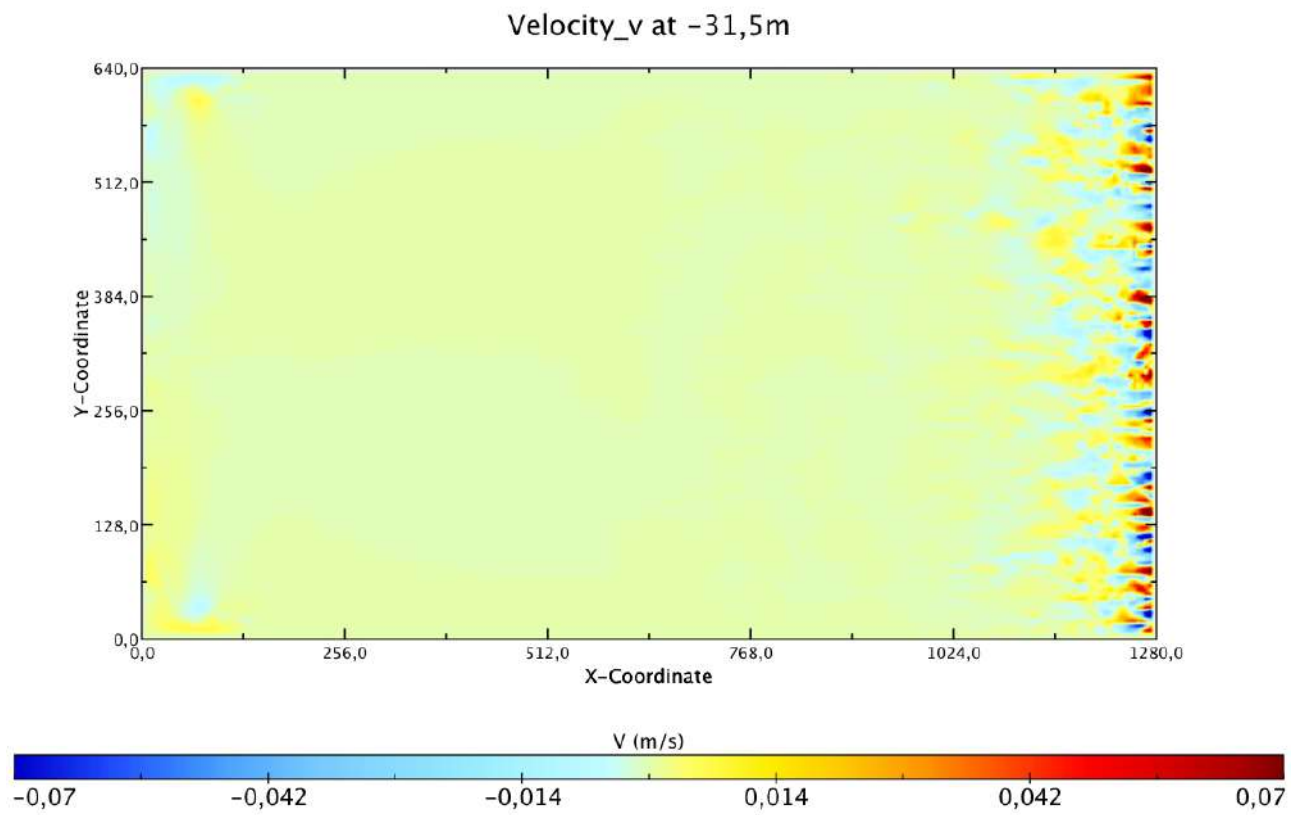


B)

Fig.4.17: Contour plot of U component of the horizontal instantaneous velocity at two horizontal planes: (A) -0,5m; (B) -31,5m. The dimension of the domain (meters) are shown on x and y axes.



A)



B)

Fig.4.18: Contour plot of V component of the horizontal instantaneous velocity at two horizontal planes: (A) -0,5m; (B) -31,5m. The dimension of the domain (meters) are shown on x and y axes.

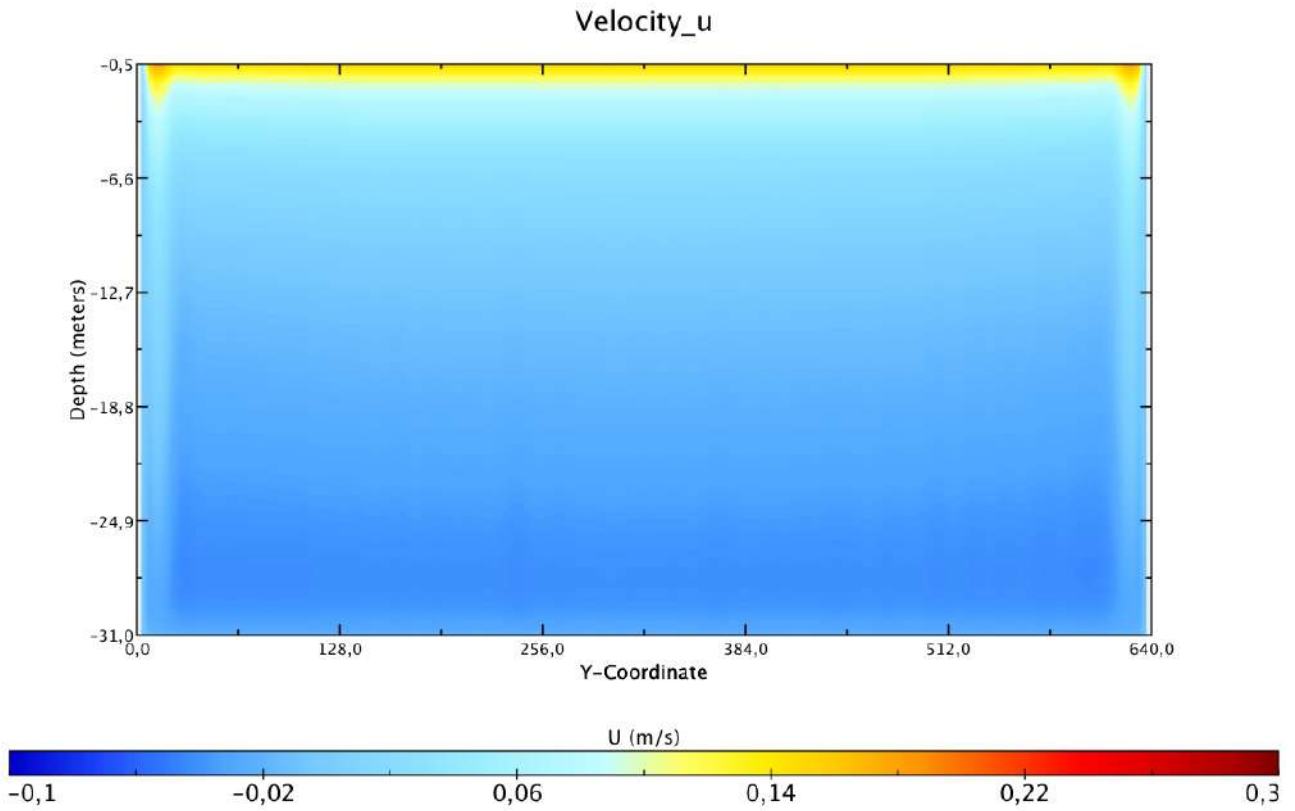


Fig.4.19: Contour plot of U component of the horizontal instantaneous velocity in a vertical plane (x-coord=640m).

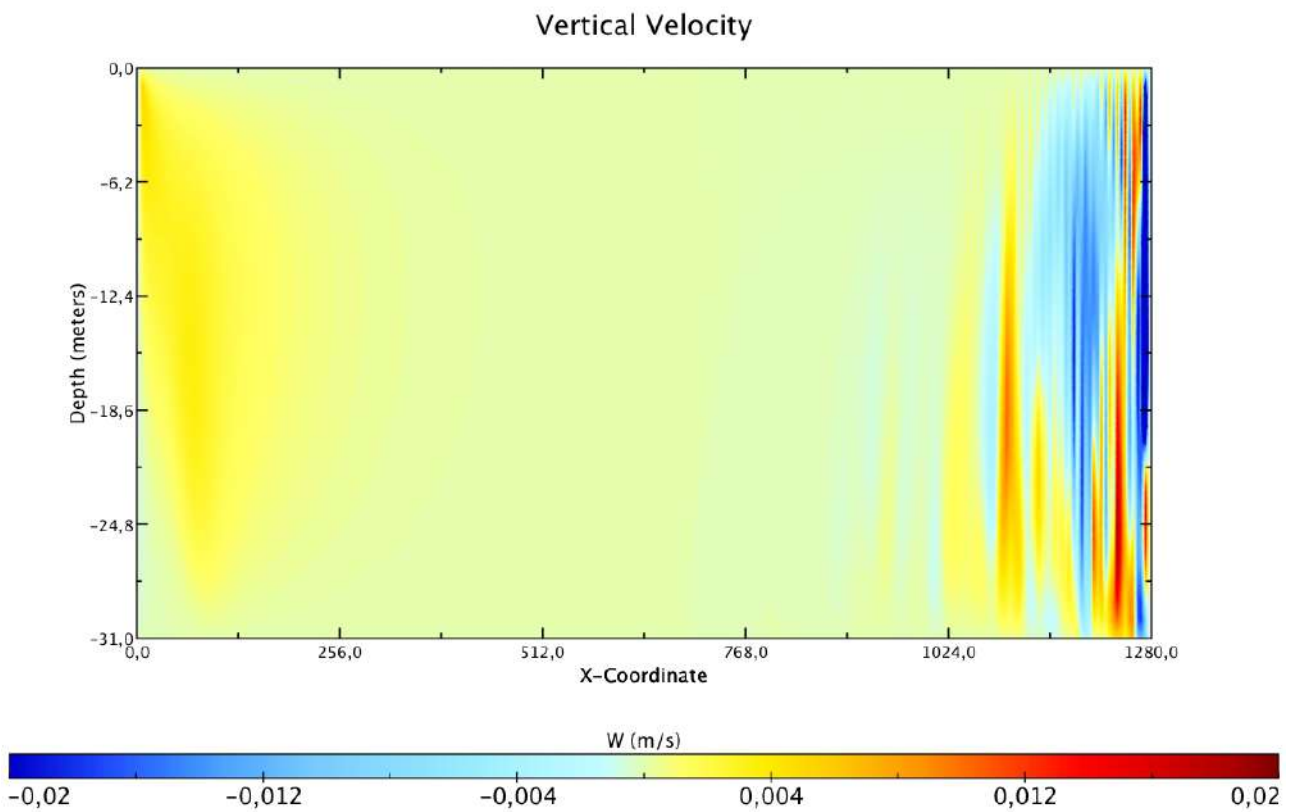


Fig.4.20: Contour plot of W component of the vertical instantaneous velocity in a vertical plane (y-coord=320m).

Turbulent Kinetic Energy

With the following definition for Turbulent Kinetic Energy (TKE):

$$\bar{e} = 0.5 \left(\overline{u'^2} + \overline{v'^2} + \overline{w'^2} \right) \quad (4.11)$$

a prognostic equation is developed:

$$\frac{\partial \bar{e}}{\partial t} = -\frac{\partial}{\partial z} \left(\overline{ew'} + \frac{\overline{p'w'}}{\rho_0} \right) - \overline{u'_h w'} \cdot \frac{\partial U_h}{\partial z} + \overline{b'w'} - \epsilon \quad (4.12)$$

where $B = g\rho_0^{-1} \rho$ is the buoyancy and ϵ is the dissipation.

The vertical turbulent fluxes are parameterized with the usual mixing coefficients K_m and K_ρ according to

$$-\overline{u'_h w'} = K_m \frac{\partial U_h}{\partial z} \quad (4.13)$$

$$-\overline{b'w'} = -g\rho_0^{-1} K_\rho \frac{\partial \rho}{\partial z} = K_\rho N^2 \quad (4.14)$$

$$K_\rho = K_m / P_{rt} \quad (4.15)$$

where N designates the Brunt-Vaisala frequency.

TKE is diagnosed at the surface and at the bottom. The bottom value for TKE is fixed to a numerical minimal threshold, while the surface value includes a dependence on the wind stress:

$$\bar{e}_{surface} = \max(3.75u^{*2}, \bar{e}_0) \quad (4.16)$$

with

$$u^{*2} = \tau / \rho_0 \quad (4.17)$$

and

$$\bar{e}_0 = 10^{-11} m^2 s^{-2} \quad (4.18)$$

The distribution of turbulent kinetic energy is illustrated for horizontal and vertical plane (fig. 4.21 and 4.22). It is possible to see how the MIT simulation develops less TKE (maximum value of 0,001) then LES simulation (maximum value of 0,0025). The minimum and maximum values of the colour bar have been chosen in order to make the patterns clearer.

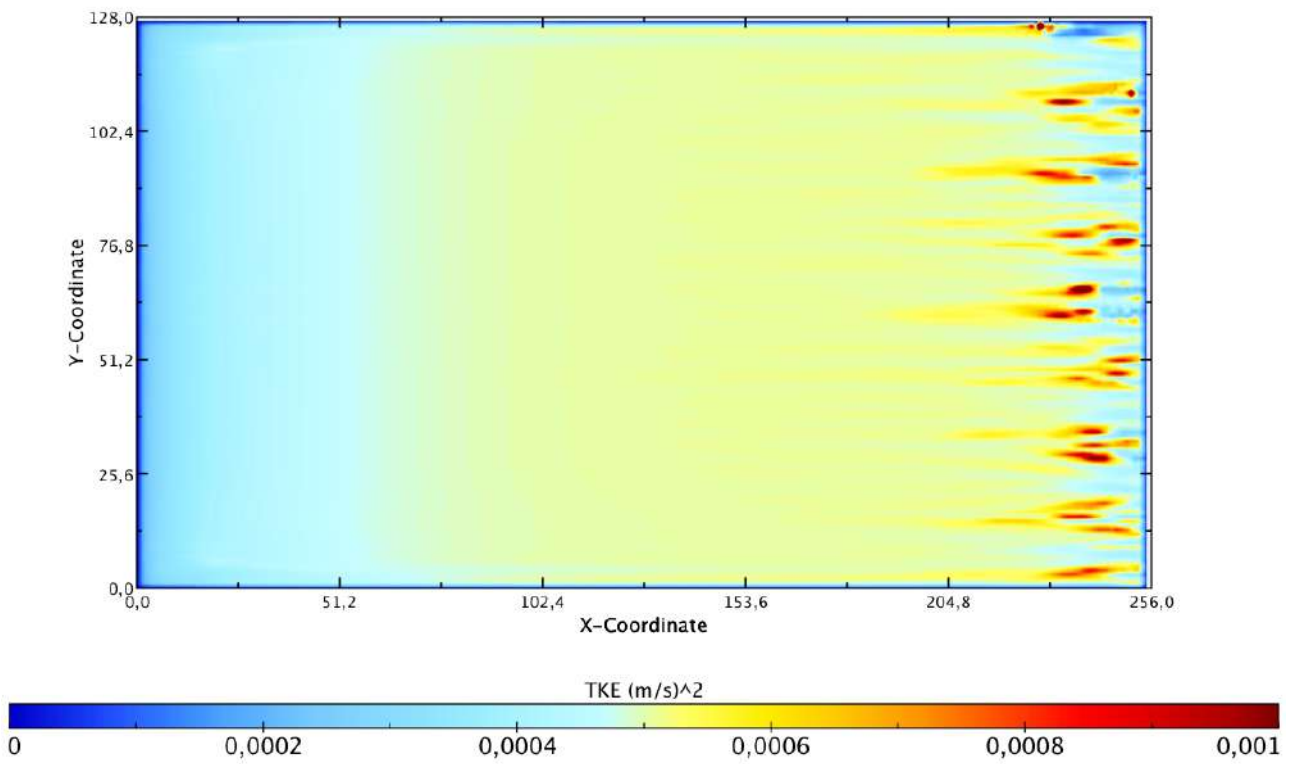


Fig.4.21: Turbulent kinetic energy at the surface. Grid cells are shown on x and y axes; Resolution 5 m.

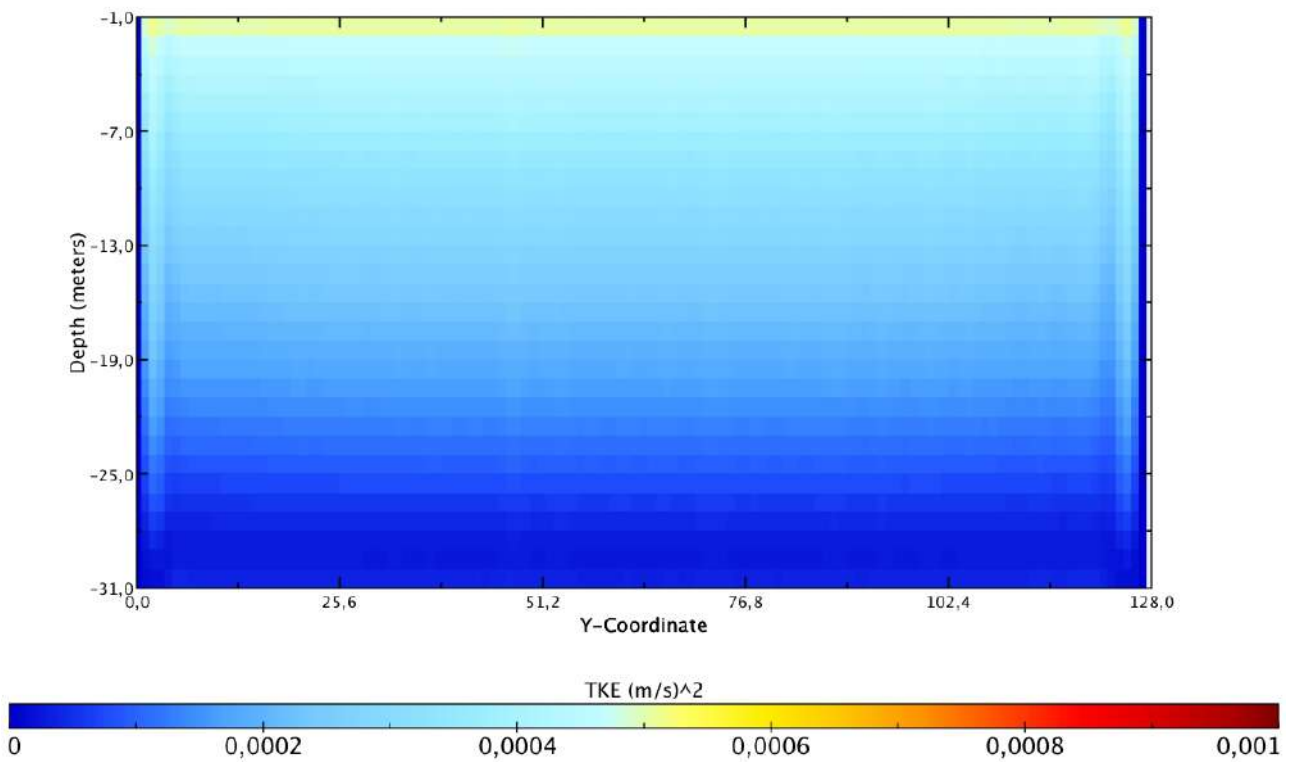


Fig.4.22: Vertical distribution of turbulent kinetic energy in a vertical plane. Grid cells are shown on y-coord; Resolution 5 m (x=128).

Eddy Viscosities

The horizontal eddy viscosity has been set constant and equal to $1 \cdot 10^{-3} \text{ m}^2\text{s}^{-1}$

Figure 4.23 illustrates the distribution of the not homogeneous vertical eddy viscosity. Comparing the distributions of both vertical eddy viscosity (that calculated from LES (Fig 4.8) and this one), it is possible to assert that the distribution is similar, showing also the same intensification on the eastern side of the domain, due to the presence of a strong downwelling region.

Overall, this parameterization produces a vertical eddy viscosity with lower values.

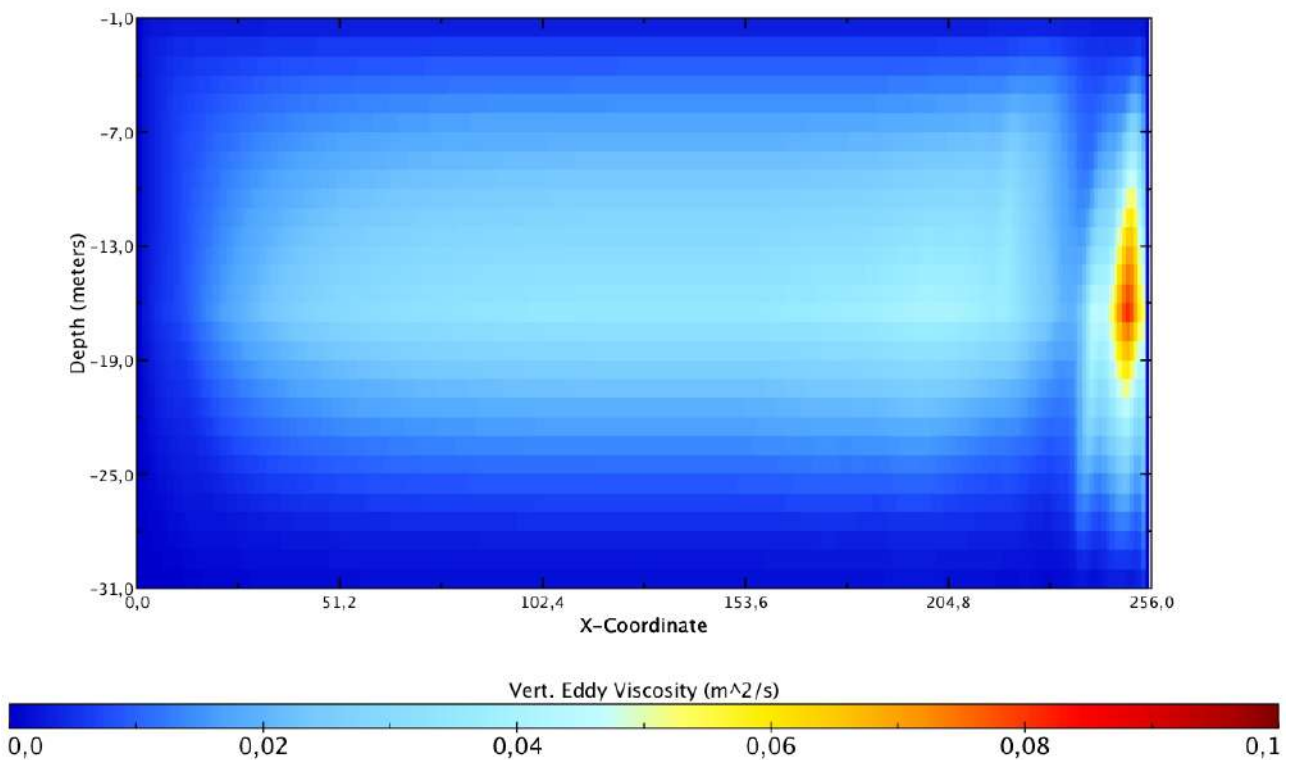


Fig.4.23: Vertical distribution of vertical eddy viscosity. Vertical plane, grid cells are shown on x-coord; Resolution 5 m.

4.3.2 LEITH VISCOSITY – SENSITIVITY ANALYSIS

Now we compare the results of numerical experiments performed by using Leith Viscosity for the horizontal mixing parameterization. We show results of simulations that differ in values of the coefficients used in this horizontal mixing scheme.

Various sensitivity runs have been carried out. A subset of these simulations is shown in Table 4.3.

GGL90 scheme is applied for the vertical mixing; Constant in viscosity coefficient (Ck) is set equal to 0.1, dissipation constant (Ceps) equal to 0.7 and the minimum mixing length (LenghtMin) is set equal to $1.e^{-2}$.

Table 4.3

Sim	Horizontal Mixing	*Setting	**ViscAz
37	LEITH	viscC2=0; viscC4=0.25; viscC2D=0; viscC4D=0.25	$1.e^{-7} \text{ m}^2\text{s}^{-1}$
33	LEITH	viscC2=0; viscC4=0.5; viscC2D=0; viscC4D=0.5	$1.e^{-7} \text{ m}^2\text{s}^{-1}$
1	LEITH	viscC2=0; viscC4=1; viscC2D=0; viscC4D=1	$1.e^{-7} \text{ m}^2\text{s}^{-1}$
32	LEITH	viscC2=0; viscC4=2; viscC2D=0; viscC4D=2	$1.e^{-7} \text{ m}^2\text{s}^{-1}$
2	LEITH	viscC2=0; viscC4=3; viscC2D=0; viscC4D=3	$1.e^{-7} \text{ m}^2\text{s}^{-1}$

*viscC2 is the harmonic coefficient and viscC4 is the biharmonic coefficient.

**ViscAz is background vertical eddy viscosity.

Figures from 4.24 to 4.28 show the contour plot of U component of horizontal velocity at the surface.

Also in this case, the MIT model reveals a considerable sensitivity in response to the different coefficients. It is yet possible to observe higher values at the surface with respect to the results obtained by LES simulation and a tendency to a homogenization of the velocity field resulting from the increasing of the biharmonic coefficient.

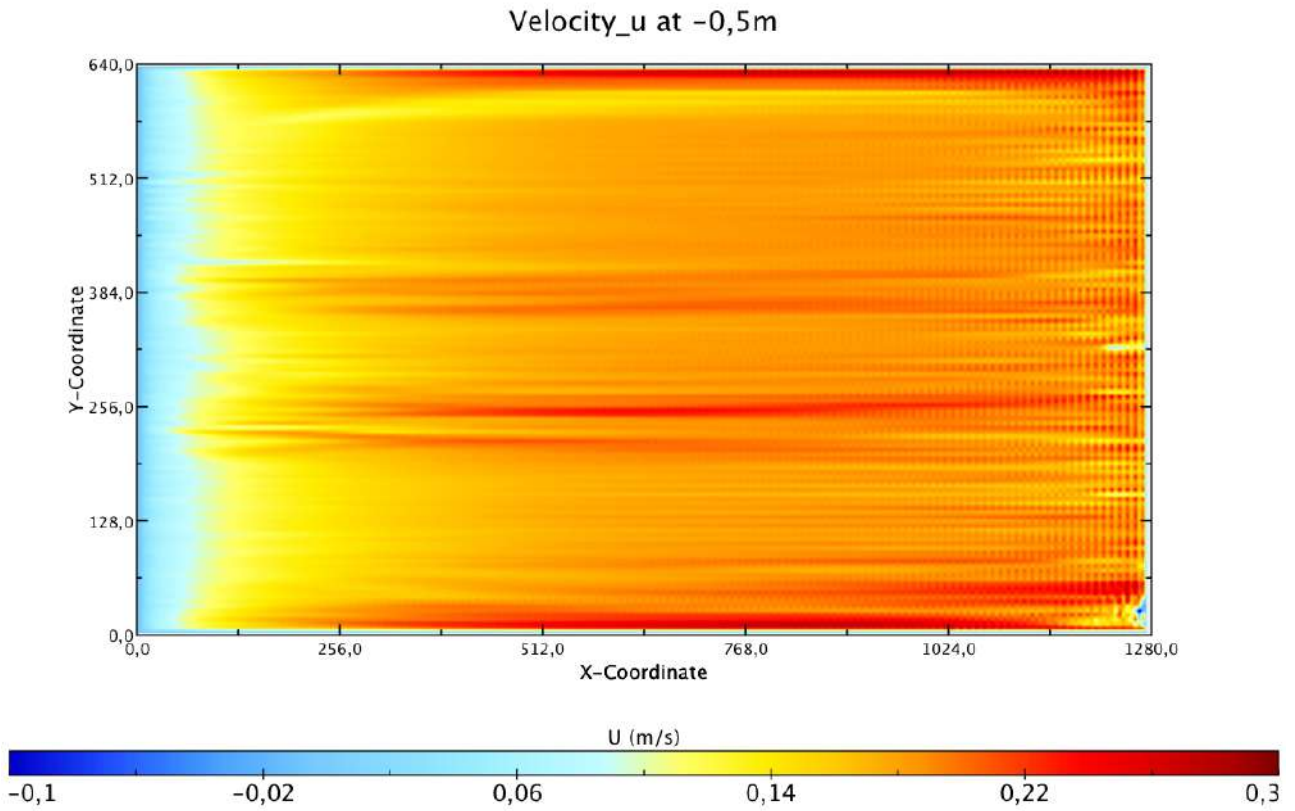


Fig. 4.24: Simulation 37 (viscC2=0; viscC4=0.25; viscC2D=0; viscC4D=0.25)

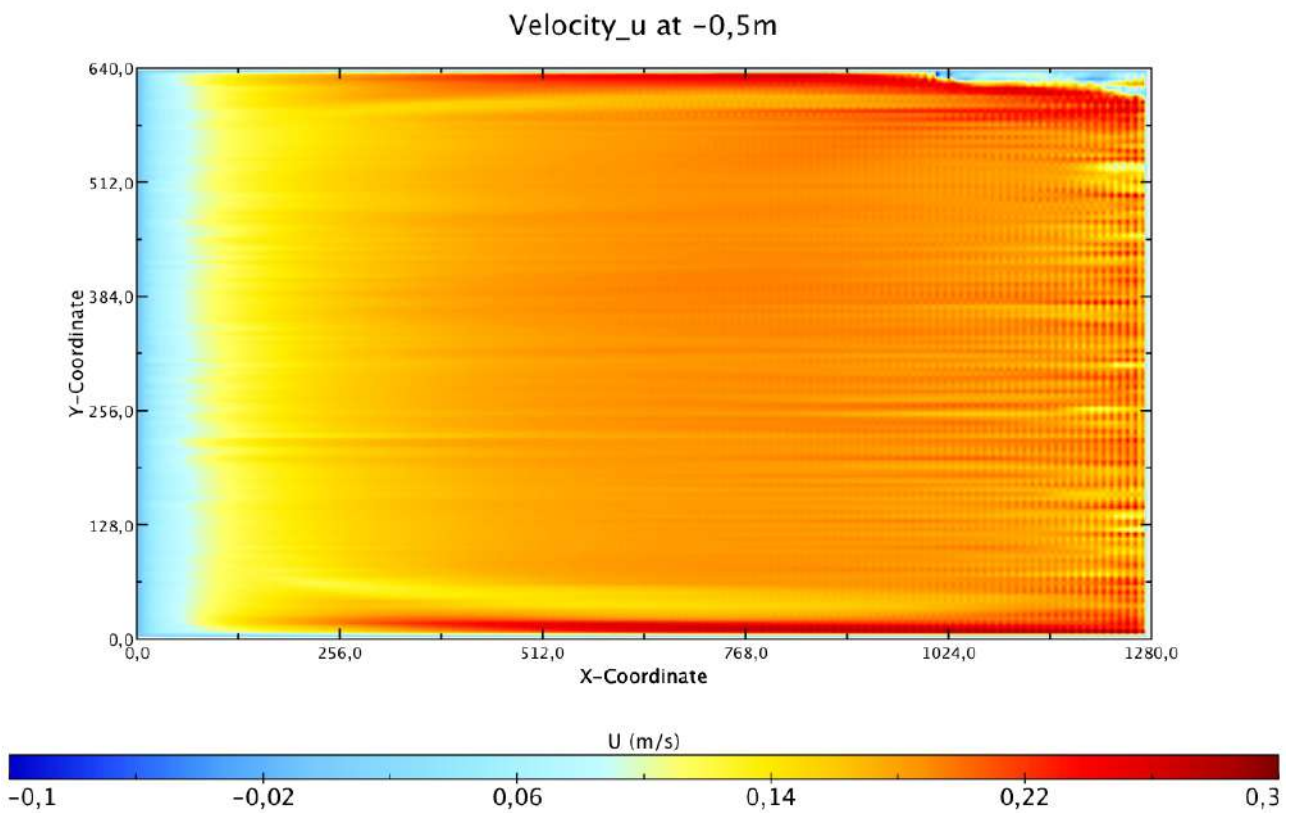


Fig. 4.25: Simulation 33 (viscC2=0; viscC4=0.5; viscC2D=0; viscC4D=0.5)

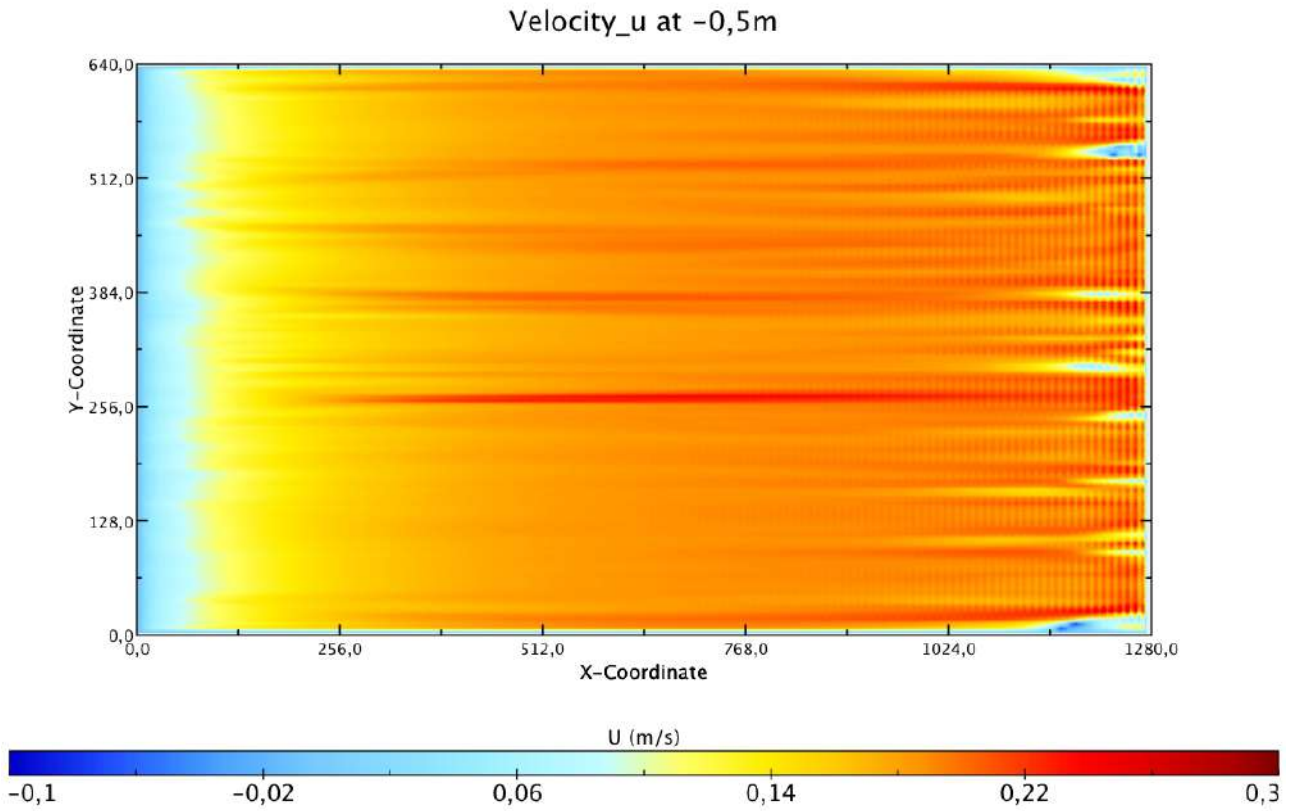


Fig. 4.26: Simulation 1 (viscC2=0; viscC4=1; viscC2D=0; viscC4D=1)

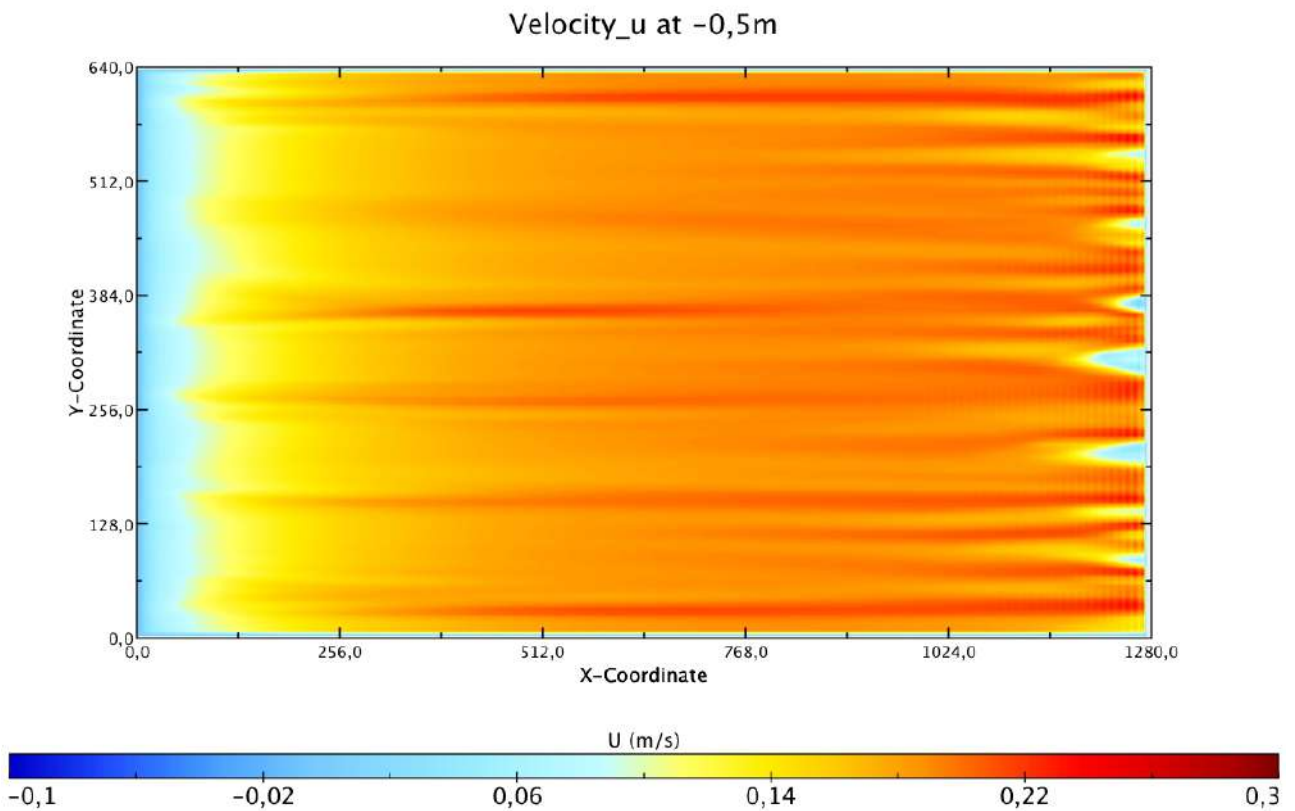


Fig. 4.27: Simulation 32 (viscC2=0; viscC4=2; viscC2D=0; viscC4D=2)

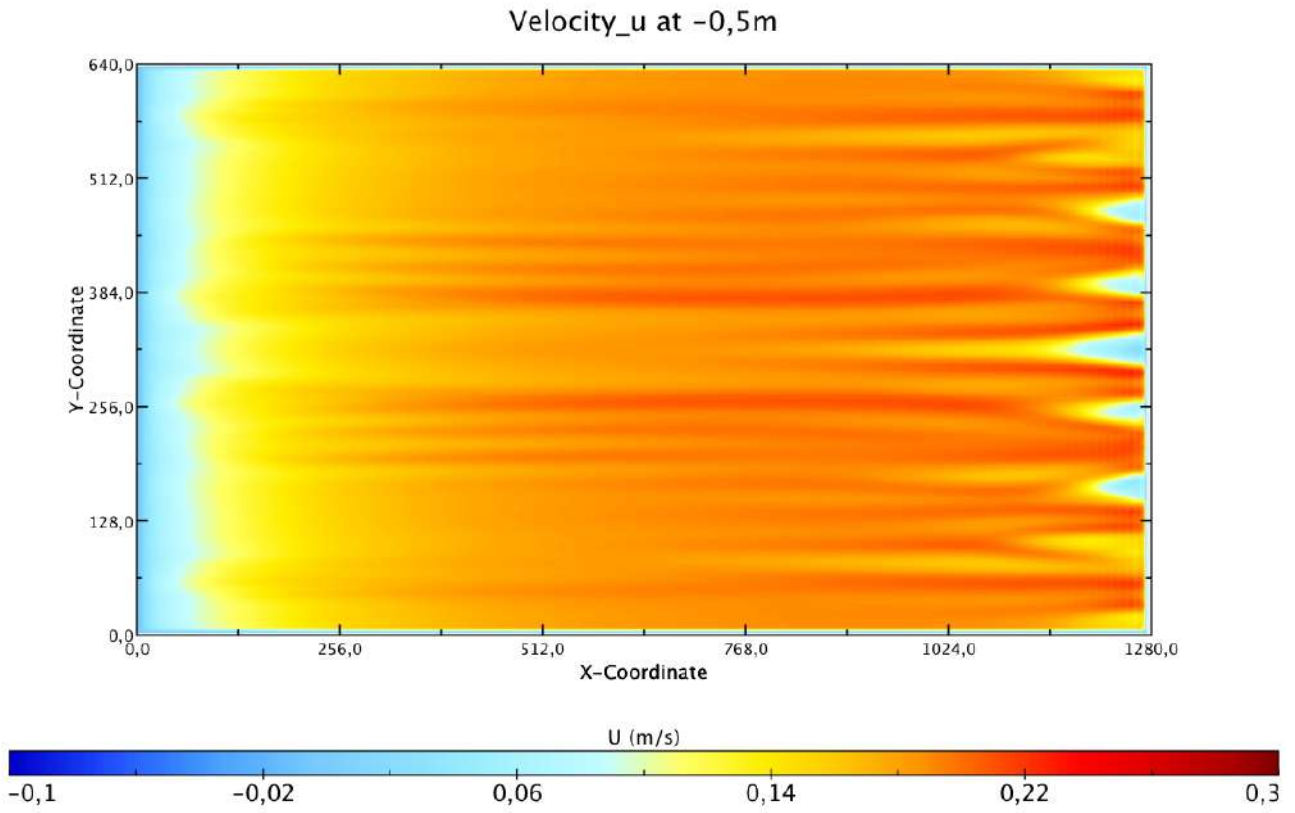


Fig. 4.28: Simulation 2 (viscC2=0; viscC4=3; viscC2D=0; viscC4D=3)

The configuration used for the “simulation 33” has been selected and thereafter the vertical mixing scheme has been tuned. The results are shown below and the parameters are shown in the following table 4.4

Table 4.4

Sim	Vert. Mixing	Setting	Horiz. Mixing	Setting
38	GGL90	Ck=0.15;Ceps=1.0;LengthMin=1.e ⁻²	LEITH	viscC2=0; viscC4=0.5; viscC2D=0; viscC4D=0.5

Instantaneous filed

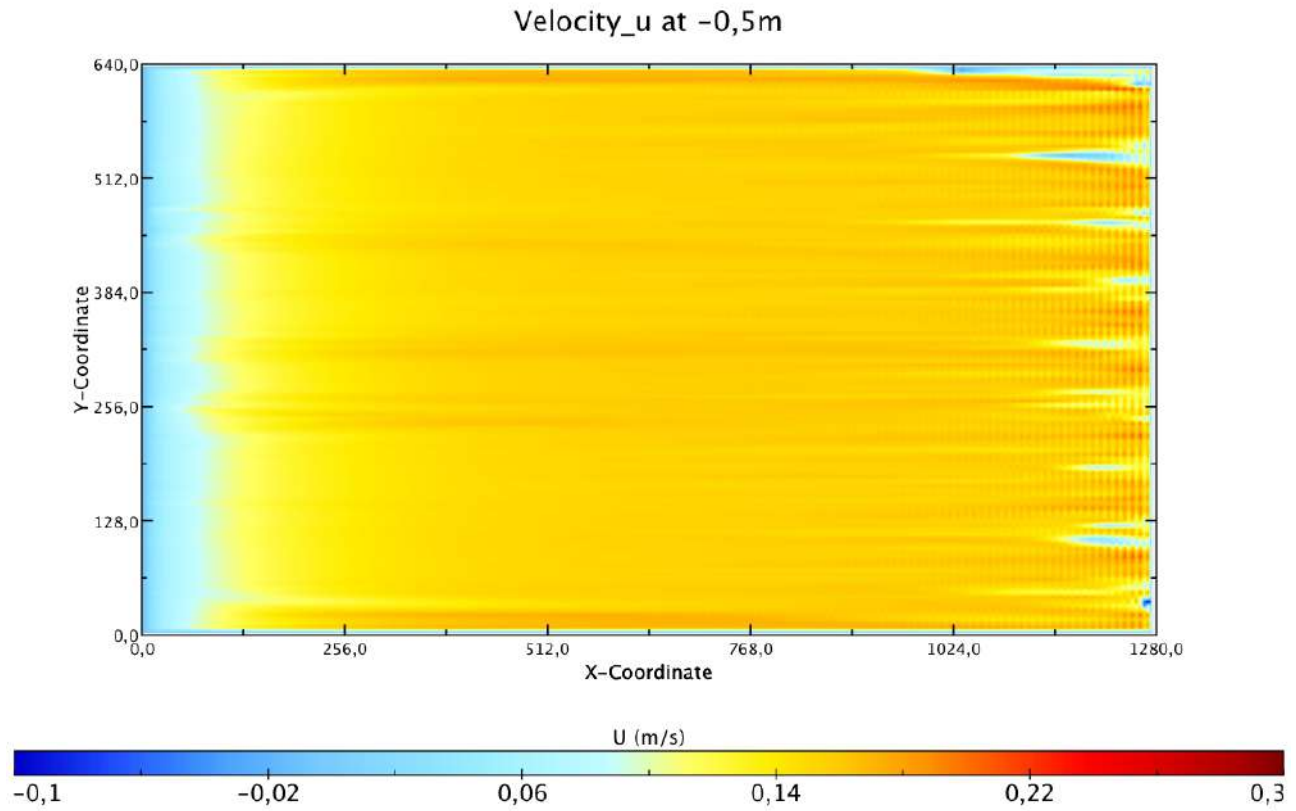
Figures 4.29 (A and B) and 4.30 (A and B) show the contour plot of U and V component of the horizontal velocity at -0,5m and -31,5m.

It is possible to recognise the effect of ggl90 scheme, tuned for shallow water; Indeed, lower values of the U component at the surface, with respect to the results obtained by the previous MIT simulation, are shown.

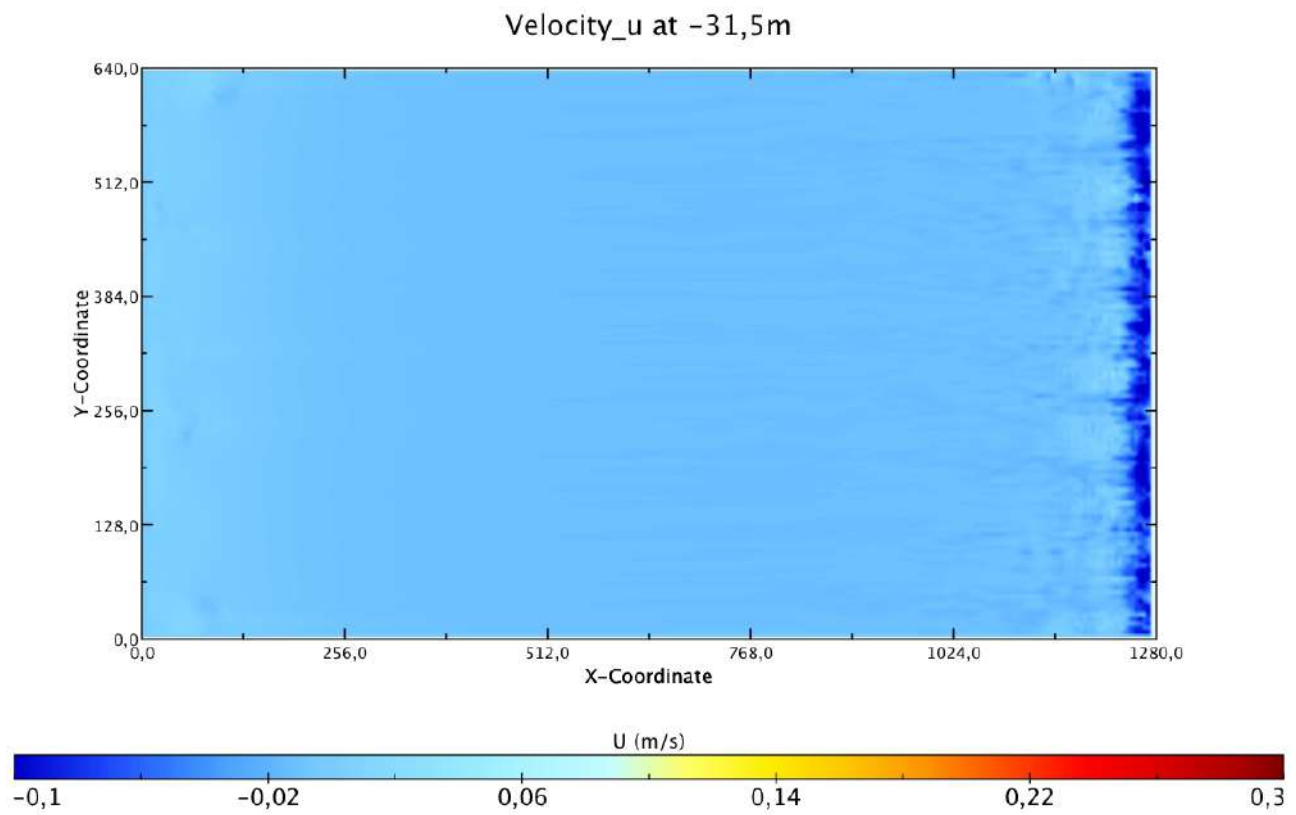
Comparing the velocity field developed by simulation n.29 (constant values of horizontal eddy viscosity) with this one, it is possible to claim that the latter is clearly less homogeneous, showing structures similar to the streaks observed in LES simulation.

The vertical velocity (Fig 4.32) is influenced by the horizontal mixing scheme, too, showing a more detailed circulation close to the boundary.

Finally, no total convergence towards the ground truth reference (LES) has been attained. But it is possible to assert that best results have been achieved by using Leith viscosity for the horizontal mixing parameterization.

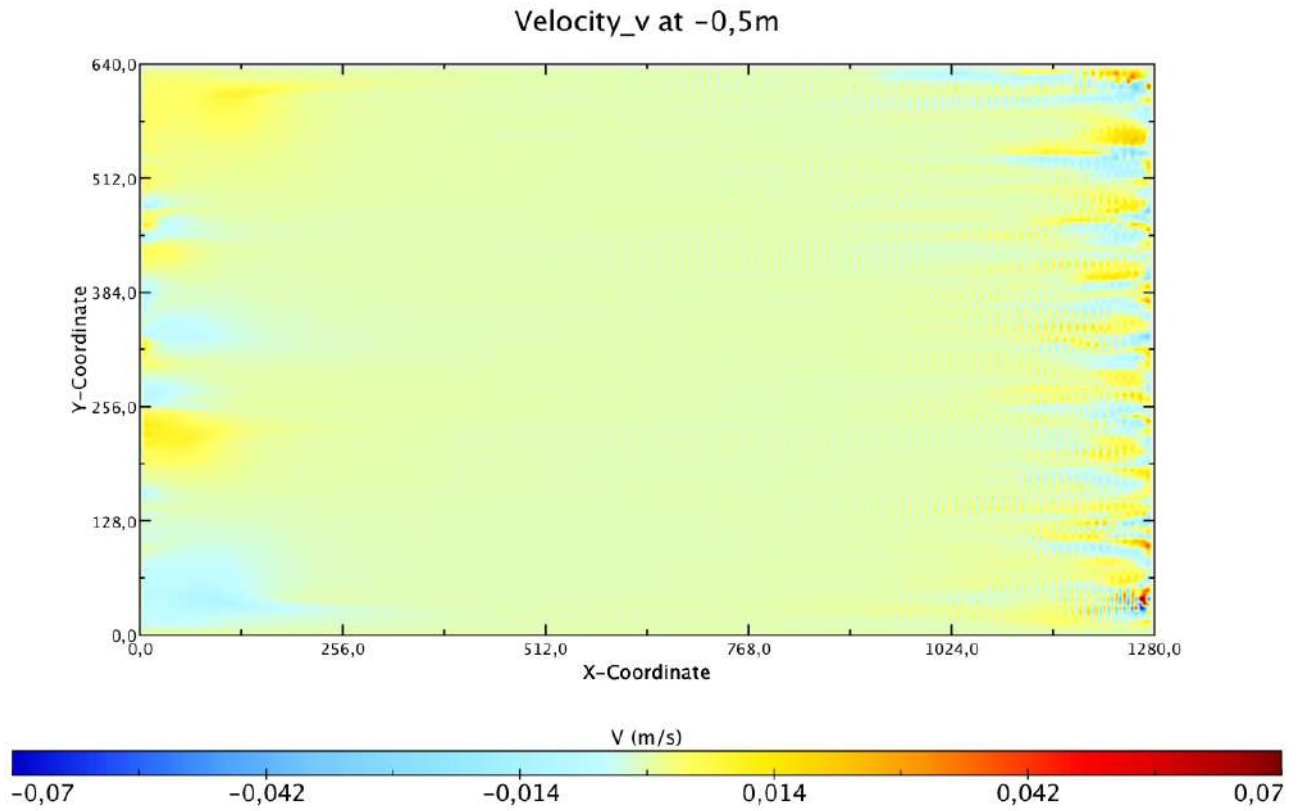


A)

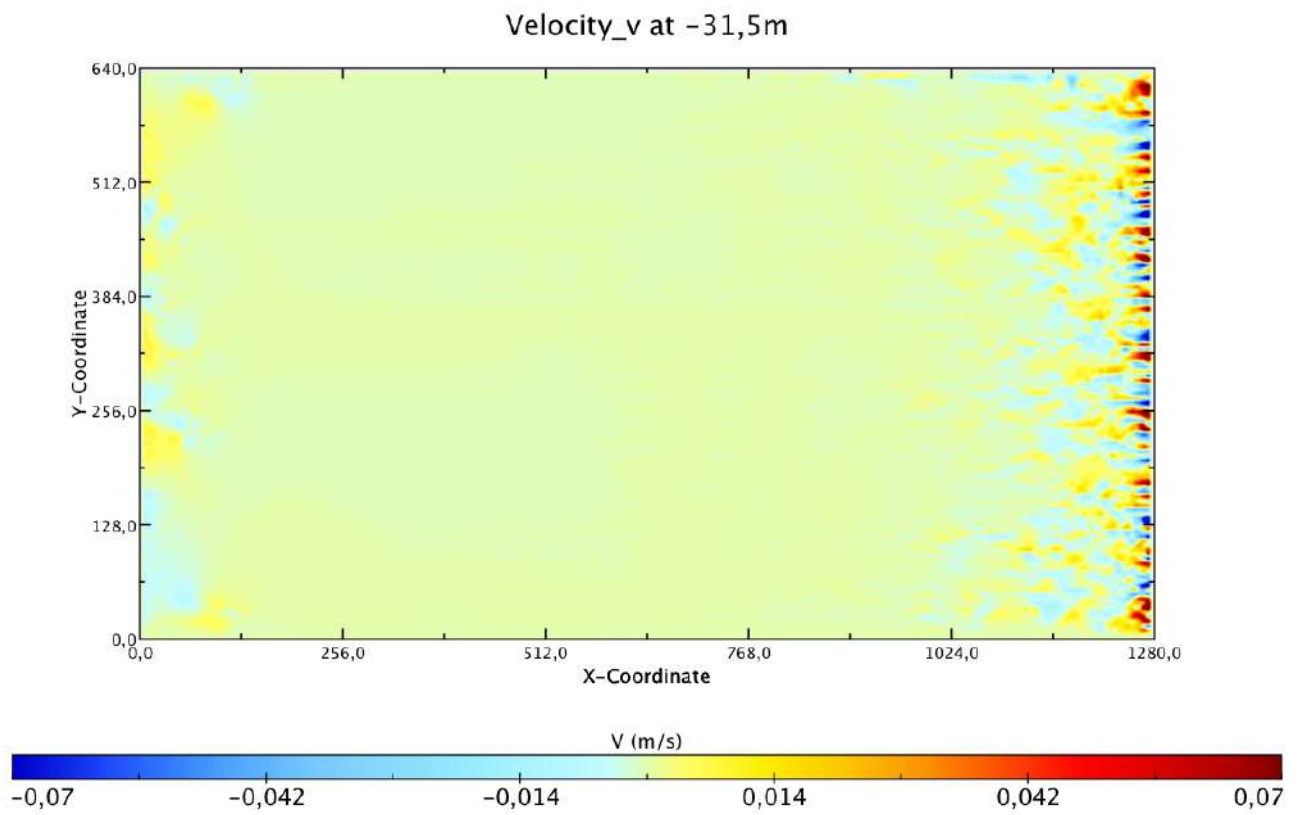


B)

Fig.4.29: Contour plot of U component of the horizontal instantaneous velocity at two horizontal planes: (A) -0,5m; (B) -31,5m



A)



B)

Fig.4.30: Contour plot of V component of the horizontal instantaneous velocity at two horizontal planes: (A) -0,5m; (B) -31,5m

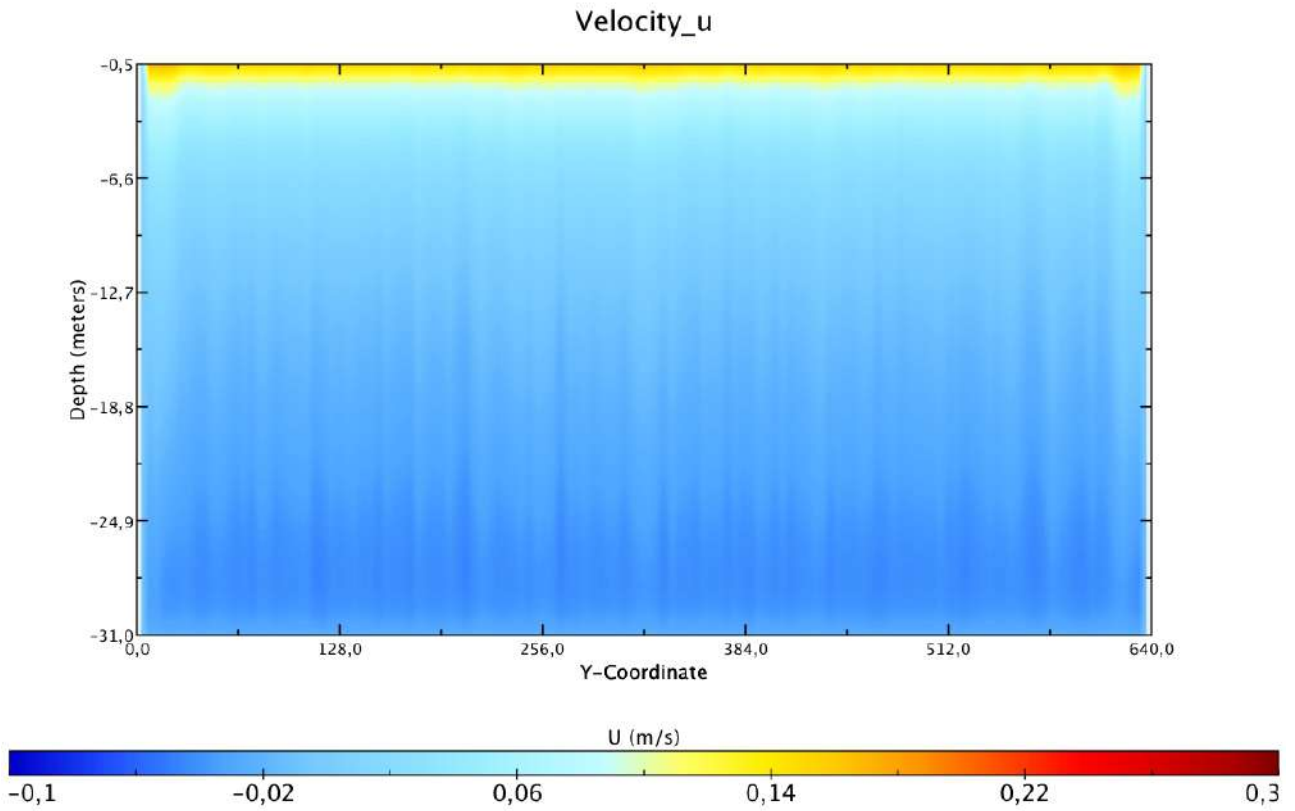


Fig.4.31: Contour plot of U component of the horizontal instantaneous velocity in a vertical plane (x-coord=640m).

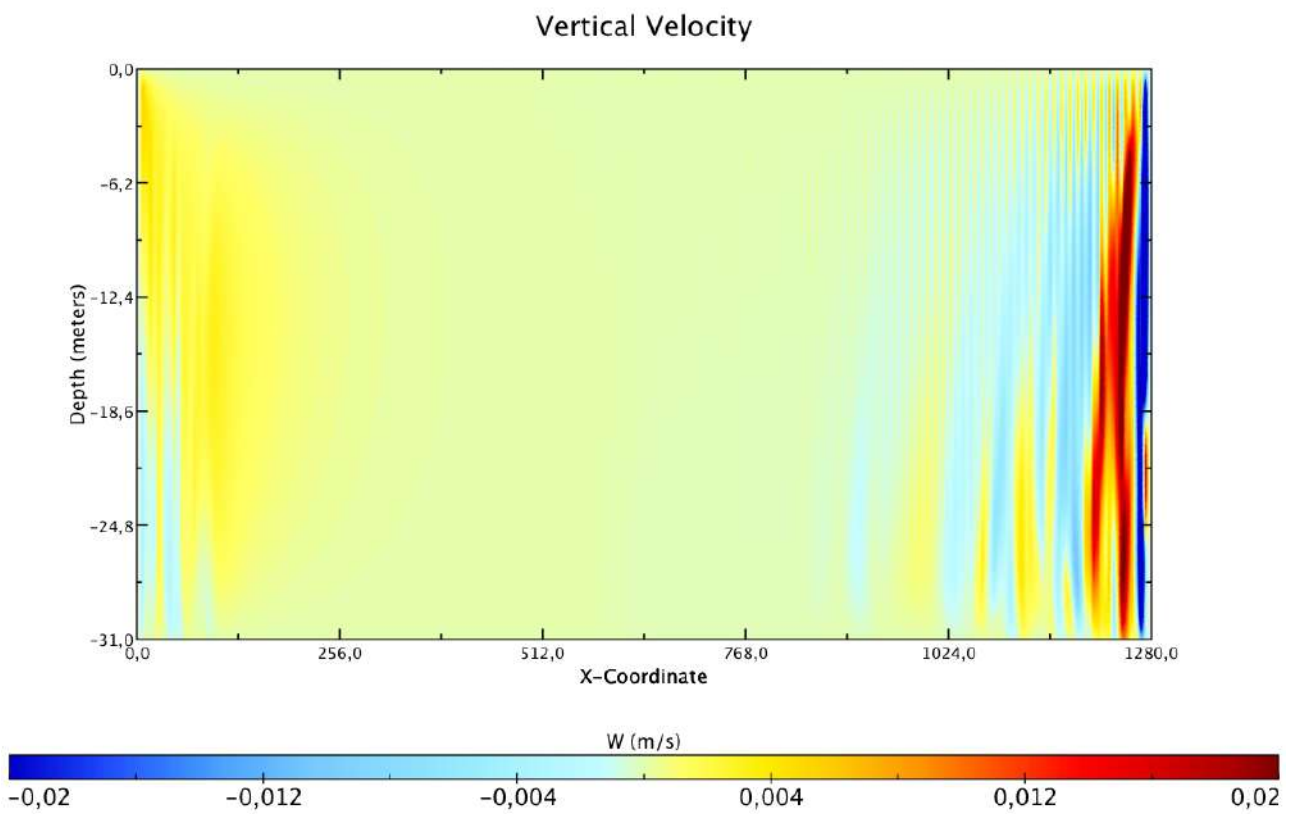


Fig.4.32: Contour plot of W component of the vertical instantaneous velocity in a vertical plane (y-coord=320m).

Turbulent Kinetic Energy and Eddy Viscosity

TKE and vertical eddy viscosity are influenced by the horizontal mixing scheme too.

It is possible to see how the simulation still develops less TKE (maximum value of 0,001) then LES simulation (maximum value of 0,0025), but shown a streaked field, absent in the simulation performed with constant value. In the following figures the minimum and the maximum values of the colour bar have been chosen in order to make the patterns clearer.

The distribution of turbulent kinetic energy (TKE) is illustrated for horizontal and vertical plane (Fig. 4.33 and 4.34)

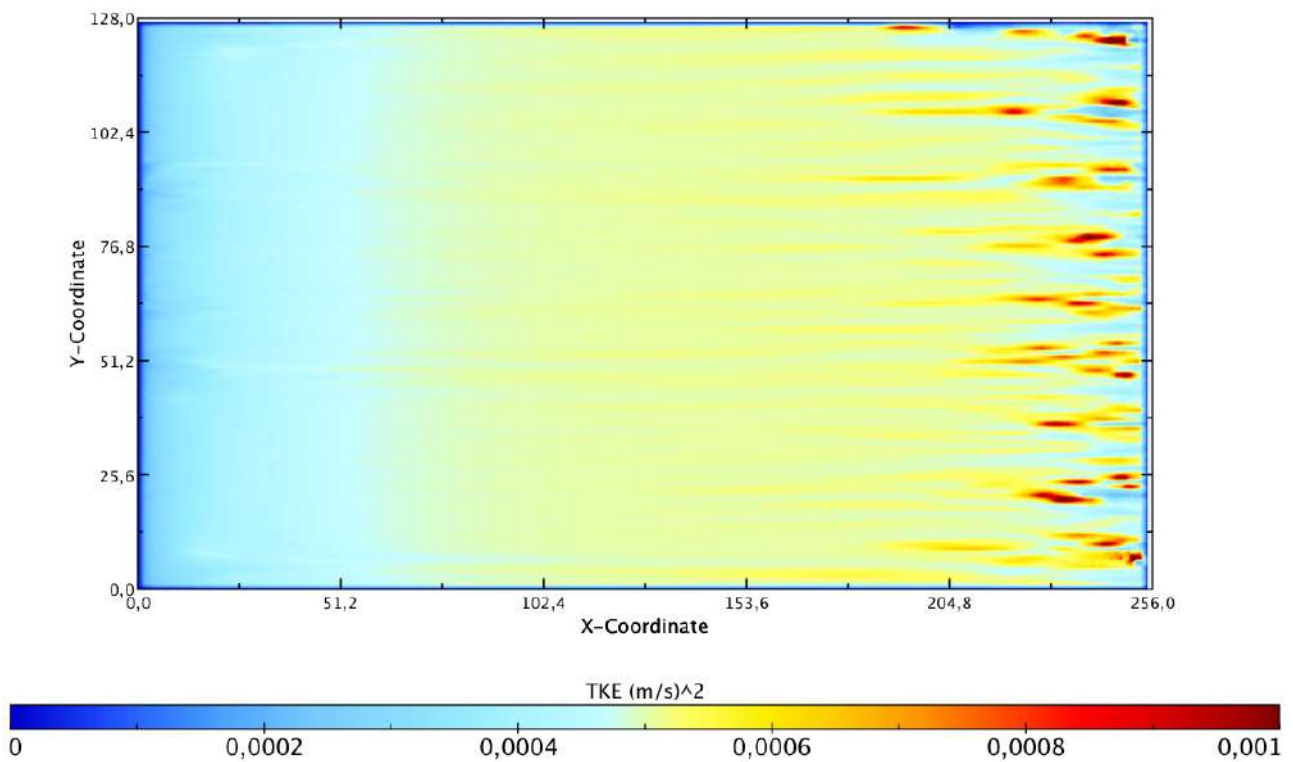


Fig.4.33: Turbulent kinetic energy at the surface. Grid cells are shown on x and y axes; Resolution 5 m.

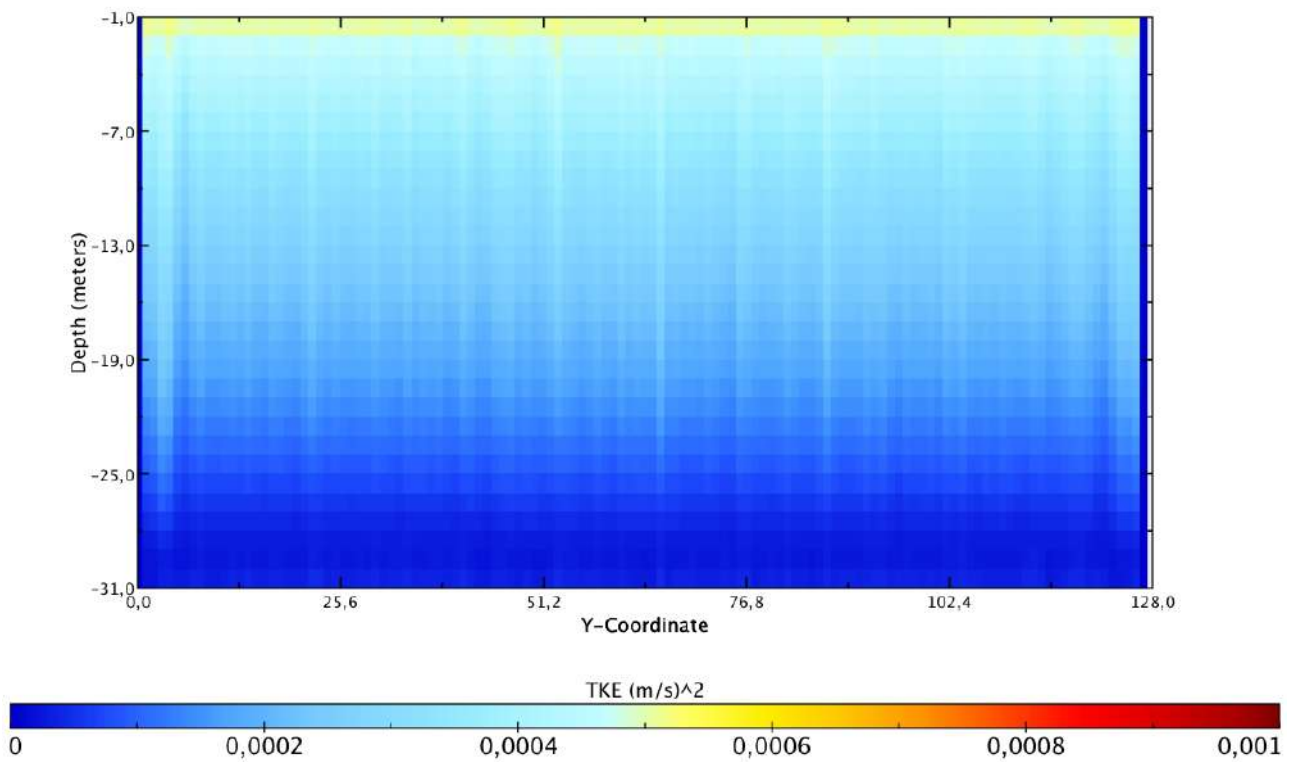


Fig.4.34: Vertical distribution of turbulent kinetic energy in a vertical plane. Grid cells are shown on y-coord; Resolution 5 m (x=128).

Figure 4.35 illustrates the distribution of the not homogeneous vertical eddy viscosity

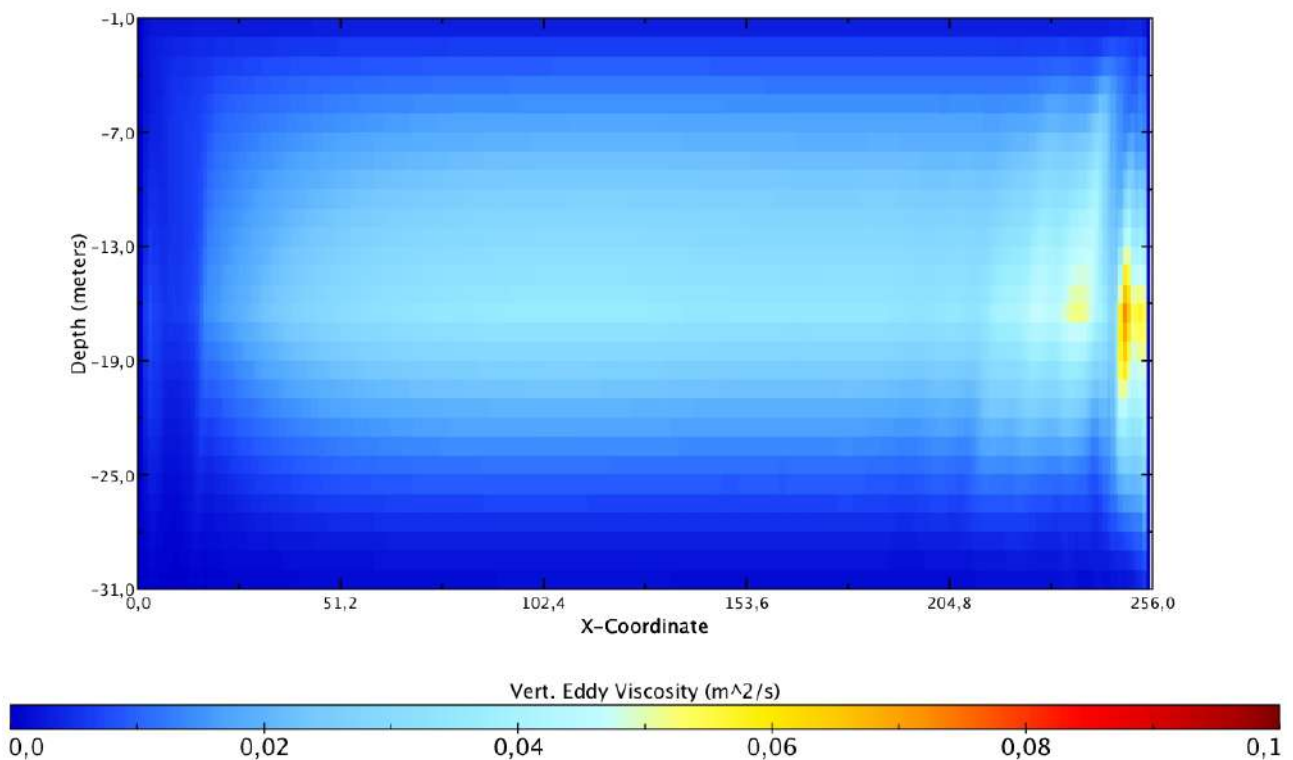


Fig.4.35: Vertical distribution of vertical eddy viscosity. Vertical plane, grid cells are shown on x-coord; Resolution 5 m.

Chapter 5 – Nesting Procedure

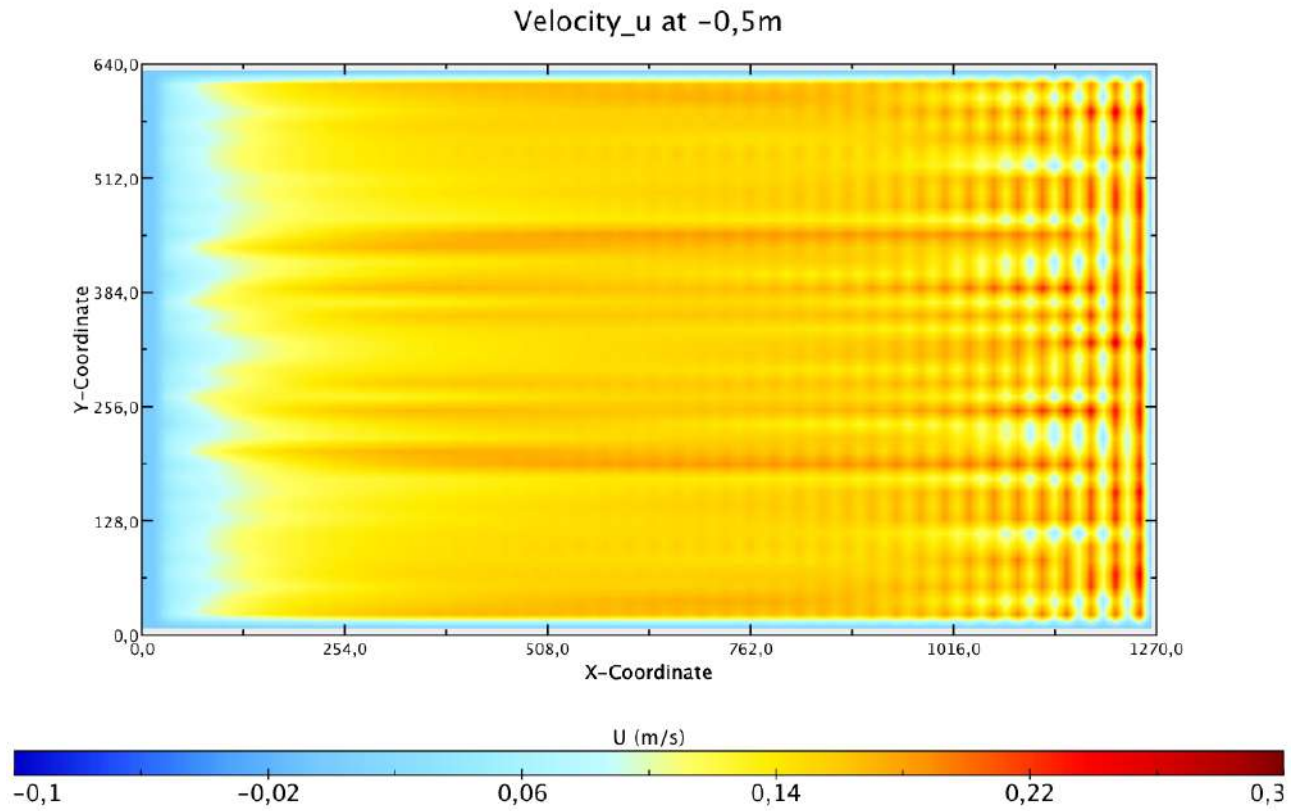
Downscaling output from MITgcm model and coupling it with the LES-Coast model.

In this chapter a nesting procedure, between the two codes, is illustrated.

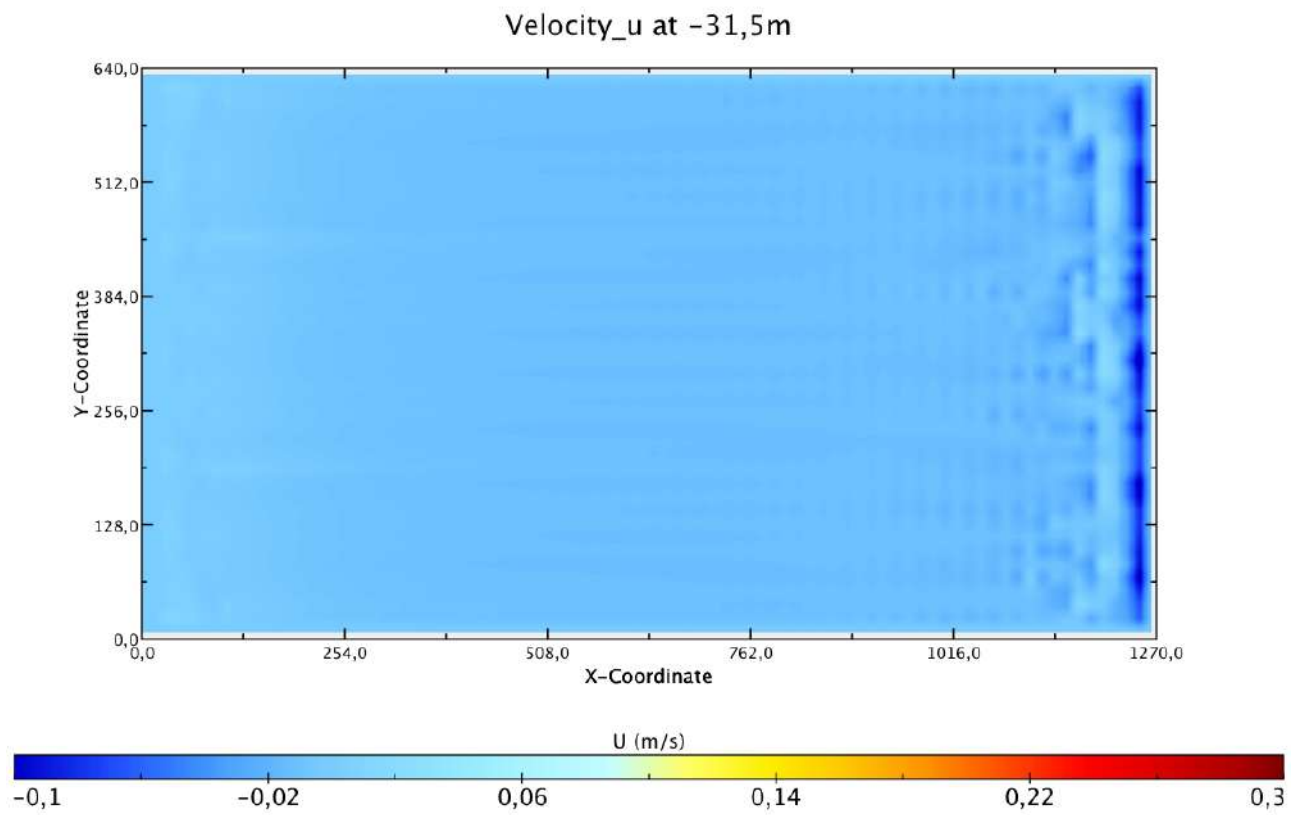
Identified the more suitable configuration for the MITgcm, as discussed in the previous chapter, the computational grid has been downscaled in a coarse resolution. The domain (measuring 1280m X 640m X 32m) is now discretized in 84 x 42 grid cells in horizontal direction and 32 cells in vertical direction. With this discretization, the dimensions of the cells are about $\Delta x \approx \Delta y \approx 15$ m and $\Delta z \approx 1$ m. With respect to LES configuration, computational cells differ by a factor of 3 in the horizontal.

Experiment with the MIT code, tuned with this coarse resolution, has been carried out and the outputs from this simulation have been used as inflow for the LES code, in a nesting procedure. Figures 5.1 (A)-(B), 5.2 (A)-(B), show the contour plot of U and V component of horizontal velocity, at two different depths. It is evident how the resolution of the computational grid is a key factor in order to achieve even better results. Indeed, by the use of fine grids, it is possible to solve physical processes otherwise parameterized and, consequently, it is possible to obtain patterns more realistic. On the other hand, because of computational costs, high-resolution simulations are often not feasible, therefore there is a need for developing a nesting with finer model only at certain areas of interest.

From now-on, this MITgcm coarse-configuration has been used in the “MIT-LES downscaling coupling framework”.

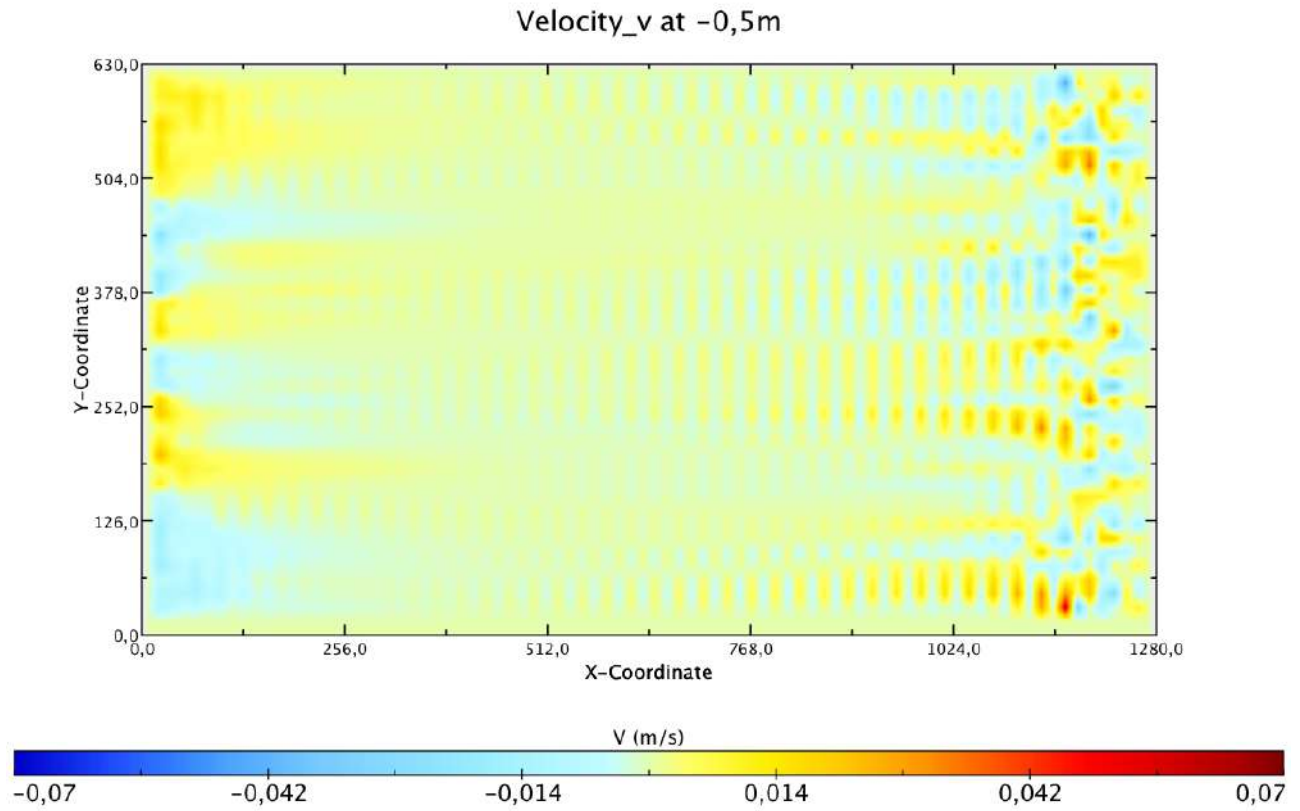


A)

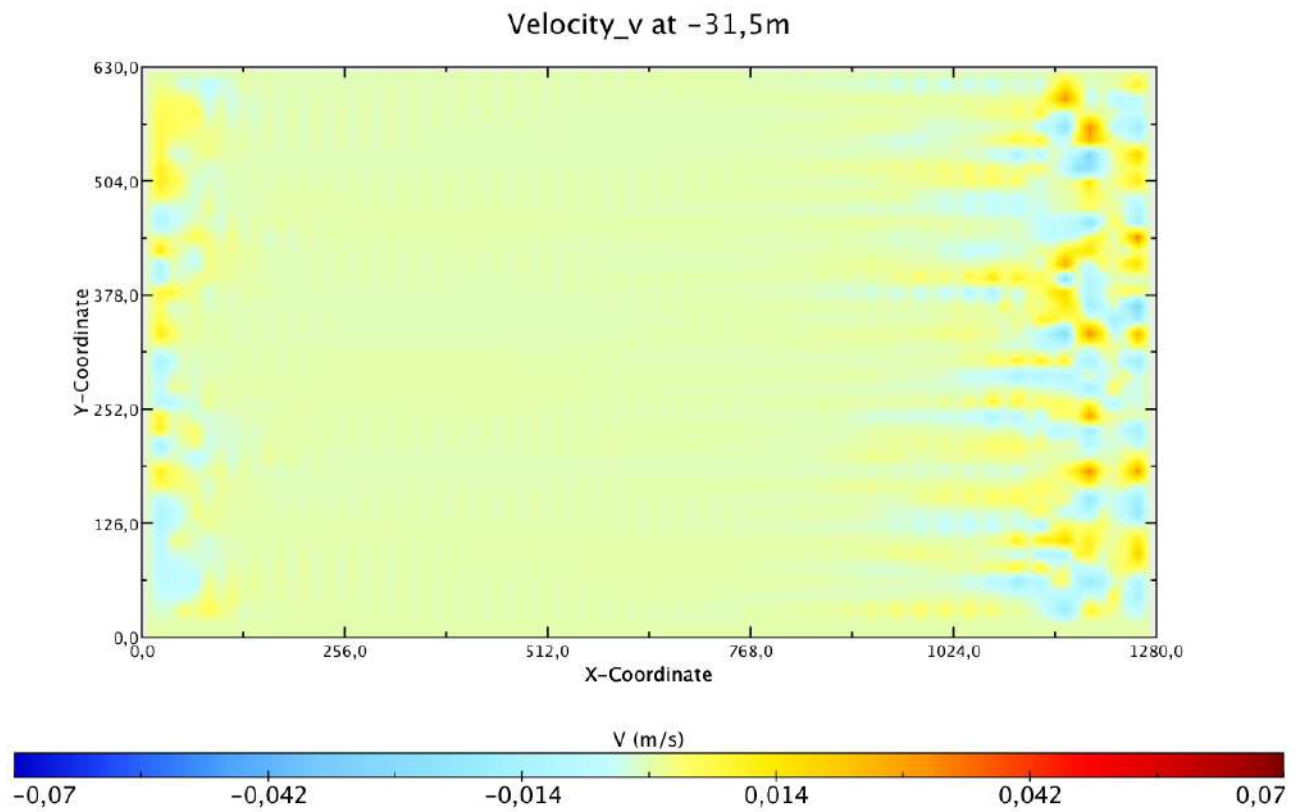


B)

Fig.5.1: Contour plot of U component of the horizontal instantaneous velocity at two horizontal planes: (A) -0,5m; (B) -31,5m. MITcgm simulation performed with Leith scheme.



A)



B)

Fig.5.2: Contour plot of V component of the horizontal instantaneous velocity at two horizontal planes: (A) -0,5m; (B) -31,5m. MITcgm simulation performed with Leith scheme.

5.1 One-way Nesting

The one-way nesting strategy has been so far the most popular approach employed by dynamical regional climate models (RCMs) for downscaling large-scale atmospheric information to regional scales (Denis et al., 2002). Along with simulating small-scale dynamics by RMCs, one-way nesting schemes help with the representation of large-scale features in RMCs by imposing initial and lateral boundary conditions, which are constructed by downscaling information from global models (Van Sy Pham et al., 2016).

Dynamical downscaling with nested regional oceanographic models has been demonstrated to be an effective approach for both operationally forecasted sea weather on regional scales and projections of future climate change and its impact on the ocean. However, when nesting procedures are carried out in dynamic downscaling from a larger-scale model to a smaller scale, errors are unavoidable due to the differences in grid sizes and updating intervals (Van Sy Pham et al., 2016).

The impact of the resolution difference between the driving data and the RCM, and the temporal updating frequency of the lateral boundary conditions (LBC), are two important topics that have not yet been rigorously studied (Denis et al., 2002). A particular problem discussed in this chapter is the one of the LBC temporal resolution.

In one-way “off-line” nesting procedure the update interval for the lateral boundary conditions must be specified. In “run-time” nesting, the nested finer domain and the outer coarser domain interact at every time step of the outer coarse-grid integration.

5.2 Off-line Nesting

The lateral boundary conditions for the nested finer domain are given by the stored coarser-domain output. Because larger data storage capacity is required when the update interval is smaller, a larger update interval is usually preferred to conserve computational resources (storage and input/output overhead costs). The optimal update interval has not been thoroughly investigated, because in the past the interval choice was highly constrained by practical computing choices. The standard or usually acceptable update interval for lateral boundaries in mesoscale simulations is a few hours (Michioka and Chow 2008).

For this part of the study, the time interval of the nesting LBC data is varied. To investigate the effect of the lateral boundary forcing update interval, three updating frequencies have been compared: 2 hours, 1 hours (for the off-line nesting case) and 9 seconds for the run-time case.

Procedure

MITgcm simulation is performed with a time-step of 9sec. while LES simulation with a time-step of 3sec; The MIT output serves as the initial and lateral boundary conditions for LES model simulation.

The MIT conditions are stored at 1h intervals in the Netcdf format and later bi-linearly interpolated in space and time to the LES model grid. A slice, from the center of the domain of the MIT simulation, has been used as inflow for the LES in a nesting framework (figure 5.3).

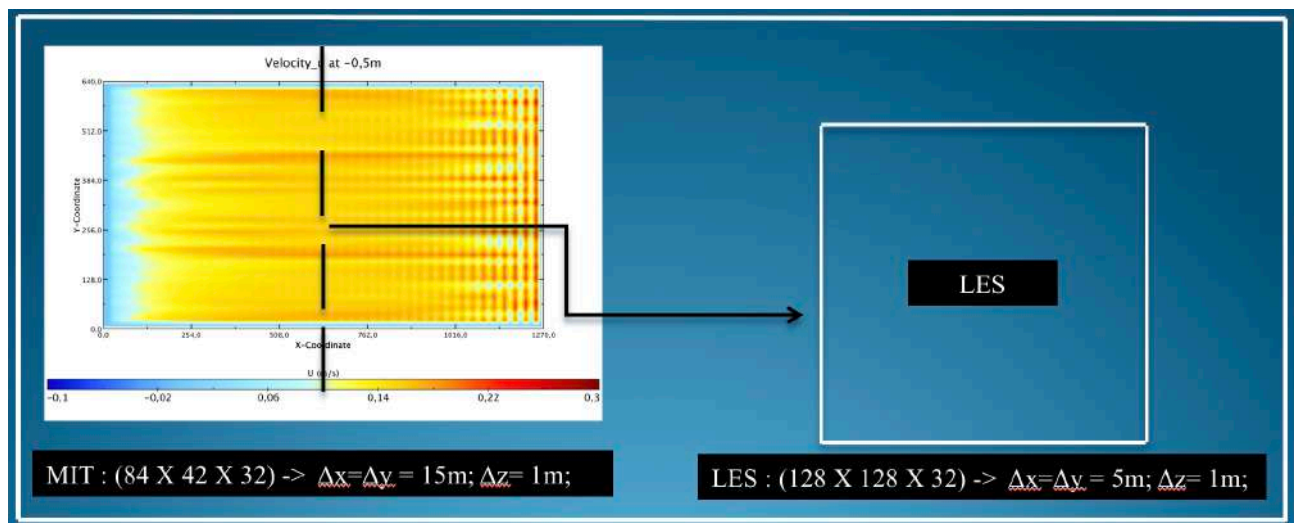


Fig.5.3: Nesting framework

The MIT uses a staggered, Arakawa-C grid, which stores thermodynamic data at cell-centroid, and velocity data at the respective face-centroid of the mesh. The MIT staggered data structure is transformed to LES Arakawa A-grid, where each variable is stored in the grid center.

Figures from 5.4 to 5.7 show the contour plot of U and V component of horizontal velocity at -0,5m and -31,5m after 48h of simulation, for an update interval of 2h and 1h, respectively.

It has been discovered how the “nested-LES” feels the effects of the nesting, showing, at the surface, higher values of variable U at the middle of the domain (absent in the simulation performed by LES stand-alone). Comparing the results of simulations MIT stand-alone (on the left) and LES after nesting (on the right), it is evident how the resolution of the field has been clearly improved. Moreover, the nested model has shown a remarkable sensitivity to the update frequency of the lateral boundary conditions, showing a slight difference in the evolution of the U component of velocity field at the surface.

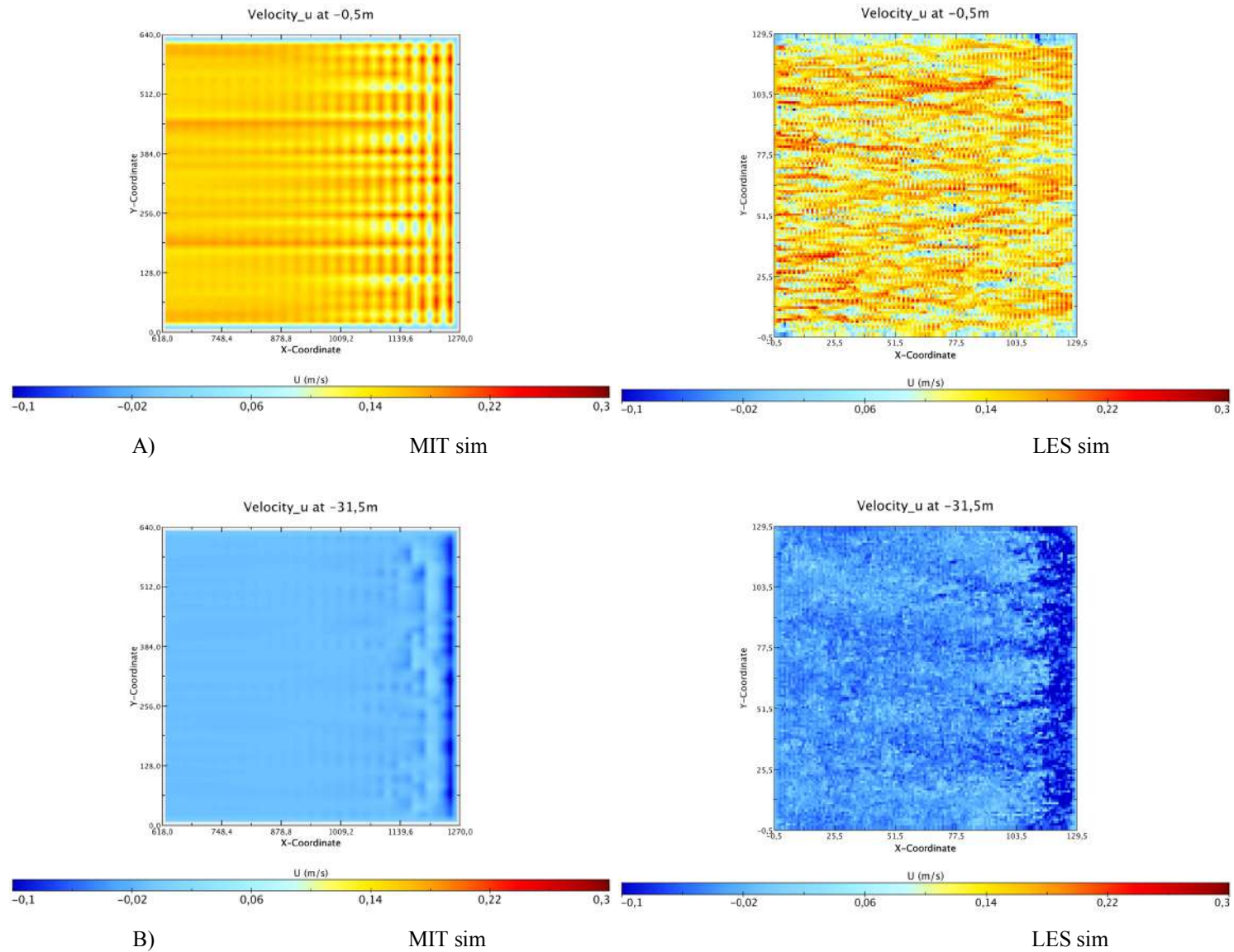


Fig.5.4: Contour plot of U component of the horizontal instantaneous velocity at two horizontal planes: (A) -0,5m; (B) -31,5m. Interval update of boundary conditions: 2h.

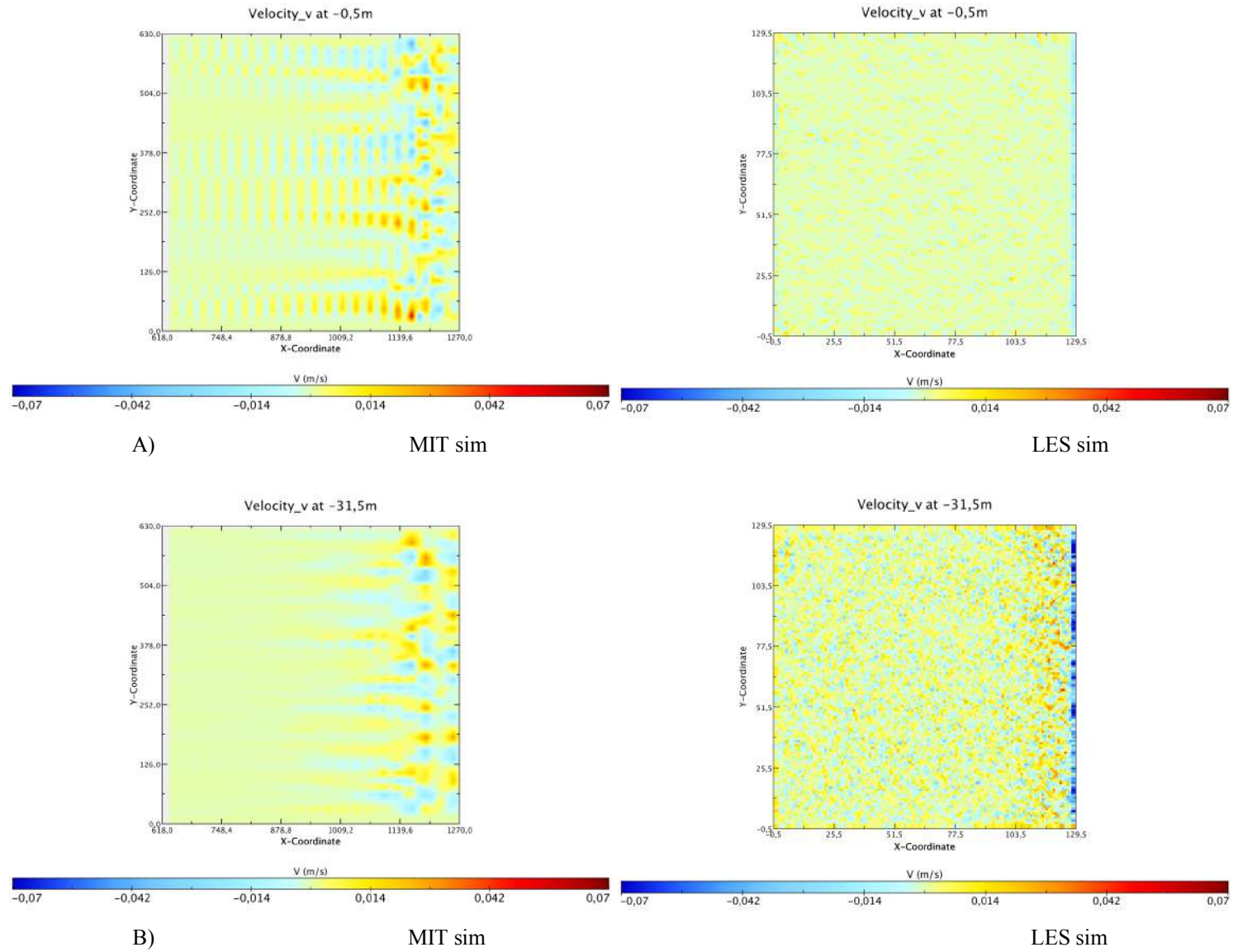


Fig.5.5: Contour plot of V component of the horizontal instantaneous velocity at two horizontal planes: (A) $-0,5\text{m}$; (B) $-31,5\text{m}$. Interval update of boundary conditions: 2h.

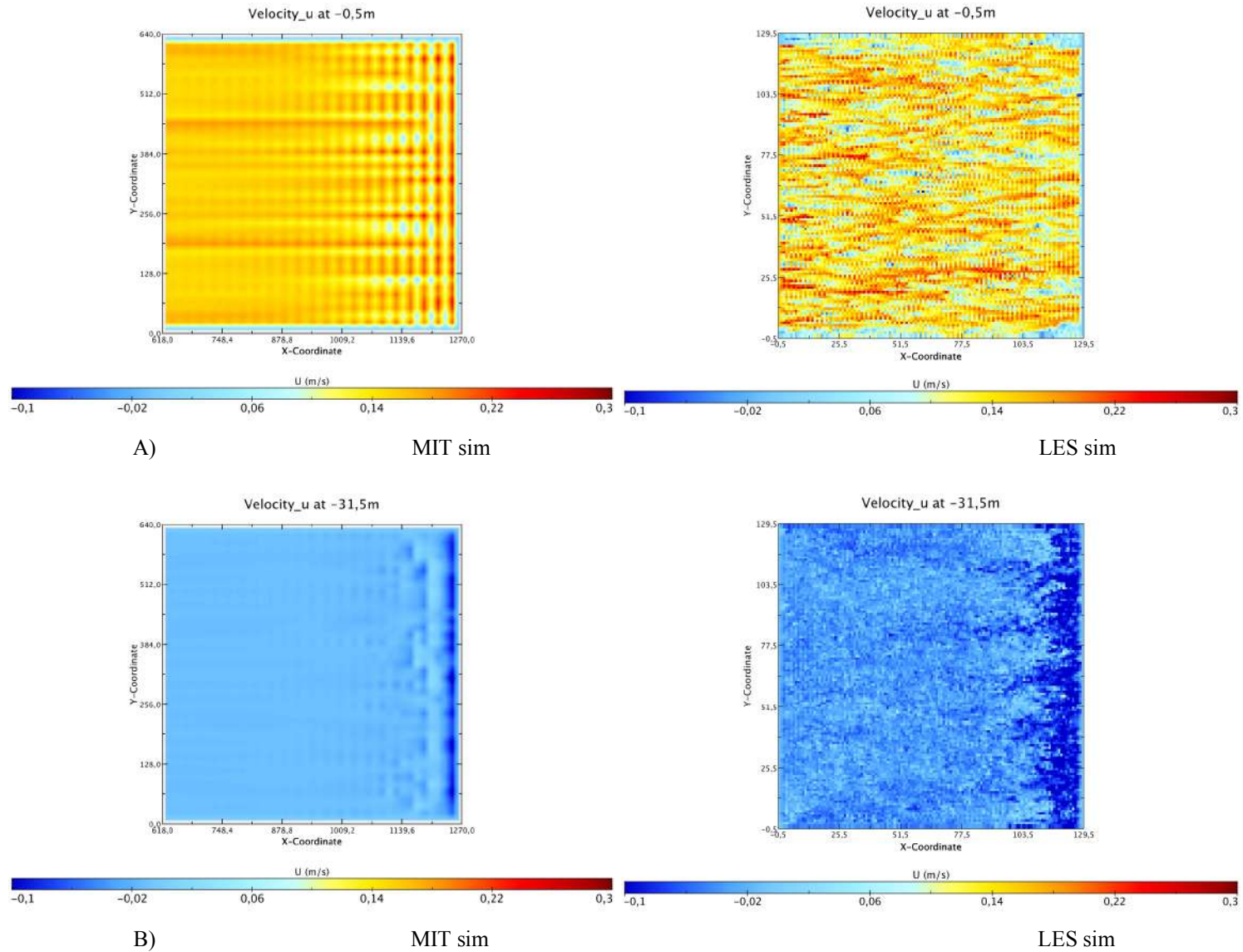


Fig.5.6: Contour plot of U component of the horizontal instantaneous velocity at two horizontal planes: (A) -0,5m; (B) -31,5m. Interval update of boundary conditions: 1h.

5.3 Run-time Nesting

Starting from the model configuration described in the previous paragraph, a new methodology for a nesting in run-time has been first designed and then developed.

The two models are coupled now via an external driver that establishes the connection, passing information from MITgcm to LES-Coast and that performs also all the necessary interpolations. To strongly reduce the communication cost between the driver and the two parallel models, a parallel version of the driver has been developed. This driver represents the main core of the developed procedure. The coupler has been written in Fortran90 and has been compiled with “mpiifort”. The peculiarity of this new method has been to have created a new global MPI environment (named COMM_WOLRD) and to have changed the previous setting “comm_world” of each model to a new “comm_local”. Then, in order to allow the communication between these three codes (2 models plus driver), both models have been deeply modified; i.e. the insertion of new variables and new “include” files it was necessary, as well as a new initialization of the MPI environment for each model.

Nested Model

The nested model consists of two models: a coarse grid model (MITgcm) and a fine grid model (LES-Coast).

The MITgcm is used in its non-hydrostatic, implicit free-surface, partial step topography formulation. The horizontal refinement ratio of the nested model is 3:1, while no refinement in the vertical has been used, i.e. the LES-Coast uses the same vertical levels of the MITgcm.

Procedure

The approach can be summarized as follows:

- 1) The MITgcm is forwarded one-time step (9seconds).
- 2) The new MITgcm dynamical fields are interpolated and applied as lateral boundary conditions to the LES-Coast.

It is obtained by a bi-linear interpolation of the velocity components of the coarse grid. It is obtained in two steps: during the first step they are linearly interpolated normally to the boundary, then, these new values are interpolated tangentially.

- 3) The LES-Coast is forwarded three-time steps (3 seconds each one) and the lateral boundary forcing is linearly interpolated at intermediate times between update intervals.

Technique

In the present nested model MITgcm and LES-Coast are both treated as independent models, except for the communication parts. The two models run in parallel, together with an external driver that establishes the connection between MITgcm and LES-Coast.

The MITgcm model sends all the calculated variables to the driver at every time step, then the driver (that is in receiving position), after performing all the proper interpolations, sends the new variables to LES-Coast model that can continue its simulation (fig.5.8).

The MPI message-passing standard is used for communication between the driver and the two models.

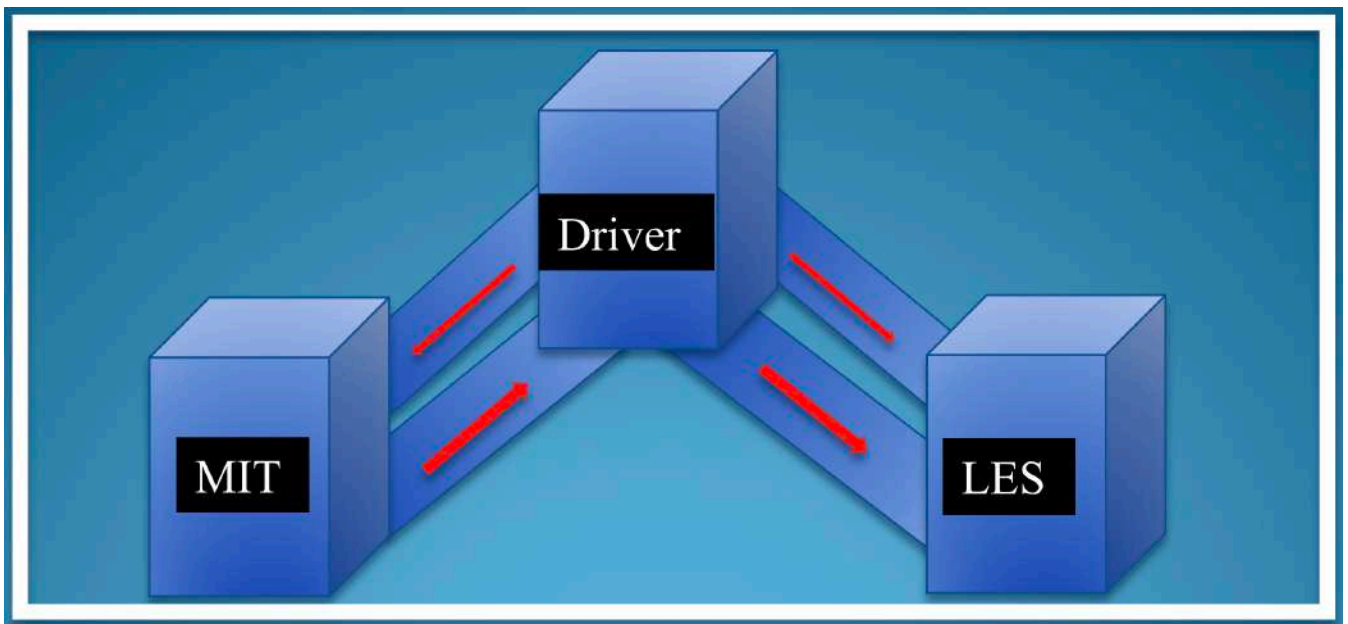


Fig.5.8: Framework of the nested model

Results

Figures 5.9 (A and B) and 5.10 (A and B) show the contour plot of U and V component of horizontal velocity at -0,5m and -31,5m after 48h of simulation.

The effect of the nesting is still evident and the resolution of the field has been clearly improved.

The good agreement found between the velocity field developed by this new “integrated model” and that previously realized, confirms both the robustness and effectiveness of the new model.

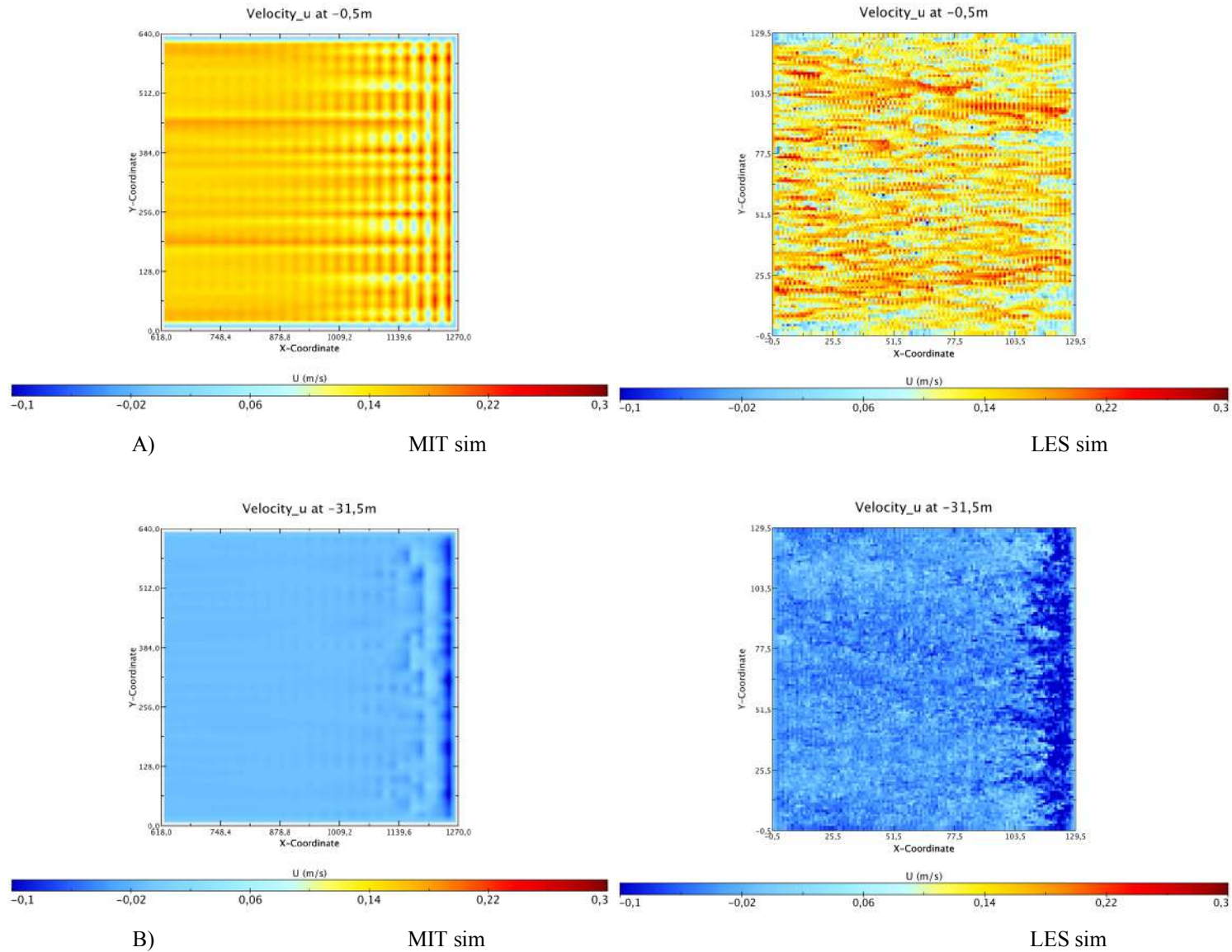


Fig.5.9: Contour plot of U component of the horizontal instantaneous velocity at two horizontal planes: (A) -0,5m; (B) -31,5m. Interval update of boundary conditions: 9 sec.

Update intervals for the lateral boundary forcing

Initial and boundary conditions produced by coarser global models do not have small-scale fluctuations, therefore, the nested model takes spin-up time to generate sufficient amount of them (Van Sy Pham et al., 2016). Initial conditions interpolated from the rough MITgcm data, indeed, do not have the small-scale features that LES should produce. Small-scale fluctuations contribute not only to kinetic energy but also to dissipation rate and to having similar amounts and distribution of energies and dissipation. During spin-up time, small-scale perturbations, which were not included in the roughly resolved LBC, are generated.

The increase in Kinetic Energy is interpreted as the growth of small-scale motions, which are produced by the energy cascade from larger scales through the process of breaking from the larger eddies to smaller eddies (Van Sy Pham et al., 2016).

Comparing the graphs of Kinetic Energy for the three LES simulations (figure 5.11), performed with different update intervals for the lateral boundary conditions, it is possible to determine how the small-scale motions grow in different way.

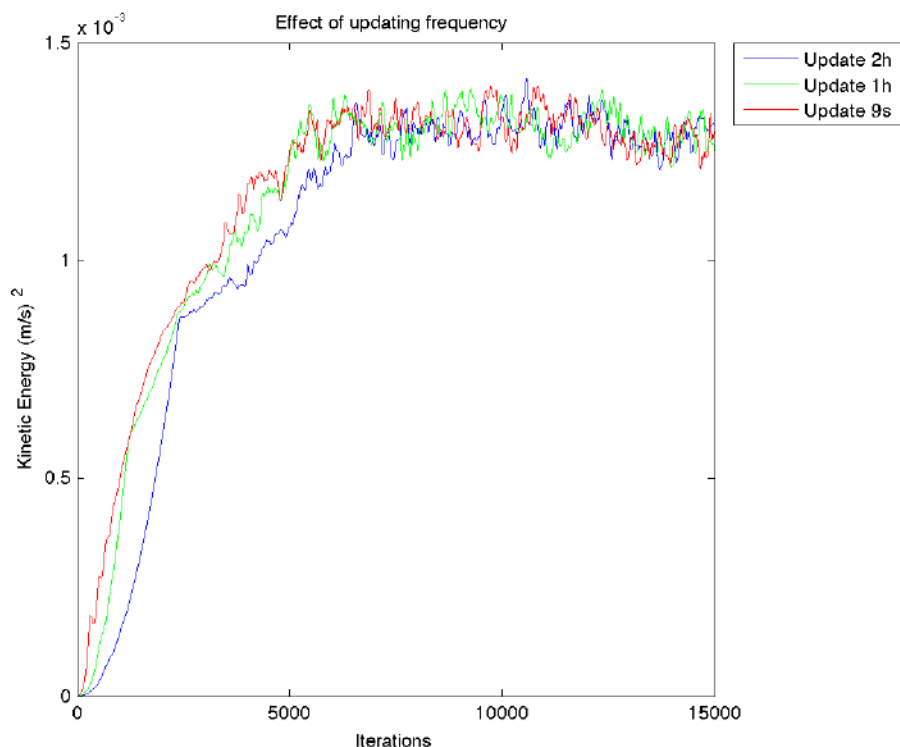


Fig.5.11:Kinetic Energy profiles. Nested model simulations performed with different update intervals: 2h (blu line), 1h(green line), 9seconds(red line)

It is possible to observe how as the update interval becomes smaller as the increment in KE becomes bigger. Discrepancies between the three simulations appear evident in the earlier period and appear unclear after the domain becomes fully saturated with small-scale fluctuations.

The Kinetic Energy is proportional to the vorticity (Denis et al., 2002). Therefore, the increase of KE could be commensurate with increasing the vorticity and, indeed, as described in “Denis et al., 2002”, fields more dominated by fine-scale features, such as the vorticity fields, are more sensitive to the update frequency of the lateral boundary conditions. Generally, as the update interval is set to be smaller, the model accuracy is improved (Michioka and Chow 2008).

Moreover, after 8 hours, KE seems to achieve a threshold at the equilibrium state. Assuming that the achievement of equilibrium is a spin-up level, 8 hours could be a spin-up time for producing small-scale motions.

Definitely, it is possible to believe that as updating becomes more frequent as the reproduction of the velocity field becomes of higher quality.

Chapter 6 – Stratified Case

The simulations described in the previous chapters have been conducted in presence of a neutral stratification.

With stratification in salinity, the buoyancy term in the Navier-Stokes equation cannot be neglected. In the present chapter a stable stratification case is analysed. In the following simulated case the salinity difference between the surface and the bottom is about 4 psu (figure 6.1).

A homogeneous and steady wind case has been considered, as already described in the previous chapters for the neutral stratification case.

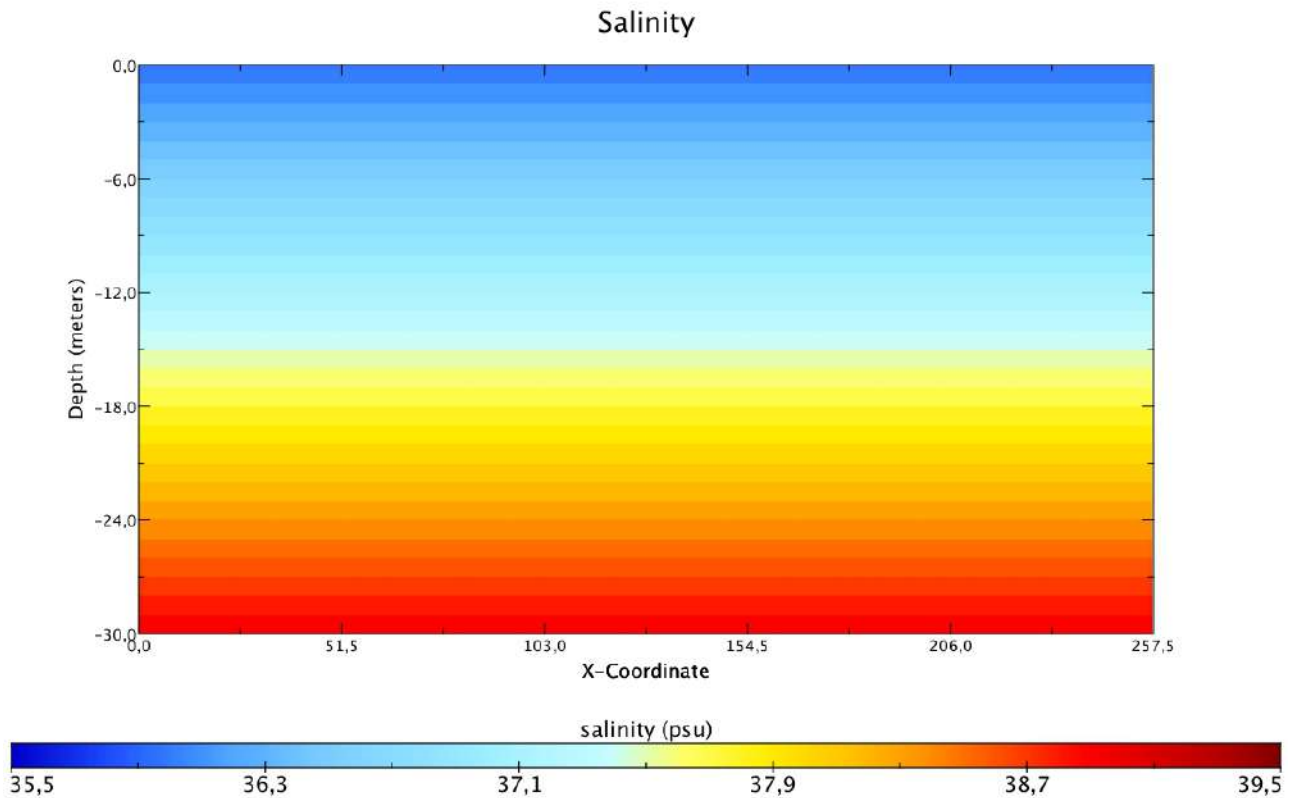


Fig.6.1: Contour plot of the initialized salinity field (vertical plane).

In order to estimate the effect of stable stratification on the wind driven circulation in a closed domain, a steady homogeneous westerly wind with $U_{10}=10\text{m/s}$ has been applied to the surface for 48 hours in absence of the Coriolis force. The salinity stratification has been initialized by imposing a salinity equal to 39,5 psu and 35,5 psu at the bottom and at the surface of the domain, respectively, and by applying a linear gradient between them.

As a representative example of the circulation occurring in presence of this homogeneous steady wind, snapshots at the end of simulations have been taken.

6.1 LES-Coast Simulation

In this section the results of the simulation performed by the use of LES-Coast model ($\Delta t=3$ sec), in a stand-alone configuration, are shown. The rectangular domain (measuring 1280m X 640m X 32m) is discretized in 256 x 128 grid cells in horizontal direction and 32 cells in vertical direction. With this discretization, the dimensions of the cells are about $\Delta x \approx \Delta y \approx 5$ m and $\Delta z \approx 1$ m.

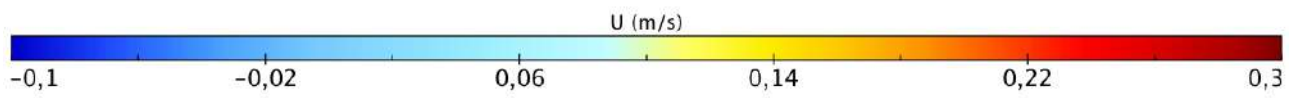
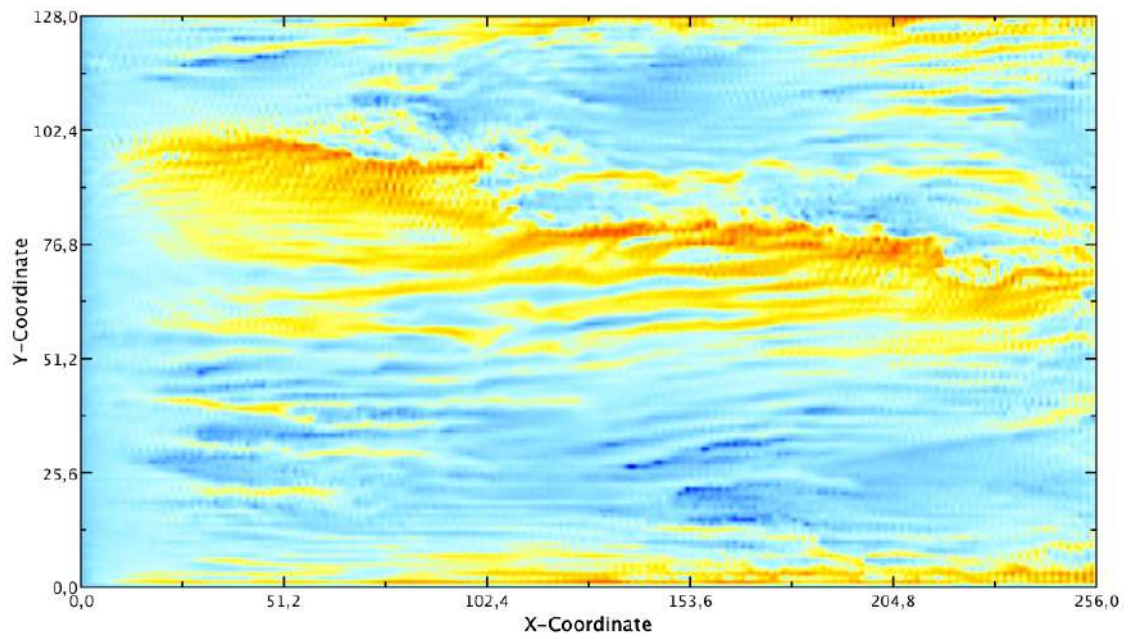
6.1.1 INSTANTANEOUS FIELD

Figure 6.2 (A)-(B) shows the contour plot of the U component of the horizontal velocity at two different depths. The current is aligned to wind direction and close to the bottom the velocity field is reversed with the respect to wind direction, as expected. It is possible to perfectly observe the presence of turbulent structures, with a streak of higher velocity in the middle of the domain.

The contour plot of the vertical velocity (figure 6.3) indicates the presence of an intense vertical mixing along the domain.

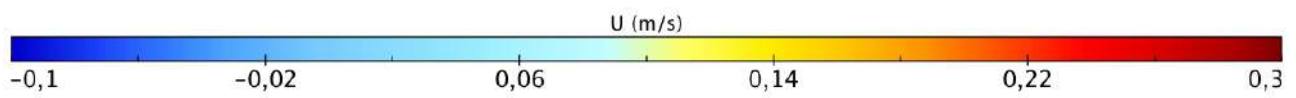
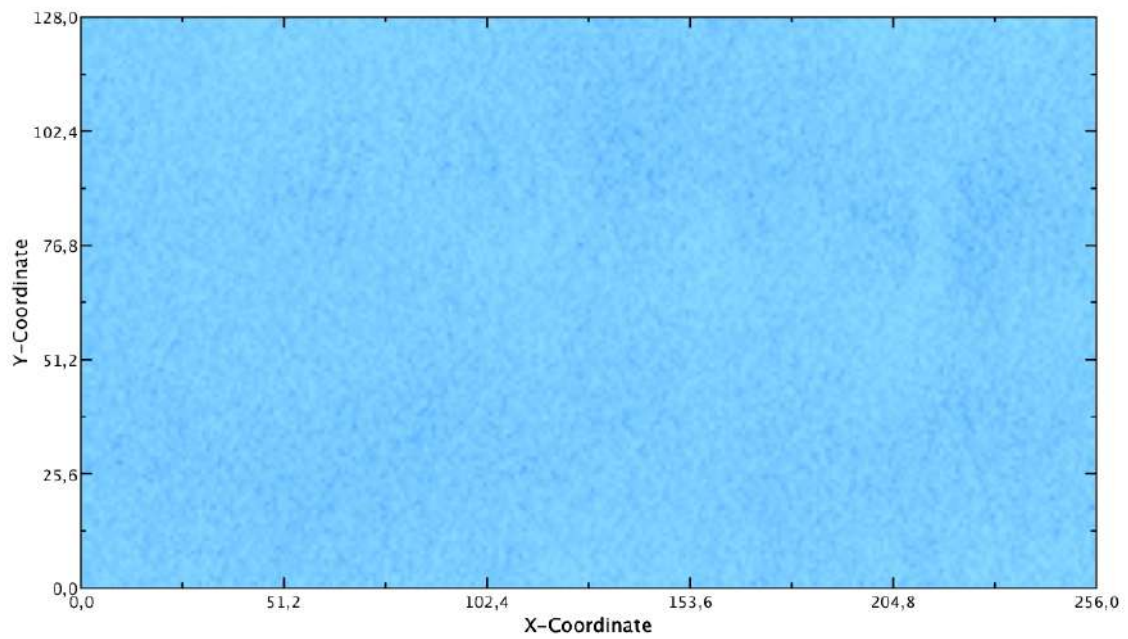
The contour plot of salinity field (figure 6.4) shows and confirms the presence of a well-mixed field. The initial linear stable stratification has been almost totally eroded, giving way to an upper layer less salty and a bottom layer with higher values of salinity.

Velocity_u at -0,5m



A)

Velocity_u at -31,5m



B)

Fig.6.2: Contour plot of U component of the horizontal instantaneous velocity at two horizontal planes: (A) -0,5m; (B) -31,5m. Grid cells are shown on x and y axes; Resolution 5 m.

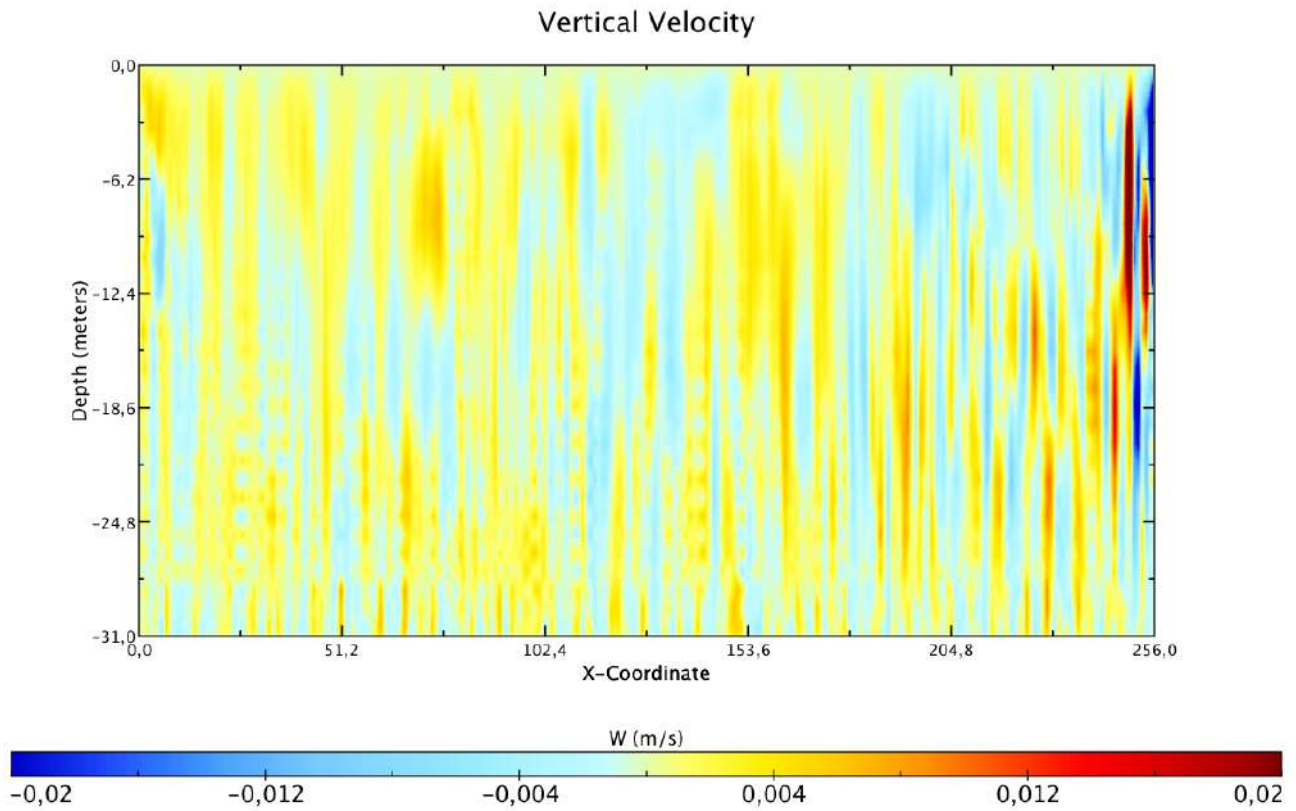


Fig.6.3: Contour plot of the vertical instantaneous velocity in a vertical plane. Grid cells are shown on x-coord; Resolution 5 m.

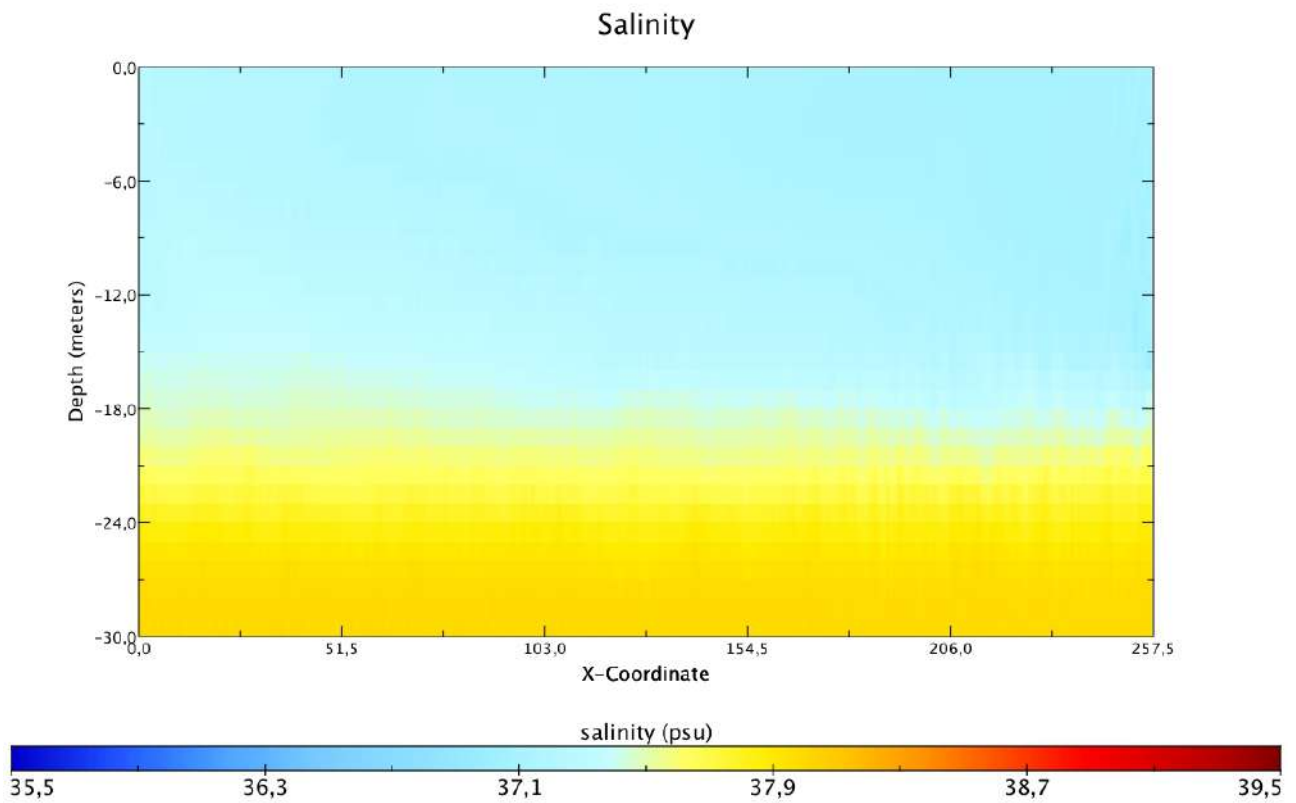


Fig.6.4: Contour plot of the vertical distribution of salinity in a vertical plane

6.2 MITgcm Simulation

In this section the results of the simulation performed by the use of MITgcm model ($\Delta t=9$ sec), tuned up its more suitable stand-alone configuration, are shown.

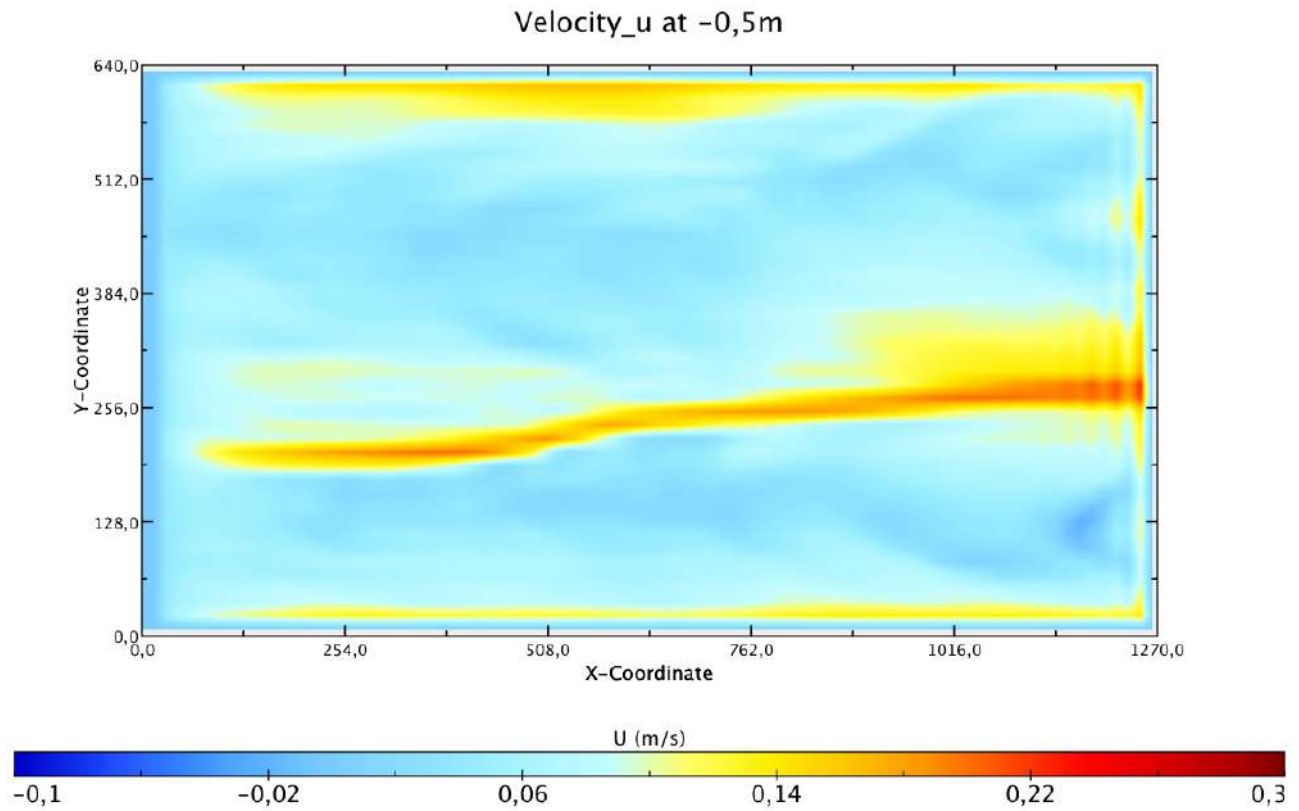
The domain is discretized in 84×42 grid cells in horizontal direction and 32 cells in vertical direction. With this discretization, the dimensions of the cells are about $\Delta x \approx \Delta y \approx 15$ m and $\Delta z \approx 1$ m. With respect to LES configuration, computational cells differ by a factor of 3 in the horizontal.

6.2.1 INSTANTANEOUS FIELD

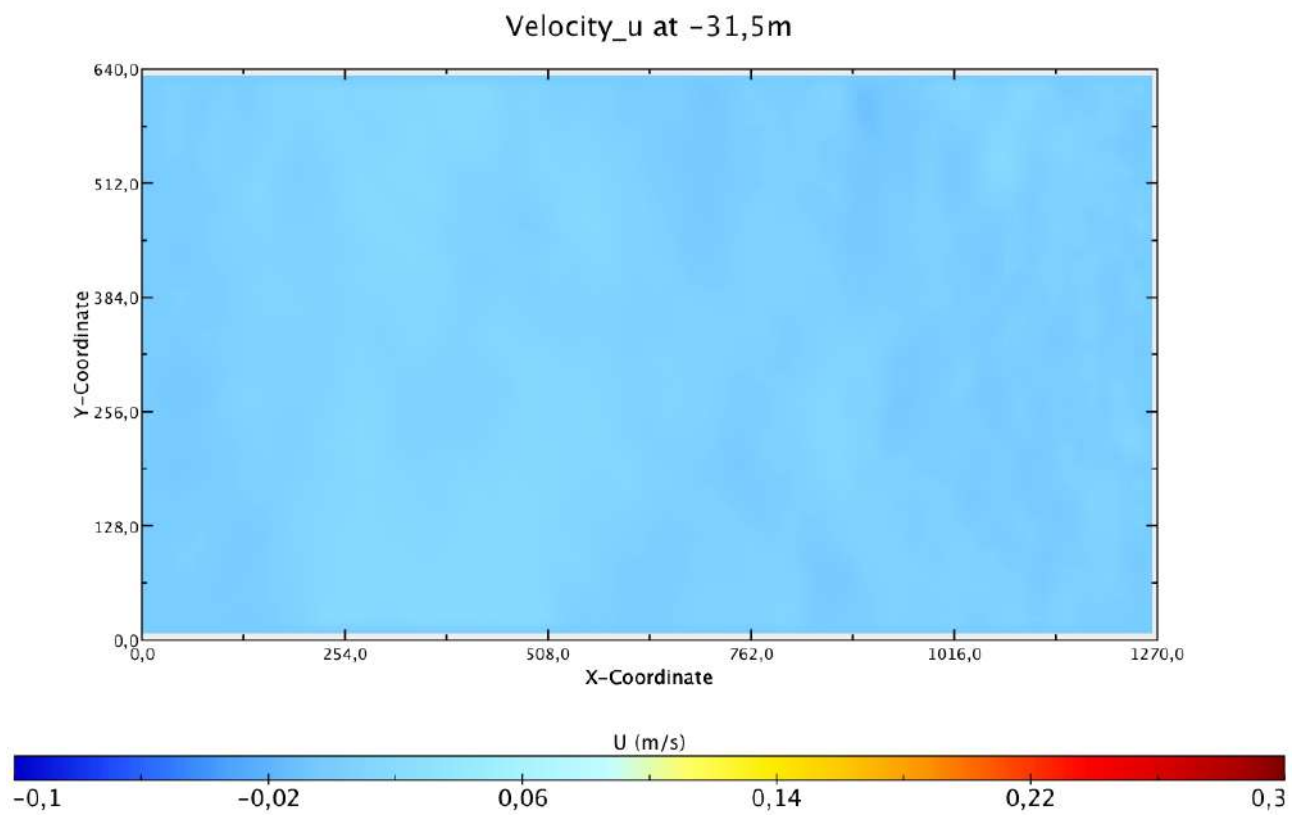
Figure 6.5 (A)-(B) shows the contour plot of the U component of the horizontal velocity at two different depths. Also in this case, the current is aligned to wind direction and the velocity field is reversed with the respect to wind direction close to the bottom, as expected. It is still possible to observe the presence of a streak with higher velocity in the middle of the domain, but with a coarse resolution.

Although it is still possible to observe a vertical mixing along the domain (figure 6.6), this mixing gives the impression to get slower at the depth of about -18m. This depth seems to constitute a sort of horizontal boundary for the horizontal vortices (i.e. recirculation area).

The contour plot of salinity profile (figure 6.7) confirms this feature. It is possible, indeed, to see an intense salinity mixing only up to -15m. Below -18m depth the initial stratification seems to persist.



A)



B)

Fig.6.5: Contour plot of U component of the horizontal instantaneous velocity at two horizontal planes: (A) -0,5m; (B) -31,5m.

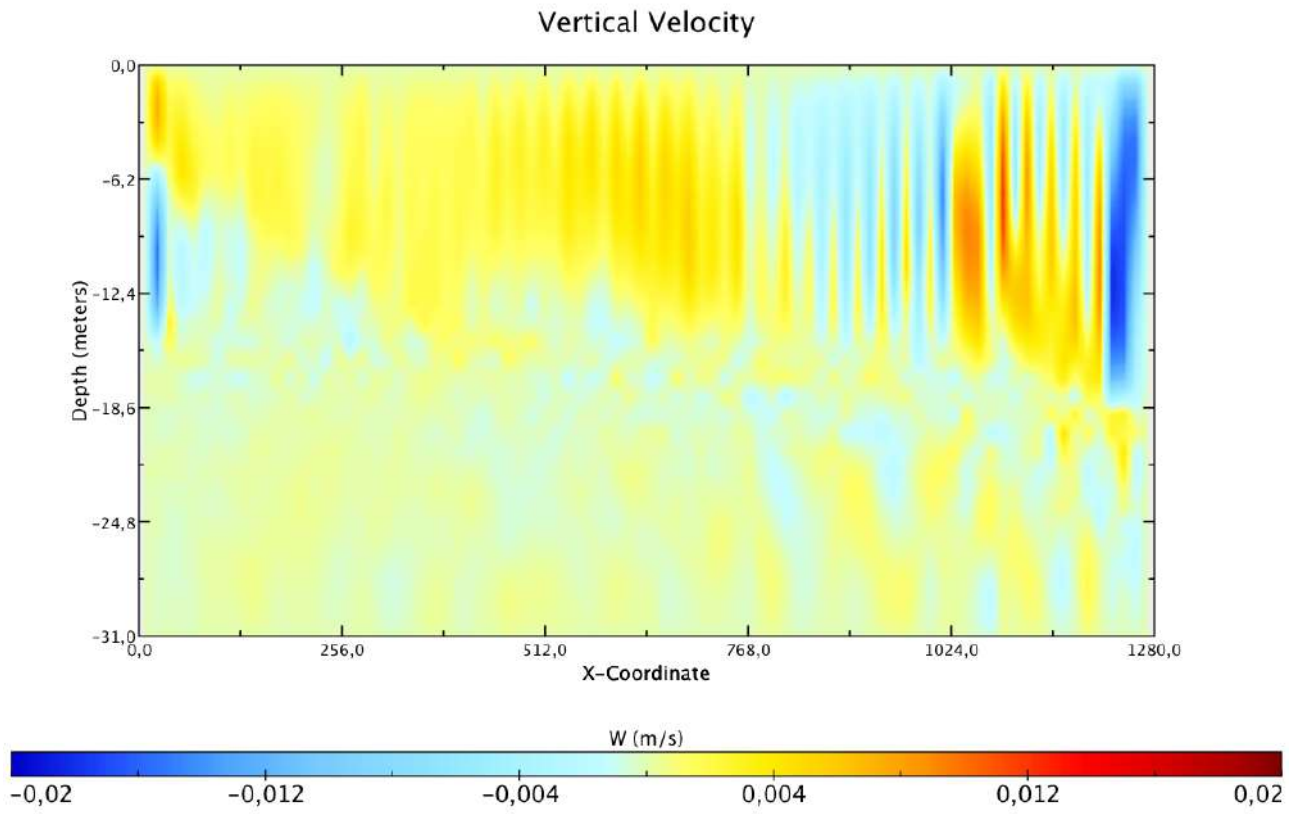


Fig.6.6: Contour plot of the vertical instantaneous velocity in a vertical plane

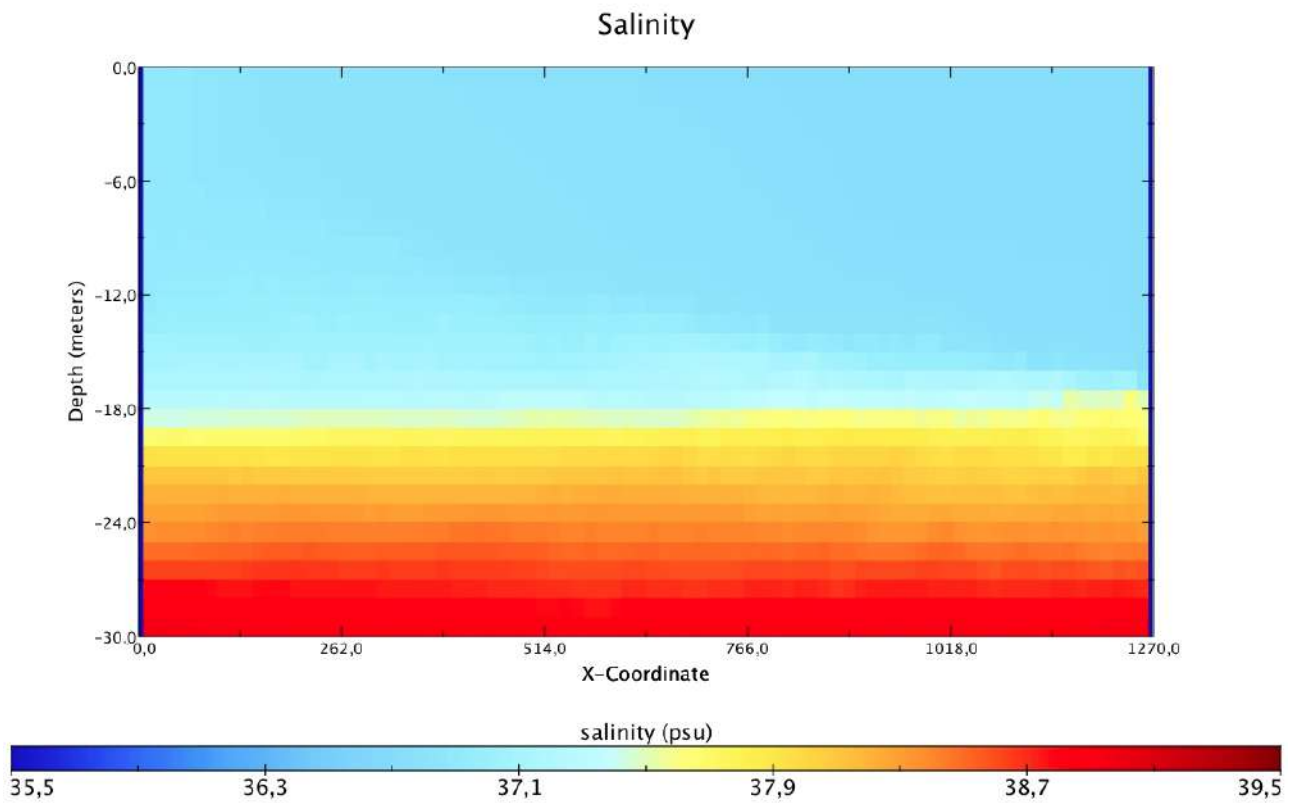


Fig.6.7: Contour plot of the vertical distribution of salinity in a vertical plane

6.3 Run-time Nesting

Results

Figures 6.8 (A and B) and 6.9 show the contour plot of U component of horizontal velocity (at - 0,5m and -31,5m) and the distribution of salinity, respectively, after 48 hours of simulation.

Comparing the results of simulations MITgcm stand-alone (on the left) and LES-Coast after nesting (on the right), it is evident, once again, how the resolution of the field has been improved. It is possible to observe a more detailed velocity field.

The “nested-LES” feels the effect of the nesting with MITgcm, showing a salinity field with a less salty upper layer, with respect to the results derived from the stand-alone simulation.

Finally, LES-Coast model has shown a sharpest mixing length-scale.

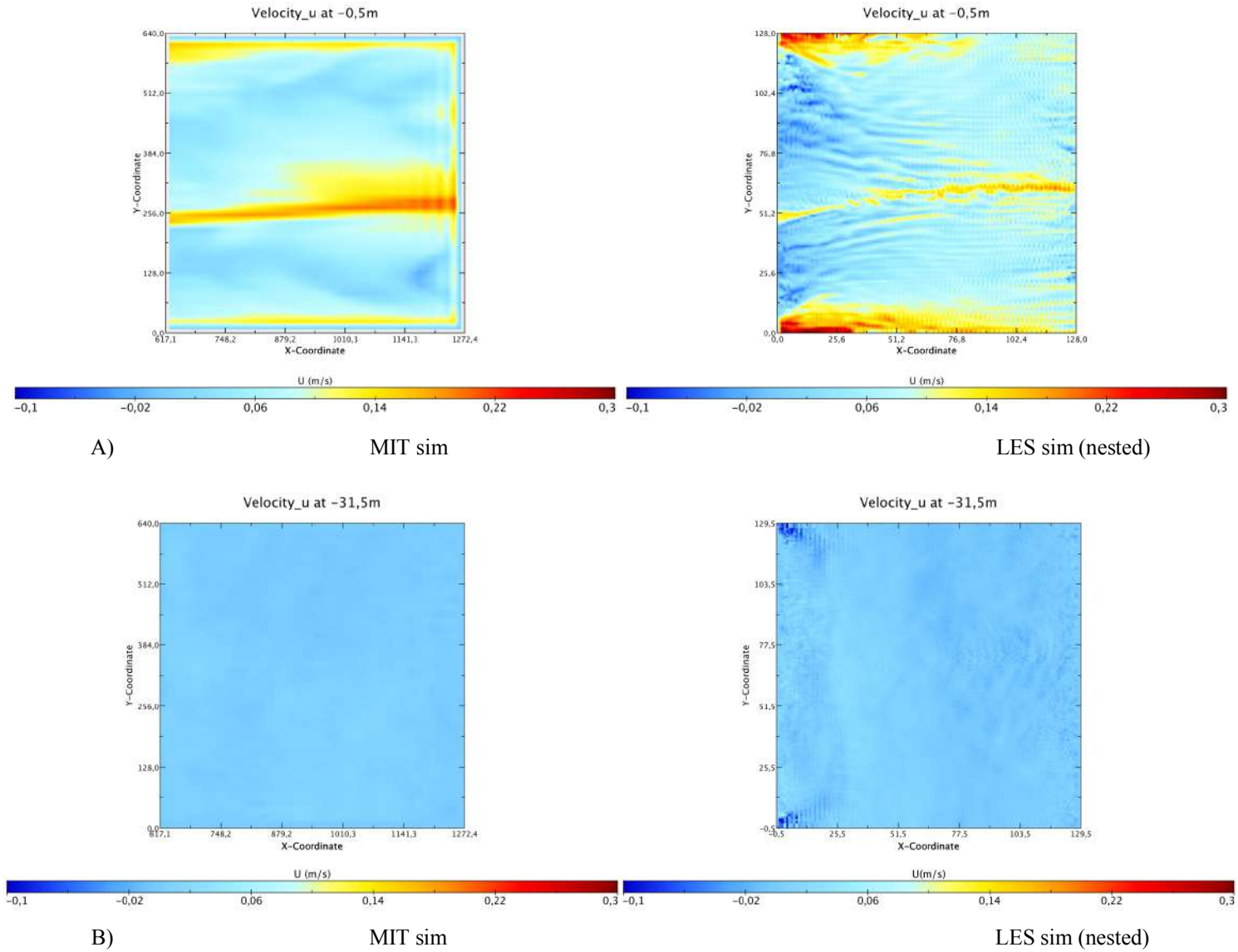


Fig.6.8: Contour plot of U component of the horizontal instantaneous velocity at two horizontal planes: (A) -0,5m; (B) -31,5m.

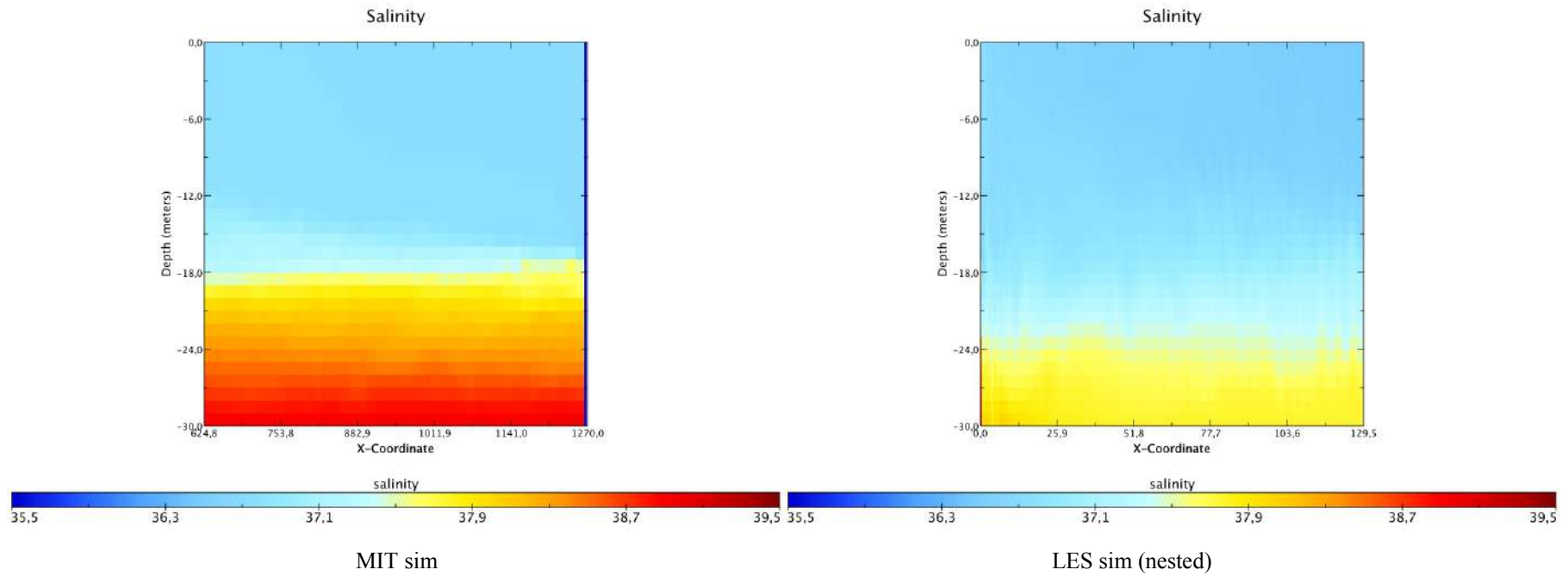


Fig.6.9: Contour plot of the vertical distribution of salinity in a vertical plane

Conclusions

Coastal and shelf seas represent a small fraction of the area of the global ocean but have a disproportionately large impact on many aspects of the marine environment and human activities.

Ocean general circulation models (OGCMs) have improved to the point that they can capture many of the features of mesoscale coastal processes but rarely with the accuracy necessary for vertical mixing estimates to be directly compared with small-scale turbulent measurements in the field. There is a need for carefully evaluating the accuracy of the OGCMs (and their Sub-Grid Scales models) below the mesoscale regime. As such a clear avenue for gaining more insight into the accuracy of OGCMs solutions for mixing and stirring problems is using Large Eddy Simulation (LES) as reference.

Definitely, investigating the large-scale impacts on smaller-scale processes in the coastal ocean can often be successfully treated by (one-way or two-way) nested regional studies.

In the present thesis the ability of MITgcm code and LES-Coast code to simulate a flow in a simple closed domain has been tested. For this purpose, idealized simulations have been used to examine and to compare the flow field, the turbulent kinetic energy and the eddy viscosities developed by the two different models. In this way a series of numerical simulations have been conducted and our goal has been to compare the results derived from these two modelling approaches: Ocean General Circulation Model (MITgcm) and a LES model, which has been used as our ground truth.

The numerical experiments, carried out by the use of MITgcm, were configured as similarly as possible to the LES settings, even though it was not a trivial matter to set them up in an identical fashion. Although comparing these two different modelling approaches has been not a trivial task, it has been a valuable way of testing the accuracy of MITgcm when the scales fall below the mesoscale regime.

A sensitivity analysis and calibration have been carried out in the application of the MITgcm (a non-hydrostatic, z-coordinate, finite volume model that solves the incompressible Navier-Stokes equations with the Boussinesq approximation on an Arakawa-C grid) to simulate the basin-scale response of a domain to wind forcing. Understanding model sensitivity has been a vital initial step.

The performance of different vertical and horizontal mixing parameterizations has been analysed to assess in what aspects they differ (the vertical mixing scheme developed by Gaspar et al 1990, GGL90, and the Leith viscosities for the horizontal mixing, respectively).

It has been discovered that the choice of a right configuration for GGL90 vertical mixing scheme plays a major role in the temporal evolution of horizontal velocity field.

The best results have been achieved by using Leith viscosity scheme for the horizontal mixing parameterization. However, no total convergence towards the ground truth reference (LES) has been attained, indeed, the simulated feature of horizontal velocity field appears to be similar, while MITgcm simulations differ from LES in the amount of vertical mixing. In MITgcm simulations the vertical mixing has been underestimated with all configuration used.

Considering that nesting remains an important approach for investigating of regional systems and providing fine-scale information, an unprecedented approach has been proposed.

A nesting (before “off-line” and successively “run-time”) between the general circulation model and a LES model has been designed and developed. The MIT output serves as the initial and lateral boundary conditions for LES model simulations. The two models involved are coupled via an external driver that performs all the necessary interpolations. The two models run in parallel, together with an external driver that establishes the connection between MITgcm and LES-Coast.

The impact of the temporal updating frequency of the lateral boundary conditions (LBC) is an important topic and it has been discussed in this thesis. In one-way “off-line” nesting procedure the update interval for the lateral boundary conditions must be specified. In “run-time” nesting, the nested finer domain and the outer coarser domain interact at every time step of the outer coarse-grid integration. To investigate the effect of the lateral boundary forcing update interval, three updating frequencies have been compared: 2 hours, 1 hours (for the off-line nesting case) and 9 seconds for the run-time case. Comparing the graphs of Kinetic Energy for the three LES simulations, performed with different update intervals for the lateral boundary conditions, it has been possible to determine how the small-scale motions grow in different way. It is possible to observe how as the update interval becomes smaller as the increment in KE becomes bigger. Discrepancies between the three simulations appear evident in the earlier period and appear unclear after the domain becomes fully saturated with small-scale fluctuations.

It has been illustrated how the “nested-LES” feels the effects of the nesting, showing, at the surface, higher values of variable U at the middle of the domain (absent in the simulation performed by LES stand-alone) in the neutral stratified experiment.

Comparing the results of simulations MITgcm stand-alone and LES-Coast after nesting, it is evident how the resolution of the velocity field has been clearly improved. Moreover, the nested model has shown a remarkable sensitivity to the update frequency of the lateral boundary conditions, showing a slight difference in the evolution of the U component of velocity field at the surface. Generally, as the update interval is set to be smaller, the model accuracy is improved (Michioka and Chow 2008).

Finally, the good agreement found between the velocity field developed by the new integrated model in the “run-time” nesting and that realized in the “off-line” procedure, confirms both the robustness and effectiveness of the new model.

FUTURE WORK

The results of the present study constitute an important starting point for the ongoing studies and for the improvement of this new methodology applied to a real scenario.

The next step, indeed, will be the application of this coupled-model on the Venice Lagoon, in order to develop an unprecedented real-time downscaling from an operating ocean general circulation model to a high-resolution coastal model. The Ocean General Circulation model will be “MITO” an operating version of the MITgcm code, designed and developed at the ENEA center, that is able to produce sea forecasts, assimilating and reproducing the tidal signal, too.

The MITO domain, that covers the entire Mediterranean Sea and Black Sea, is discretized by a curvilinear grid of 2500 x 750 points. The model has a resolution of $1/48^\circ$ and the grid has been developed improving a previous $1/16^\circ$ model grid. At the Strait of Gibraltar, the grid has been highly stretched in order to reach a resolution of $1/800^\circ$ and a local refinement has been applied at the Strait of Dardanelles and at the Strait of Bosphorus, too. In these straits the number of meridians and parallel has been progressively increased until to reach a resolution of $1/250^\circ$.

The vertical domain is discretized into 100 non-uniformly spaced z-levels ranging from 2m to 62m between surface and 1500m depths. A constant value of 62m has been chosen from 1500m depth to the bottom.

WHY AN OPERATING OCEAN MODEL?

The Operational Oceanography is an evolution of the traditional application of oceanography. The products derived from operational oceanography are several, one of them is the possibility to provide continuous forecasts of the future condition of the sea for as far ahead as possible.

The outputs from the model can be oriented to the management of emergencies. Examples of final products can include: warnings (of coastal floods and contaminants), optimum routes for ships, ocean currents and ocean climate variability.

Analyses, carried out by the International Tanker Owners Pollution Federation-2011, show that most of oil spill accidents, occurred worldwide, with oil releases smaller than 700 tons, has been taking place in coastal areas.

Oil spill events can cause strong damage to the marine environment and coastal areas. Oil in the sea is dangerous for biological species and for human health; furthermore, contamination of coastline has a strong impact in tourist and commercial activities. The fate and the persistence of oil in the sea water are conditioned by the physical, chemical and biological processes that occur after oil release, they depend on oil properties as well as environmental conditions, such as sea temperature, waves, wind and currents.

In Venice Lagoon, because of the massive presence of all kind of ships, it could be essential to be able to predict, in real-time, the trajectory of an oil spill.

VENICE LAGOON

Lagoons are highly productive areas that are situated in the transitional areas at the land-ocean boundary. They are important to mankind because many industrial, commercial, and recreational activities are concentrated in these regions. The need to manage this part of the coastal zone makes of primary interest to understand processes occurring in these water bodies (Umgiesser, G. et al, 2014). In recent years, these areas have become important because they provide the key to understanding the general dynamics of the seas they are connected with. Their existence and their influence on the coastal zones have become a fundamental study topic in many disciplines (Umgiesser, G. et al, 2014).

Venice lagoon is located in the northwest Adriatic Sea and is the largest Mediterranean lagoon (surface 500 km², length 50 km, mean width 15 km). The bathymetry is characterized by the presence of navigable channels, tidal flats, and shoals. The latter ones can either be wet or dry depending on tidal level. Only 5% of the lagoon area is deeper than 5 m and 75% is shallower than 2 m. The mean depth is 1.5 m, but there are some areas deeper than 30 m.

Three inlets connect the lagoon with the open sea (Lido, Malamocco, and Chioggia, from North to South) with length around 2.5 km each, mean depth 10, 16, and 8 m, respectively, and width from 0.5 to 1 km.

The mean tidal range at the inlets of the Venice Lagoon is 50 cm during neap tide and 100 cm during spring tide (Umgiesser, G. et al, 2014).

The model implementation

The numerical grid describing the Lagoon of Venice will be made out of 1866 x 2400 grid points, the model will have a resolution of 15 m in the horizontal direction and 1 m in the vertical direction.

Data set

Two different datasets have been processed in order to build the bathymetry necessary for this work.

These different datasets are:

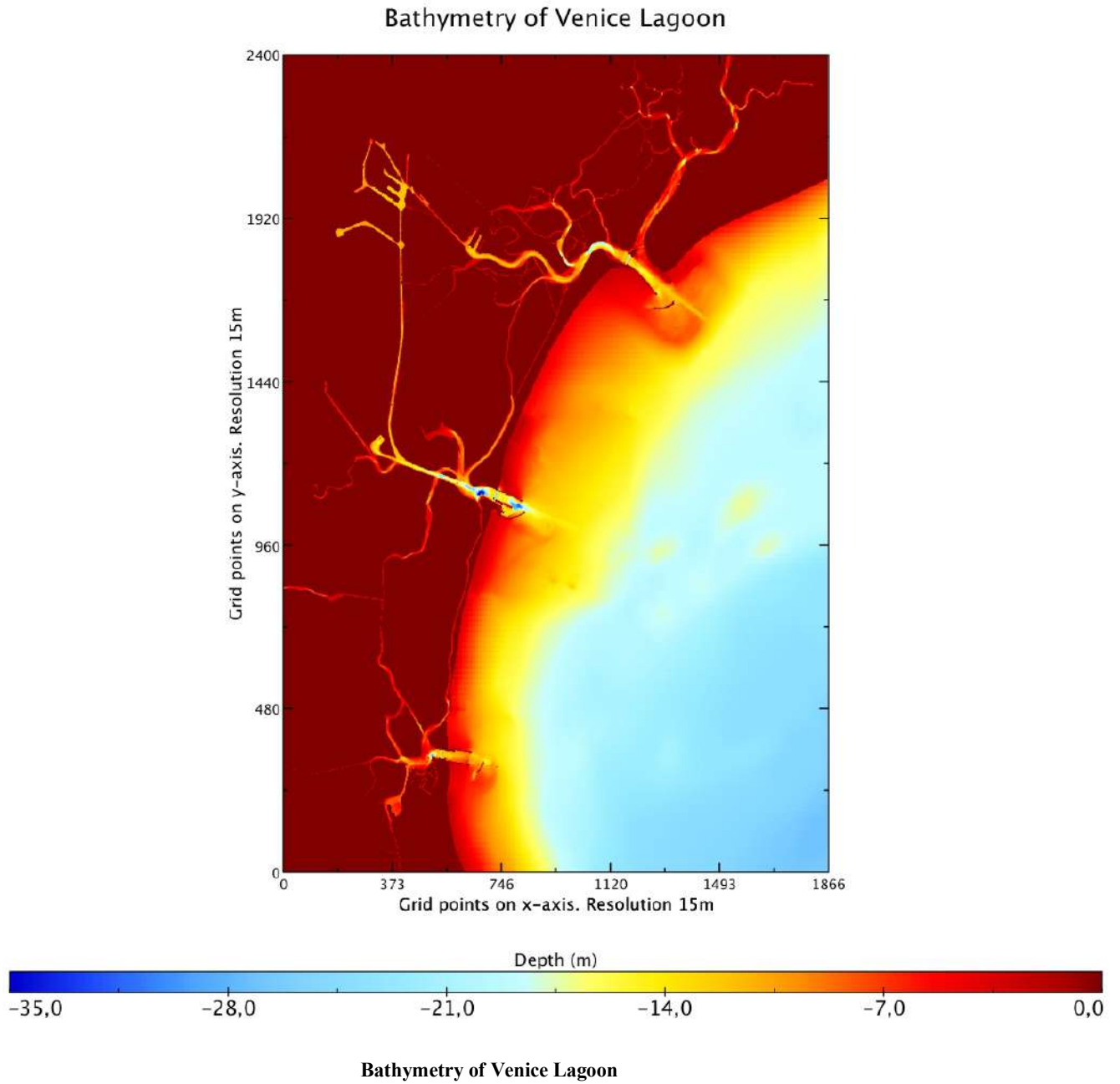
1) The “High resolution multibeam and hydrodynamic datasets of tidal channels and inlets of the Venice Lagoon” (Madricardo, F. et al. 2017). This dataset is unique not only because it depicts the seafloor morphologies with unprecedented detail but also, because it was acquired just before the MOSE barrier system starts to operate. Therefore, it represents a benchmark for evaluating the possible impacts of the major engineering interventions taking place in the Lagoon of Venice and its inlets. This dataset contains high-resolution ASCII:ESRI gridded bathymetric data (0.5 m DTM). Data was collected during a six-months survey (lasting from May to December 2013) in the channel network of the Venice Lagoon by means of the MBES system Kongsberg EM-2040 Compact dual head.

2) Emodnet Bathymetry. A harmonised EMODnet Digital Terrain Model (DTM) is generated for European sea regions from selected bathymetric survey data sets and composite DTMs, while gaps with no data coverage are completed by integrating the GEBCO Digital Bathymetry. For each maritime region bathymetric survey data and aggregated bathymetry data sets have been collated from public and research organizations. These have been processed and quality controlled and used to produce regional Digital Terrain Models (DTM). Thereafter these have been integrated into the EMODnet DTM for European seas. The DTM has a grid size of .125 minute * .125 minute.

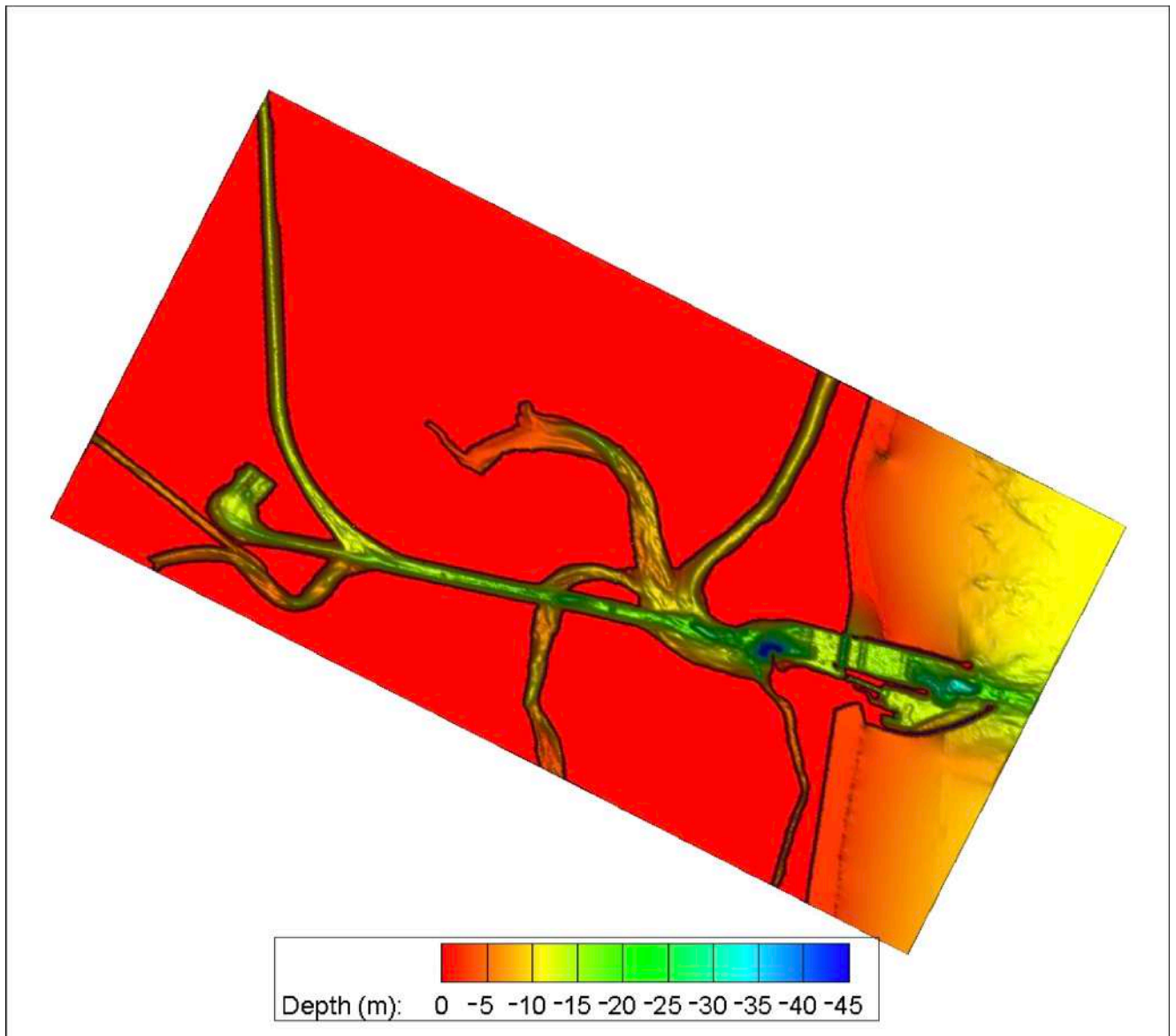
Data processing

The first step has been the acquisition and the handling of the high-resolution dataset. This dataset has been downsampled to a resolution of 5 m in order to have data more suitable. The second step has been the acquisition of the EMODnet data for the area of the Venice Lagoon. The two datasets have been merged and then an interpolation has been applied. Finally, the obtained dataset

has been downscaled to a 15 m resolution, carrying out a suitable smoothing, in order to have the definitive bathymetry, as shown in the following figure.



As a representative example of the bathymetry reconstructed by Immersed Boundary method, in the following figure it is shown the area of Malamocco Inlet.



Bathymetry of Malamocco Inlet reconstructed by Immersed Boundary method

Bibliography

- Adcroft, A., Campin, J.M., Dutkiewicz, S., Evangelinos, C., Ferreira, D., Forget, G., Fox-Kemper, B., Heimbach, P., Hill, C., Hill, E., Hill, H., Jahn, O., Losch, M., Marshall, J., Maze, G., Menemenlis, D., Molod, A. «MITgcm user manual.» MIT Department of EAPS, Cambridge, 2014.
- Armenio, V., Sarkar, S. «An investigation of stably stratified turbulent channel flow using large-eddy simulation.» *Journal of fluid mechanics* 459 (2002): 1-42.
- Baumert, H., J. H. Simpson, and J. Sundermann. «Marine turbulence .» (Cambridge University Press) 2005.
- Berntsen, J. «Internal pressure errors in sigma-coordinate ocean models .» *Journal of Atmospheric and Oceanic Technology* 19 (2002): 1403–1414 .
- Berntsen, J., Xing, J., Davies, A. «Numerical studies of flow over a sill: sensitivity of the non-hydrostatic effects to the grid size.» *Ocean Dynamics* 59 (2009): 1043–1059.
- Bjerknes, V. «Das Problem der Wettervorhersage, betrachtet vom Standpunkte der Mechanik und der Physik .» *Meteorologische Zeitschrift* 21 (1904).
- Boegman, L., Dorostkar, A. «Three-dimensional simulation of NLIW generation, propagation and breaking in Cayuga Lake.» (7th Int. Symp. on Stratified Flows, Rome, Italy, August 22 - 26) 2011.
- Bricheno, L., Wolf, J., Brown, J. «Impacts of high resolution model downscaling in coastal regions.» *Continental Shelf Research* 87 (2013): 7-16.
- Brown E, A. Colling, D.Park, J.Phillips, D. Rothery, and J. Wright. «Sea-water: Its composition properties and behavior.» *The Open University* 2 (1989).

- Bryan, K. «A numerical method for the study of the circulation of the world ocean.» *Journal of Computational Physics* 4 (1969): 347-376.
- Burchard, H. «Applied turbulence modeling in marine waters .» (Springer) 2002.
- Chang, Y.S., Xu, X., Özgökmen, T.M., Chassignet, E.P., Peters, H., Fischer, P.F.
«Comparison of gravity current mixing parameterizations and calibration using a high-resolution 3D nonhydrostatic spectral element model.» *Ocean Modell.* 10 (2005): 342-368.
- Curchitser, E. N., Haidvogel, D. B., Hermann, A. J., Dobbins, E. L., Powell, T. M., Kaplan, A.
«Multi-scale modeling of the North Pacific Ocean: Assessment and analysis of simulated basin-scale variability (1996–2003).» *J. Geophys. Res.-Ocean.* 110 (2005).
- Deardorff, J.W. «A numerical study of three-dimensional turbulent channel flow at large Reynolds numbers.» *Journal of Fluid Mechanics* 41 (1970): 453–465 .
- Deardorff, J.W. «The use of subgrid transport equations in a three-dimensional model of atmospheric turbulence.» *ASME Journal of Fluid Engineering* , 1973: 429–438 .
- Debreu, L., Marchesiello, P., Penven, P., Cambon, G. «Two-way nesting in split-explicit ocean models: algorithms, implementation and validation.» *Ocean Modell.* 49-50 (2012): 1-21.
- Denbo, D. W., Skillingstad, E. D. «An ocean large-eddy simulation model with application to deep convection in the Greenland Sea.» *J. Geophys. Res.* 101 (1996): 1095–1110 .
- Denis, B., Laprise, R., Caya, D. «Sensitivity of a regional climate model to the resolution of the lateral boundary conditions .» *Climate Dynamics* 20 (2003): 107-126.
- Dorostkar, A., Boegman, L., Diamessis, P., Pollard, A. «Sensitivity of MITgcm to different model parameters in application to Cayuga Lake.» *Environmental Hydraulics*, 2010.

- Durski, S., Glenn, S., Haidvogel, D. «Vertical mixing schemes in the coastal ocean: Comparison of the level 2.5 Mellor-Yamada scheme with an enhanced version of the K profile parameterization.» *Journal of Geophysical Research* 109 (2004).
- EMODnet Bathymetry Consortium (2016): EMODnet Digital Bathymetry (DTM).
- Ferziger, J.H., and M. Peric'. «Computational methods for fluid dynamics .» (Springer) 2002.
- Fox-Kemper, B., Ferrari, R., Hallberg, R. «Parameterization of mixed layer eddies. Part I: theory and diagnosis.» *J. Phys. Oceanogr.* 38 (2008): 1145-1165.
- Fox-Kemper, B., Ferrari, R.,. «Parameterization of mixed layer eddies. Part II: prognosis and impact.» *J. Phys. Oceanogr.* 38 (2008): 1166-1179.
- Fox-Kemper, B., Menemenlis, D. «Can large eddy simulation techniques improves mesoscale rich ocean models?» *Geophys. Monogr.*, 2008: 319-337.
- Fox-Kemper, B., Menemenlis, D. «Can Large Eddy Simulation Techniques Improve Mesoscale Rich Ocean Models? .» *Ocean Modeling* 177 (2008).
- Furuichi, N., Hibiya, T. «Assessment of the upper-ocean mixed layer parameterizations using a large eddy simulation model .» *J. of Geophysical Research: Ocean* 120 (2015): 2350–2369 .
- Garwood, R. W., Isakari, S., Gallacher, P. «Thermobaric convection. .» *The Polar Oceans, Geophys. Monogr.*, n. 85 (1994): 199-209.
- Gaspar, P., Gregoris, Y., Lefevre, J. «A simple eddy kinetic energy model for simulations of the oceanic vertical mixing: Tests at station papa and long-term upper ocean study site.» *J. Geophys. Res.* 16 (1990): 179-193.
- Griffies, S. «Fundamentals of Oceanic Climate Models.» (Princeton University Press) 518 (2004).

- Griffies, S., Hallberg, R. «Biharmonic friction with a Smagorinsky-like viscosity for use in large-scale eddy-permitting ocean models.» *Mon. Wea. Rev.* 128 (2000): 2935–2946 .
- Haidvogel, D.B., A.Beckmann. «Numerical ocean circulation modeling .» *Series on Environmental Science and Management (Imperial College Press)* 2 (1998).
- Holland, W. «The role of mesoscale eddies in the general circulation of the ocean—numerical experiments using a wind-driven quasi-geostrophic model.» *Journal of Physical Oceanography* 8 (1978): 363–392 .
- Holt, J., Allen, J. I., Anderson, T. R., Brewin, R., Butenschon, M., Harle, J., Huse, G., Lehodey, P., Lindemann, C., Memery, L., Salihoglu, B., Senina, I., Yool, A. «Challenges in integrative approaches to modelling the marine ecosystems of the North Atlantic: Physics to Fish and Coasts to Ocean .» *Prog. Oceanogr.* 129 (2014): 285–313 .
- Holt, J., Hyder, P., Ashworth, M., Harle, J., Hewitt, H., Liu, H. «Prospects for improving the representation of coastal and shelf seas in global ocean models .» *Geosci. Model Dev.* 10 (2017): 499-523.
- Holt, J., Wakelin, S., Lowe, J., Tinker, J. «The potential impacts of climate change on the hydrography of the north-west European Continental shelf .» *Prog. Oceanogr.* 86 (2010): 361-379.
- Jayne, S.R., L. C. St Laurent, S. T. Gille. «Connections between ocean bottom topography and earth's climate.» *Oceanography* 17 (2004): 65-74.
- Julien, K., Legg, S., McWilliams, J., Werner, J. «Enetrative convection in rapidly rotating flows: Preliminary results from numerical simulation.» *Dyn. Atmos. Oceans* 24 (1996b): 237–249 .
- Kantha, L.H., e C.A. Clayson. «Numerical models of oceans and oceanic processes.» *International Geophysics Series (Academic Press)* 66 (2000).

- Kantha, L.H., and Clayson, C.A. «Small scale processes in geophysical fluid flows.» International Geophysics Series (Academic Press) 67 (2000).
- Kim, J., Moin, P. «Application of a fractional step to incompressible Navier-Stokes equations.» J. Comput. Phys. 59 (1985): 308–323.
- Kolmogorov, A. «The local structure of turbulence in incompressible viscous fluid for very large Reynolds numbers .» Proceedings: Mathematical and Physical Sciences 434 (1991): 9-13.
- Kundu, P.K., and M. Cohen. «Fluid mechanics .» (Elsevier Academic Press) 2004.
- Leith, C. «Large eddy simulation of complex engineering and geophysical flows.» Physics of Fluids 10 (1968): 1409–1416 .
- Leith, C. «Stochastic models of chaotic systems .» Physica D 98 (1996): 481–491 .
- Lilly, D.K., «The representation of small-scale turbulence in numerical simulation experiments .» Proceedings of the IBM Scientific Computing Symposium on Environmental Sciences. , 1967.
- Madricardo, F. et al. «High resolution multibeam and hydrodynamic dataset of tidal channels and inlets of the Venice Lagoon.» Sci. Data. 4:170121 (2017).
- Mahadevan, A., Tandon, A. «An analysis of mechanisms for submesoscale vertical motion at ocean fronts.» Ocean Modell. 14 (2006): 241-256.
- Marques, G., Ozgokmen, T. «On modeling turbulent exchange in buoyancy-driven fronts.» Ocean Modelling 83 (2014): 43–62 .
- Marshall, J., Hill, C., Perelman, L., Adcroft, A. «Hydrostatic, quasi–hydrostatic and nonhydrostatic ocean modeling .» Journal of Geophysical Research 102 (1997): 5733–5752 .

- Mellor, G.L., Y. Oey, and T. Ezer. «Sigma coordinate pressure gradient errors and the seamount problem.» *Journal of Atmospheric and Oceanic Technology* 15 (1998): 1122–1131 .
- Michioka, T., Chow, F. «High-Resolution Large-Eddy Simulations of Scalar Transport in Atmospheric Boundary Layer Flow over Complex Terrain .» *JOURNAL OF APPLIED METEOROLOGY AND CLIMATOLOGY* 47 (2008).
- MITgcm, User Manual. 2014.
- Noh, Y., Min, H., Raasch, S. «Large Eddy Simulation of the Ocean Mixed Layer: The Effects of Wave Breaking and Langmuir Circulation .» *J. of Physical Oceanography* 34 (2003).
- Petronio, A., Roman, F., Nasello, Armenio, V. «Large Eddy Simulation model for wind-driven sea circulation in coastal areas.» *Nonlinear Processes in Geophysics* 20 (2013): 1095-1112 .
- Piomelli, U. «Wall-layer models for large-eddy simulations.» *Progr. Aerospace Sci.* 44 (2008): 437-446.
- Raasch, S., Etling, D. «Modeling Deep Ocean Convection: Large Eddy Simulation in Comparison with Laboratory Experiments .» *Journal of Physical Oceanography* 28 (1997).
- Ramachandran, S., Tandon, A., Mahadevan, A. «Effect of subgrid-scale mixing on the evolution of forced submesoscale instabilities.» *Ocean Modell.* 66 (2013): 45-63.
- Renner, A. H. H., Heywood, K. J., and Thorpe, S. E. «Validation of three global ocean models in the Weddell Sea .» *Ocean Model.* 30 (2009): 1-15.
- Roman, F., Armenio, V., Frohlich. «A simple wall layer model for Large Eddy Simulation with immersed boundary method.» *Physics of Fluids* 21 (2009a).

- Roman, F., Napoli, E., Milici, Armenio, V. «An improved immersed boundary method for curvilinear grids.» *Computers and Fluids* 38 (2009b): 1510-1527 .
- Roman, F., Stipcich, G., Armenio, V., Inghilesi, Corsini. «Large eddy simulation of mixing in coastal areas.» *International Journal of Heat and Fluid Flow* 31 (2010): 327-341.
- Scotti, A. «Large eddy simulation in the ocean .» *International Journal of Computational Fluid Dynamics* 24 (2010): 393–406 .
- Shuang, L., Jinbao, S., Hailun, H., Yansong, H. «Large eddy simulation of turbulence in ocean surface boundary layer at Zhangzi Island offshore .» *Acta Oceanol. Sin.* 32 (2013): 8-13.
- Skyllingstad, E., Smyth, W., Moum, J. «Upper-Ocean Turbulence during a Westerly Wind Burst: A Comparison of Large-Eddy Simulation Results and Microstructure Measurements .» *J. of Physical Oceanography* 29 (1999).
- Skyllingstad, E., Wijesekera, H. «Large-Eddy Simulation of Flow over Two-Dimensional Obstacles: High Drag States and Mixing.» *J. of Physical Oceanography* 34 (2003).
- Smagorinsky, J.,. «General circulation experiments with the primitive equations. I: the basic experiment.» *Monthly Weather Review* 91 (1963): 99-165.
- Stashchuk, N., Vlasenko, V., Inall, M., Aleynik, D. «Horizontal dispersion in shelf seas: High resolution modelling as an aid to sparse sampling.» *Progress in Oceanography* 128 (2014): 74-87.
- Termonia, P., Deckmyn, A., Hamdi, R. «Study of the Lateral Boundary Condition Temporal Resolution Problem and a Proposed Solution by Means of Boundary Error Restarts .» *MONTHLY WEATHER REVIEW* 137 (2009).
- Thomas, L., Tandon, A., Mahadevan, A.,. «Submesoscale processes and dynamics. Eddy resolving ocean models.» *Geophysical Monograph* 177 (2008): 17-38.

- Umgiesser, G., Ferrain, C., Cucco, A., De Pascalis, F., Bellafiore, D., Ghezzi, M., Bajo, M.. «Comparative hydrodynamics of 10 Mediterranean lagoons by means of numerical modeling.» *J. Geophys. Res. Oceans* 119 (2014): 2212-2226.
- Van Sy Pham, Hwan Hwang, Hyeyun Ku. «Optimizing dynamic downscaling in one-way nesting using a regional ocean model .» *Ocean Modelling* 106 (2016): 104-120.
- Vlasenko, V., Stashchuk, N., McEwan, R. «High-resolution modelling of a large-scale river plume .» *Ocean Dynamics* 63 (2013): 1307–1320 .
- Wakelin, S. L., Holt, J. T., Proctor, R. «The influence of initial conditions and open boundary conditions on shelf circulation in a 3D ocean-shelf model of the North East Atlantic .» *Ocean Dynam.* 59 (2009): 67-81.
- Wang, D., Large, W., McWilliam, J. «Large-eddy simulation of the equatorial ocean boundary layer: Diurnal cycling, eddy viscosity, and horizontal rotation .» *J. of Geophysical Res.* 101 (1996): 3649-3662.
- Wang, D., McWilliams, J., Large, W. «Large-Eddy Simulation of the Diurnal Cycle of Deep Equatorial Turbulence .» *J. of Physical Oceanography* 28 (1997).
- Warner, J., Geyer, W., Lerczak, J. «Numerical modeling of an estuary: a comprehensive skill assessment.» *J. Geophys. Res.* 110 (2005a).
- Wu, J. «Wind-stress coefficient over sea surface from breeze to hurricane .» *Journal of Geophysical Research* 87 (1982): 9704-9706 .
- Xing, J., Davies, A. «On the importance of non-hydrostatic processes in determining tidally induced mixing in sill regions.» *Continental Shelf Research* 27 (2007): 2162–2185.
- Xu, X., Chang, Y., Peters, H., Özgökmen, T., Chassignet, E. «Parameterization of gravity current entrainment for ocean circulation models using a high-order 3D nonhydrostatic spectral element model.» *Ocean Modell.* 14 (2006): 19-44.

Xu, Y., Rignot, E., Fenty, I., Menemenlis, D., Flexas, M. «Subaqueous melting of Store Glacier, west Greenland from three-dimensional, high-resolution numerical modeling and ocean observations.» *Geophys. Res. Lett.* 40 (2013): 4648–4653 .

Zang, Y., Street, R. L., Koseff, J. R. «A Non-staggered Grid, Fractional Step Method for Time-Dependent Incompressible Navier-Stokes Equations in Curvilinear Coordinates.» *Journal of Computational Physics* 114 (1994): 18-33.

Zhang, W. G. F., Wilkin, J. L., Chant, R. J. «Modeling the Pathways and Mean Dynamics of River Plume Dispersal in the New York Bight .» *J. Phys. Oceanogr.* 39 (2009): 1167–1183 .

Zikanov, O., Slinn, D., Dhanak, M. «Large-eddy simulations of the wind-induced turbulent Ekman layer.» *Journal of Fluid Mechanics* 495 (2003): 343-368.